

University of Windsor

Scholarship at UWindor

Electronic Theses and Dissertations

Theses, Dissertations, and Major Papers

1-1-2007

Computational investigations on metalloenzymes and metallo-like biomolecules.

Jesse J. Robinet
University of Windsor

Follow this and additional works at: <https://scholar.uwindsor.ca/etd>

Recommended Citation

Robinet, Jesse J., "Computational investigations on metalloenzymes and metallo-like biomolecules." (2007). *Electronic Theses and Dissertations*. 7041.
<https://scholar.uwindsor.ca/etd/7041>

This online database contains the full-text of PhD dissertations and Masters' theses of University of Windsor students from 1954 forward. These documents are made available for personal study and research purposes only, in accordance with the Canadian Copyright Act and the Creative Commons license—CC BY-NC-ND (Attribution, Non-Commercial, No Derivative Works). Under this license, works must always be attributed to the copyright holder (original author), cannot be used for any commercial purposes, and may not be altered. Any other use would require the permission of the copyright holder. Students may inquire about withdrawing their dissertation and/or thesis from this database. For additional inquiries, please contact the repository administrator via email (scholarship@uwindsor.ca) or by telephone at 519-253-3000ext. 3208.

Computational Investigations on
Metalloenzymes and Metallo-Like
Biomolecules

by

Jesse J. Robinet

A Thesis
Submitted to the Faculty of Graduate Studies
through the Department of Chemistry and Biochemistry
in Partial Fulfillment of the Requirements for
the Degree of Master of Science at the
University of Windsor

Windsor, Ontario, Canada

2007

© 2007 Jesse J. Robinet



Library and
Archives Canada

Bibliothèque et
Archives Canada

Published Heritage
Branch

Direction du
Patrimoine de l'édition

395 Wellington Street
Ottawa ON K1A 0N4
Canada

395, rue Wellington
Ottawa ON K1A 0N4
Canada

Your file *Votre référence*
ISBN: 978-0-494-35068-3
Our file *Notre référence*
ISBN: 978-0-494-35068-3

NOTICE:

The author has granted a non-exclusive license allowing Library and Archives Canada to reproduce, publish, archive, preserve, conserve, communicate to the public by telecommunication or on the Internet, loan, distribute and sell theses worldwide, for commercial or non-commercial purposes, in microform, paper, electronic and/or any other formats.

The author retains copyright ownership and moral rights in this thesis. Neither the thesis nor substantial extracts from it may be printed or otherwise reproduced without the author's permission.

AVIS:

L'auteur a accordé une licence non exclusive permettant à la Bibliothèque et Archives Canada de reproduire, publier, archiver, sauvegarder, conserver, transmettre au public par télécommunication ou par l'Internet, prêter, distribuer et vendre des thèses partout dans le monde, à des fins commerciales ou autres, sur support microforme, papier, électronique et/ou autres formats.

L'auteur conserve la propriété du droit d'auteur et des droits moraux qui protègent cette thèse. Ni la thèse ni des extraits substantiels de celle-ci ne doivent être imprimés ou autrement reproduits sans son autorisation.

In compliance with the Canadian Privacy Act some supporting forms may have been removed from this thesis.

Conformément à la loi canadienne sur la protection de la vie privée, quelques formulaires secondaires ont été enlevés de cette thèse.

While these forms may be included in the document page count, their removal does not represent any loss of content from the thesis.

Bien que ces formulaires aient inclus dans la pagination, il n'y aura aucun contenu manquant.


Canada

Abstract

In this thesis, the mechanisms of two metalloenzymes and a non-metal redox active enzyme, as well as the binding of the ions of nitric oxide to aromatic biomolecules have been investigated using computational techniques.

In Chapter 3, we have used density functional theory to study the mechanism of the metalloenzyme LpxC. Notably, LpxC is found to catalyse its deacetylation reaction using an acid/base pair mechanism, employing His265 and Glu78 for these roles, respectively. Furthermore, due to orientation of active site amino acid residues and their interactions, LpxC is found to require additional reaction steps in its mechanism in order to cleave the amide bond compared to the water-assisted hydrolysis of an amide bond and related metallopeptidases.

In Chapter 4, density functional theory methods have been employed to systematically investigate the overall mechanism of the second half-reaction of nitric oxide synthases. The previously identified initial heme-bound hydrogen peroxide intermediate is found to proceed through a mechanism containing a Compound I ($\text{Fe}_{\text{heme}}\text{-O}$) intermediate, common to P450 enzymes. The formation of the final citrulline and NO products can then be achieved in one step via a 'tetrahedral' transition structure containing an $\text{Fe}_{\text{heme}}\text{-O-C}_{\text{guan}}$ link resulting from the direct attack of the $\text{Fe}_{\text{heme}}\text{-O}$ moiety at the guanidinium carbon (C_{guan}) of the substrate.

In Chapter 5, the interaction of the nitric oxide ions NO^+ and NO^- with benzene (C_6H_6) and the aromatic *R*-groups of the amino acids, phenylalanine (Phe), tyrosine (Tyr), histidine (His) and tryptophan (Trp), have been examined. In particular, the structures and complexation energies of the resulting half-sandwich $\text{Ar}\cdots\text{NO}^{+/-}$ and sandwich $[\text{Ar}\cdots\text{NO}\cdots\text{Ar}]^{+/-}$ complexes have been considered. For the $\text{Ar}\cdots\text{NO}^+$

complexes, the presence of an electron rich heteroatom within or attached to the ring is not found to preclude the cation $\cdots\pi$ bound complex from being the most stable. Furthermore, unlike the anionic complexes, the $\pi\cdots\text{cation}\cdots\pi$ ($[\text{Ar}\cdots\text{NO}\cdots\text{Ar}]^+$) complexes do not correspond to a 'doubling' of the parent half-sandwich.

In Chapter 6, the ongoing investigation into the catalytic mechanism of MsrB is presented. Thus far, it has been found that the formation of the enzyme-bound sulfurane intermediate occurs via the concomitant proton transfer from a histidine with the nucleophilic attack of a cysteine on the sulfur of methionine sulfoxide. Interestingly, formation of such a sulfurane enhances the basicity of the substrate hydroxyl group, encouraging the addition of a second proton to remove this oxygen from methionine sulfoxide as water and generate an enzyme bound methionine.

Dedication

This work is dedicated to my family.

Acknowledgments

First and foremost, I would like to thank my supervisor Dr. James W. Gauld for providing me the opportunity to work in this research group for the past 5 years. His guidance, attention to details and professional attitude have helped me develop and strengthen many skills that will be needed for future endeavours. In addition, his two-minute break emails and the discussions on various topics were always appreciated.

I would also like to thank my committee members, Dr. Sam Johnson, Dr. Pierre Boulos, and Dr. James Green for taking the time to read and evaluate this work.

I am also grateful for all of the support and assistance that has come from all of the members of the Gauld research group, past and present. In particular, I would like to thank Haining Liu for not only ensuring my research was “interesting” but also for his comic relief (knowingly or not). I would also like to thank Dr. Kyung-Bin Cho and Cristina Baciu who both had a great influence on my development as a computational chemist. Outside of the research group, I would like to thank all of the people in the chemistry and biochemistry department for their help in taking my mind off chemistry, whether it was through sports or Shawarma, it was always appreciated.

I would like to thank my family for their patience, support, and generosity over the years. Last, but not least, I would like to thank Katie Sykes for her constant support and encouragement that have helped me through all of the tough times in the last few years.

Thank you all for everything!

Statement of Originality

I declare that the work reported in this thesis is my own and has not been submitted for any other degree. The material in Chapter 5 was reproduced with permission from Robinet, J. J.; Baciú, C.; Cho, K. -B.; Gauld, J. W. *J. Phys. Chem. A* **2007**, *111*, 1981. Copyright 2007 American Chemical Society.

Jesse J. Robinet

Table of Contents

Approval Page	ii
Abstract	iii
Dedications	v
Acknowledgements	vi
Statement of Originality	vii
List of Tables	xii
List of Figures	xiii
List of Schemes	xviii
List of Appendices	xx
List of Abbreviations and Symbols	xxii
Chapter 1 Introduction	1
References	4
Chapter 2 Theoretical Methods	6
2.1 Introduction	6
2.2 The Schrödinger Equation	6
2.3 The Born-Oppenheimer Approximation	8
2.4 The Orbital Approximation	8
2.5 Basis Set Expansion	10
2.6 The Variational Theorem	10
2.7 Hartree-Fock Theory	11
2.8 Restricted and Unrestricted Hartree-Fock Theory	12
2.9 Electron Correlation	13
2.10 Configuration Interactions	14
2.11 Møller-Plesset Perturbation Theory	14

2.12 Density Functional Theory	16
2.12.1 <i>Hohenberg-Kohn Theorem</i>	16
2.12.2 <i>Kohn-Sham Theorem</i>	17
2.12.3 <i>The B3LYP Hybrid Functional</i>	18
2.14 Basis Sets	19
2.14.1 <i>Split-Valence Basis Sets</i>	19
2.14.2 <i>Polarization Basis Sets</i>	20
2.14.3 <i>Diffuse Functions</i>	20
2.14.4 <i>Pople Diagram</i>	21
2.14.5 <i>Compound Methods</i>	21
2.15 Basis Set Superposition Error	22
2.16 Calculations	23
2.17 Potential Energy Surfaces	24
2.18 Solvation	25
2.18 Technical Aspects and Units	26
References	27
Chapter 3 A DFT Investigation on the Mechanism of the Deacetylation	
Reaction Catalyzed by LpxC	30
3.1 Introduction	30
3.2 Computational Methods	33
3.3 Results and Discussion	35
3.3.1 <i>The Water-Assisted Deacetylation Mechanism</i>	35
3.3.2 <i>The Active Site-Bound Substrate Complex</i>	37
3.3.3 <i>The LpxC Catalyzed Deacetylation Reaction</i>	39
3.3.4 <i>Overall Mechanism</i>	46
3.4 Conclusions	46
References	47

Chapter 4	A DFT Investigation on the Mechanism of the Second Half- Reaction of Nitric Oxide Synthase.....	51
	4.1 Introduction.....	51
	4.2 Computational Methods	54
	4.3 Results and Discussion	55
	4.3.1 <i>Substrate Bound Active Site and Initial Reaction Step ...</i>	55
	4.3.2 <i>Possible Reactions of the $Fe_{\text{heme}}\text{-(H)OOH}$ Intermediate.....</i>	56
	4.3.3 <i>Formation of 'Compound I' from $Fe_{\text{heme}}\text{-(H)OOH}$ Intermediate 3</i>	59
	4.3.4 <i>Formation of the Final Products, Citrulline and NO</i>	62
	4.4 Conclusions.....	65
	References	66
Chapter 5	A Computational Study on the Interaction of the Nitric Oxide Ions NO^+ and NO^- with the Side Groups of the Aromatic Amino Acids	70
	5.1 Introduction.....	70
	5.2 Computational Methods	72
	5.3 Results and Discussion	73
	5.3.1 <i>Assessment of Computational Methods.....</i>	73
	5.3.2 <i>$Ar\cdots NO^+$ Complexes</i>	82
	5.3.3 <i>$Ar\cdots NO^-$ Complexes.....</i>	85
	5.3.4 <i>$[Ar\cdots NO\cdots Ar]^+$ Complexes.....</i>	87
	5.3.5 <i>$[Ar\cdots NO\cdots Ar]^-$ Complexes</i>	91
	5.4 Conclusions.....	93
	References	95

Chapter 6	An Ongoing Investigation into the Mechanism of Methionine Sulfoxide Reductase B	99
	6.1 Introduction	99
	6.2 Computational Methods	103
	6.3 Results and Discussion	106
	<i>6.3.1 Non-Covalent Binding of the Substrate within the Active Site</i>	106
	<i>6.3.2 Covalent Binding of the Substrate within the Active Site</i>	107
	<i>6.3.3 Regeneration of the 'Active Site Bound' Methionine</i>	111
	<i>6.3.4 Ongoing and Future Work</i>	116
	6.4 Preliminary Conclusions	116
	References	117
Chapter 7	Conclusions	120
Vita Auctoris	123
Appendices	CD

List of Tables

Table 5.1	Selected Optimized Distances (Å) and Complexation Energy (kJ mol ⁻¹) of C ₆ H ₆ ⋯NO ⁺ (2A) Obtained Using the B3LYP and MP2 Methods in Combination with a Range of Basis Sets.....	74
Table 5.2	Optimized N—O Bond Distances (Å) for Nitric Oxide and its Mono-Ions Obtained Using the B3LYP and MP2 Methods in Combination with a Range of Basis Sets	76
Table 5.3	Calculated Adiabatic Ionization Energies (IE's) for NO, C ₆ H ₆ , and R-Groups ^b of the Aromatic Amino Acids and Corrected Complexation Energies (kJ mol ⁻¹) for the Ar⋯NO ^{+/-} and Ar⋯NO ^{+/-} ⋯Ar Complexes	78
Table 5.4	Selected Optimized Distances (Å) and Complexation Energy (kJ mol ⁻¹) Obtained at Various Levels of Theory for the NO ⁻ Bound Side-On C ₆ H ₆ ⋯NO ⁻ Complex 2B	79
Table 5.5	Selected Optimized Distances (Å) and Complexation Energies (kJ mol ⁻¹) Obtained at Various Levels of Theory for the NO ⁻ Bound N-End-On C ₆ H ₆ ⋯NO ⁻ Complex	80

List of Figures

Figure 1.1	Schematic illustration showing the structure of selected amino acids at pH 7. The amino acid backbone is highlighted in red, while the functional groups of the amino acids that exemplify the basis for classification are shown in blue	1
Figure 1.2	Schematic illustration of selected cofactors. Inorganic atoms are highlighted in red	2
Figure 2.1	Illustration of a Pople Diagram	21
Figure 2.2	Illustration indicating key features of a potential energy surface for the reaction of A and B to produce C and D	25
Figure 2.3	Diagram of the cavity created for the solute in Tomasi's PCM solvation model.....	26
Figure 3.1	Potential energy surfaces for water-assisted hydrolysis of the amide bond of <i>N</i> -methylacetamide via concerted (red dashed) and step-wise (blue solid) mechanisms.....	36
Figure 3.2	Lowest energy active site-bound substrate complexes: (1A) substrate bound between a Zn ²⁺ -bound H ₂ O and Thr191 residue, (1B) substrate bound between His265-H ⁺ and a Zn ²⁺ bound H ₂ O. Select optimized distances (Å) are also shown. [Zn (purple); C (gray); N (blue); O (red); H (white)].....	38
Figure 3.3	Potential energy surface for the overall reaction mechanism of LpxC. Key residues of minima are schematically shown in order to highlight changes in the system during the reaction. For clarity, the Thr191 and Glu78-H ⁺ residues have been omitted	39
Figure 3.4	Optimized geometries of transition structure TS1 and <i>gem</i> -diolate intermediate 2 arising from the addition of the hydroxide ion at the	

- substrate's carbonyl carbon. Select optimized distances (Å) are also shown. [Zn (purple); C (gray); N (blue); O (red); H (white)] 41
- Figure 3.5** Optimized geometries of the transition structures and intermediates arising from proton transfer from His265–H⁺ to the amino nitrogen of the intermediate (**TS2** and **3**), as well as reorientation of His265 within the active site (**TS3** and **4**). Select optimized distances (Å) are also shown. [Zn (purple); C (gray); N (blue); O (red); H (white)] 43
- Figure 3.6** Optimized geometries of the transition structure and the resulting product complex associated with the transfer of the substrate's hydroxyl proton to His265. Select optimized distances (Å) are also shown. [Zn (purple); C (gray); N (blue); O (red); H (white)] 45
- Figure 4.1** Schematic potential energy surfaces obtained for possible reactions of the Fe_{heme}-(H)O—OH intermediate **2**. Relative energies shown in kcal mol⁻¹ 57
- Figure 4.2** Optimized structures of the singlet state intermediates and transition structures shown in Figure 1 arising from the reaction of the Fe_{heme}-(H)O—OH intermediate **2**. Selected optimized distances (Å) and spin densities (in brackets) are also shown. [Fe (purple); S (yellow); C (gray); N (blue); O (red); H (white)] 58
- Figure 4.3** Schematic potential energy surface for the formation of Compound I from the Fe_{heme}-(H)O—OH intermediate **3**. Relative energies shown in kcal mol⁻¹ 60
- Figure 4.4** Optimized structures of the singlet state intermediates and transition structures shown in Figure 4.3 arising from the reaction of the Fe_{heme}-(H)O—OH intermediate **3**. Selected optimized

- distances (Å) and spin densities (in brackets) are also shown. [Fe (purple); S (yellow); C (gray); N (blue); O (red); H (white)] 61
- Figure 4.5** Schematic potential energy surface for the overall mechanism of the second half-reaction of NOSs. Relative energies shown in kcal mol⁻¹ 63
- Figure 4.6** Optimized structures of the triplet state intermediate **5** (**5**³) and corresponding transition structure (**TSS**³) for formation of the triplet product (**6**³) complex. Selected optimized distances (Å) and spin densities (in brackets) are also shown. [Fe (purple); S (yellow); C (gray); N (blue); O (red); H (white)] 65
- Figure 5.1** Models used in this present study for the side (R-) groups of the aromatic amino acids (1A) phenylalanine (Phe), (1B) tyrosine (Tyr), (1C) histidine (His) and (1D) tryptophan (Trp). [C (gray); N (blue); O (red); H (white)] 72
- Figure 5.2** Illustration of the optimized structures of (**2A**) C₆H₆···NO⁺ and C₆H₆···NO⁻ with NO⁻ bound (**2B**) side-on or N-end-on via (**2C**) two hydrogen bonds or (**2D**) one hydrogen bond. [C (gray); N (blue); O (red); H (white)] 74
- Figure 5.3** Optimized structures (B3LYP/6-311G(2d,p)) with selected distances (Å) for the Ar···NO⁺ complexes where Ar is (**3A**) Phe, (**3B**) Tyr, (**3C**₁) His with NO⁺ bound via a ring nitrogen's lone pair, (**3C**₂) His with NO⁺ bound via its π-system, and (**3D**) Trp. [C (gray); N (blue); O (red); H (white)] 82
- Figure 5.4** Optimized structures (B3LYP/6-311G(2d,p)) with selected distances (Å) for the lowest energy Ar···NO⁻ complexes where Ar is (**4A**) Phe, (**4B**) Tyr, (**4C**) His and (**4D**) Trp. [C (gray); N (blue); O (red); H (white)] 85

- Figure 5.5** Optimized structures (B3LYP/6-311G(2d,p)) with selected distances (Å) of the $[\text{Ar}\cdots\text{NO}\cdots\text{Ar}]^+$ complexes where Ar is (**5A**) C_6H_6 , (**5B**) Phe, (**5C**) Tyr, (**5D₁**) His when bound via both ring nitrogens' lone-pairs, (**5D₂**) His when bound via both rings π -systems, and (**5E**) Trp. [C (gray); N (blue); O (red); H (white)]..... 88
- Figure 5.6** The highest occupied molecular orbital (HOMO) for the optimized structures of the $\text{Ar}\cdots\text{NO}^+\cdots\text{Ar}$ sandwich complexes where Ar is (**5A_{HOMO}**) C_6H_6 and (**5B_{HOMO}**) Phe. [C (gray); N (blue); O (red); H (white)]..... 90
- Figure 5.7** Optimized structures (B3LYP/6-311G(2d,p)) with selected distances (Å) of the $[\text{Ar}\cdots\text{NO}\cdots\text{Ar}]^-$ complexes where Ar is (**7A**) C_6H_6 , (**7B**) Phe, (**7C**) Tyr, (**7D**) His, and (**7E**) Trp. [C (gray); N (blue); O (red); H (white)]..... 93
- Figure 6.1** Optimized geometry of the lowest energy structures of the non-covalently bound substrate within the active site models M_{Med} and M_{Lrg} . [S (yellow); C (gray); N (blue); O (red); H (white)]..... 107
- Figure 6.2** Potential energy surface and schematic illustration of key intermediates for the reduction of methionine-R-sulfoxide by MsrB to a sulfonium cation intermediate. Only residues directly involved in the catalysis are shown in the intermediates for clarity. The blue and red PES's correspond to M_{Med} and M_{Lrg} , respectively. 108
- Figure 6.3** The highest occupied (HOMO) and lowest unoccupied (LUMO) molecular orbitals of DMSO and $\text{DMSO}-\text{H}^+$ 109
- Figure 6.4** Optimized geometries of the transition structure (TS1_{Med}) and intermediate (2_{Med}) resulting from the concomitant proton transfer and nucleophilic attack of the thiolate on DMSO to form an

	enzyme bound sulfurane. [S (yellow); C (gray); N (blue); O (red); H (white)]	110
Figure 6.5	Optimized geometries of the intermediates 2_{Lrg} and 3_{Lrg} . [S (yellow); C (gray); N (blue); O (red); H (white)]	111
Figure 6.6	Potential energy surface of the intramolecular rearrangement and OH^- transfer of a sulfurane to generate a sulfenic acid and dimethyl sulfide	112
Figure 6.7	Optimized structures for transfer of the OH^- group closer proximity to the sulfur of Cys495. [S (yellow); C (gray); N (blue); O (red); H (white)]	114
Figure 6.8	Optimized geometries of the transition structure ($\text{TS}_{2_{\text{Med}}}$) and intermediate (3_{Med}), due to the transfer of a second proton to the sulfurane's OH^- moiety to form a sulfonium cation intermediate. [S (yellow); C (gray); N (blue); O (red); H (white)]	115

List of Schemes

Scheme 3.1	LpxC catalyses the conversion of UDP-3- <i>O</i> -(<i>R</i> -3-hydroxymyristoyl)- <i>N</i> -acetylglucosamine to UDP-3- <i>O</i> -(<i>R</i> -3-hydroxymyristoyl)glucosamine and acetate.....	30
Scheme 3.2	Proposed mechanisms for the deacetylation reaction catalyzed by LpxC in which: (a) Glu78 acts as both the general acid and base and (b) His265–H ⁺ and Glu78 act as the general acid and base, respectively.....	33
Scheme 3.3	Schematic illustration of the LpxC active site model used in this chapter. Atoms held fixed throughout optimizations are bolded and coloured red.	34
Scheme 4.1	The overall mechanism catalysed by nitric oxide synthases illustrating its two component half-reactions (R = –(CH ₂) ₂ CH(NH ₂)COOH).....	52
Scheme 4.2	Summary of common features of the various proposed mechanisms for the second half-reaction in which NO is formed via a tetrahedral intermediate. Note, proposed ionization and protonation states may vary.....	53
Scheme 4.3	Schematic depiction of the active site of NOS as modeled in this chapter. Atoms highlighted in red were held fixed in the crystal structure position throughout the optimizations.....	55
Scheme 6.1	Illustration of the methionine sulfoxide isomers produced via oxidation and the selectivity of the methionine sulfoxide reduction enzymes MsrA and MsrB.....	100
Scheme 6.2	Key steps of the proposed mechanism for the Msr enzymes in the reduction of MetSO via a sulfenic acid intermediate.....	101

Scheme 6.3	Proposed reaction mechanism for MetSO reduction via a second protonation and a direct thiol attack	102
Scheme 6.4	Schematic illustration and optimized substrate structure (1_{Med}) of the active site of MsrB for the M _{Med} model calculations. Fixed points are coloured red and bolded. [S (yellow); C (gray); N (blue); O (red); H (white)].....	104
Scheme 6.5	Schematic illustration and optimized substrate structure (1_{Lrg}) of the active site of MsrB for the M _{Lrg} model calculations. Fixed points are coloured in red and bolded. [S (yellow); C (gray); N (blue); O (red); H (white)].....	105

List of Appendices (on CD)

Appendix A

Table A.1 Optimized xyz-coordinates obtained at the PB-PCM-B3LYP/LACVP** level of theory and solution phase energies (h) obtained at the PB-PCM-B3LYP/LACV3P+**//PB-PCM-B3LYP/LACVP** level of theory for all species considered in this present study

Appendix B

Figure B.1 Optimized structures of the high-energy transition states. (S1A) Cleavage of O–O bond from **3A**. (S1B) Attack of Fe_{heme}–O oxygen at N^o from **5**¹. Selected interaction distances (Å) and spin densities in brackets are shown. [Fe (purple); S (yellow); C (gray); N (blue); O (red); H (white)]

Figure B.2 Optimized structure of compound I multiplicity 5 (S2), showing selected interaction distances (Å) and spin densities in brackets. [Fe (purple); S (yellow); C (gray); N (blue); O (red); H (white)]

Table B.1 Optimized xyz-coordinates obtained at the B3LYP/LACVP level of theory for all species considered in Chapter 4

Table B.2 Calculated energies (h) for all structures considered in Chapter 4. LACVP optimization energy (E), LACV3P** single point energy (E_{SP}), LACVP solvation energy (E_{solv}), and thermal correction to Gibbs free energy (ΔE_{Therm})

Appendix C

Figure C.1 Mulliken atomic charges calculated at the B3LYP/6-311G(d,p) level of theory of the carbons in toluene, with hydrogens summed into heavy atoms

Figure C.2 The highest intramolecular bonding orbital for NO^+ binding to the two Ar rings in the $\text{Ar}\cdots\text{NO}^+\cdots\text{Ar}$ sandwich complexes where Ar is (**5C_{HOMO}**) Tyr and (**5D_{1 HOMO-2}**) His with NO^+ bound via the rings N1 lone pairs and (**5D_{2 HOMO}**) His with NO^+ bound via the rings π -systems. [C (gray); N (blue); O (red); H (white)]

Table C.1 Optimized xyz-coordinates, electronic energies (h), ZPVE corrections, BSSE corrections and $\langle S^2 \rangle$ values for all species considered in Chapter 5

Appendix D

Table D.1 Optimized xyz-coordinates for all species considered in Chapter 6

Table D.2 Calculated energies (h) for all structures considered in Chapter 6. Optimization energy (E), single point energy (E_{SP}) and solvation energy (E_{solv})

List of Abbreviations and Symbols

Ar	Aromatic
Asn	Asparagine
Asp	Aspartate
B	Becke's 88 exchange functional
B3LYP	Becke's three parameter hybrid functional
BSSE	Basis Set Superposition Error
cGMP	Cyclic Guanosine Monophosphate
C ₆ H ₆	Benzene
CI	Configuration Interaction
CID	Configuration Interaction with Doubles
CISD	Configuration Interaction with Singles and Doubles
CP	Counterpoise Correction
Cys	Cysteine
DFT	Density Functional Theory
FAD	Flavin Adenine Dinucleotide
FMN	Flavin Mononucleotide
GGA	Generalized Gradient Approximation
Glu	Glutamate
GSNO	S-Nitrosoglutathione
GTF	Gaussian-Type Functions
H ₄ B	(6R)-5,6,7,8-tetrahydro-L-biopterin
HF	Hartree-Fock
His	Histidine
HOMO	Highest Occupied Molecular Orbital
IE	Ionization Energy
IEF	Integral Formalism Equation

LCAO	Linear Combination of Atomic Orbitals
LDA	Local Density Approximation
LpxC	UDP-3- <i>O</i> -(<i>R</i> -3-hydroxymyristoyl)- <i>N</i> -acetylglucosamine deacetylase
LUMO	Lowest Unoccupied Molecular Orbital
LYP	Lee-Yang-Parr correlation functional
Met	Methionine
MetSO	Methionine Sulfoxide
MPn	n^{th} order Møller-Plesset
Msr	Methionine Sulfoxide Reductase
MsrA	Methionine Sulfoxide Reductase A
MsrB	Methionine Sulfoxide Reductase B
NADPH	Nicotinamide Adenine Dinucleotide
NHA	N^{ω} -hydroxy-L-arginine
NO	Nitric Oxide
NO^+	Nitrosium Cation
NO^-	Nitroxyl Anion
NOS	Nitric Oxide Synthase
PB	Poisson-Boltzmann
PCM	Polarizable Continuum Method
PDB	Protein Data Bank
PES	Potential Energy Surface
Phe	Phenylalanine
RHF	Restricted Hartree-Fock
ROS	Reactive Oxygen Species
RSNO	<i>S</i> -Nitrosothiols
SCF	Self-Consistent Field

STO	Slater-Type Orbitals
Thr	Threonine
Trp	Tryptophan
Trx	Thioredoxin
Tyr	Tyrosine
UDP	Uridine Diphosphate
UHF	Unrestricted Hartree-Fock
UV	Ultra Violet
VWN	Vosko-Wilk-Nusair
ZPVE	Zero Point Vibrational Energy

\hat{H}	Hamiltonian operator
E	Energy
ψ	Wave function
\hat{T}	Kinetic energy operator
\hat{V}	Potential energy operator
∇^2	Laplacian operator
r	Distance between two particles
q_i	Coordinates of particle i
χ_i	i^{th} spin orbital
c_{ui}	Molecular orbital coefficient
ϕ	Basis function
ψ_{approx}	Trial wave function
F_{uv}	Fock matrix
S_{uv}	Overlap matrix
ϵ_i	Orbital energy for the i^{th} molecular orbital
λ	Dimensionless parameter
ρ	Density
E^T	Kinetic energy term
E^V	Potential energy term
E^J	Repulsion energy term
E^{XC}	Exchange-correlation energy term
ϵ	Dielectric constant
\AA	Ångstrom

Chapter 1

Introduction

Biomolecules are generally defined as chemical compounds that are synthesized by the cell and are essential to all living organisms.¹ There are four main classes of biomolecules: nucleic acids, proteins, lipids and carbohydrates. Proteins have attracted considerable attention due to the fact that they are the 'work horses' of the cell. In particular, proteins are found to function in numerous cellular activities including structure, communication, storage, transportation, and catalysis.²

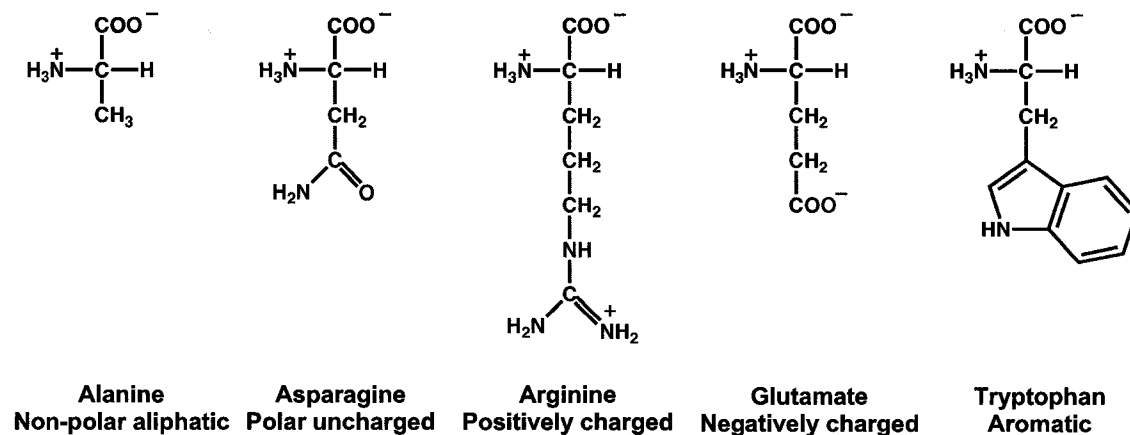


Figure 1.1. Schematic illustration showing the structure of selected amino acids at pH 7. The amino acid backbone is highlighted in red, while the functional groups of the amino acids that exemplify the basis for classification are shown in blue.

Proteins are polymers assembled from various combinations of the twenty naturally occurring amino acids.³ Structurally, amino acids consist of a central carbon atom bound by an amino group, a carboxylic group, and a functional (R-) group as shown in Figure 1.1. Categorization of the amino acids based on the properties of their

unique R-groups results in five classes: (i) non-polar, (ii) neutral polar, (iii) positively charged (basic), (iv) negatively charged (acidic), and (v) aromatic amino acids. Examples of each type is given in Figure 1.1.³ It is of utmost importance to note that it is the presence, arrangement and interactions of the amino acids' functional groups within a protein that allow for the distinct chemical properties of proteins.

In spite of the array of chemical properties provided by the amino acids, many proteins also rely on other molecules to aid them in their various roles. These additional properties may be offered by non-protein components known as cofactors.³ Cofactors can be non-covalently or covalently bound to the protein (the latter being known as a prosthetic group). Many cofactors are organic molecules, e.g., tetrahydrobiopterin. In the case of metalloproteins, at least one cofactor contains a metal ion, often incorporated within a molecule, e.g. heme. Figure 1.2 provides examples of some organic and inorganic cofactors.

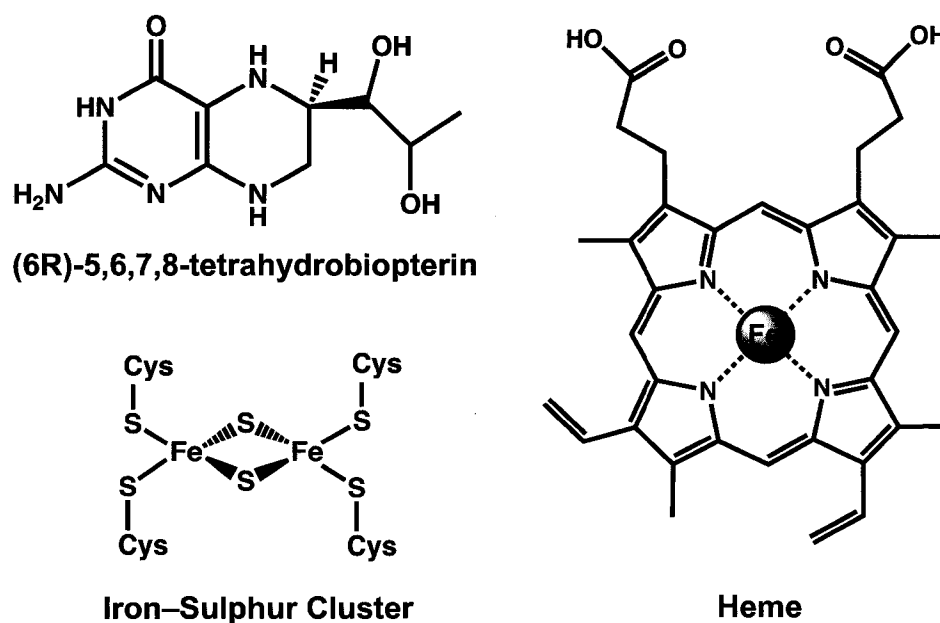


Figure 1.2. Schematic illustration of selected cofactors. Inorganic atoms are highlighted in red.

The role and function of metal ions in proteins is of particular interest due to the fact that they are often found to be essential for ensuring the proper structure and function of many proteins, in particular those that are able to catalyse reactions, enzymes.² Enzymes are biomolecular catalysts that are used to accelerate the rate of chemical reactions within the cell.⁴ They have been observed to enhance the rate of reactions by a factor of 10^{15} , thereby catalysing reactions that would normally take 30 000 000 years in only one second!⁵ Interestingly, it has been found that approximately 40% of all enzymes contain a metal ion.^{6,7}

Enzymes employ metal ions in numerous functions, namely structural and chemical roles. Structurally, metals ions have been shown to ensure the proper folding of proteins through coordination to the amino acids.⁷⁻⁹ Interestingly, metal ions are also known to participate in non-covalent interactions, notably cation- π interactions, with aromatic systems and have been found to form 'sandwich' type complexes with two aromatic species.^{10,11} Chemically, metal ions often assume a direct role in the enzyme-catalyzed reaction mechanism. A reaction mechanism is the sequence of step-wise reactions a system undergoes as a reaction progresses from reactants to products. Specifically, metal ions are most often incorporated in a protein's active site, the region of the protein where the catalysis occurs. One manner in which metal ions participate in catalysis is to bind and stabilize ligands within the active site. In addition to orienting the ligand, metal ions can also have a polarizing effect on such ligands, which may serve to alter the ligand's chemical properties facilitating the reaction.^{9,12-15} Furthermore, many transition metal ions participate in redox reactions.¹⁶ In such reactions, the metal ion acts as an oxidizing or reducing agent by donating or accepting electrons.¹⁷

The involvement of metal ions in biochemical systems is ubiquitous. Thus, understanding metal ion-protein interactions and their involvement in the catalytic

mechanisms of such enzymes is critical. Such knowledge may aid to achieve a greater overall understanding of the chemistry of proteins and their implementation of cofactors as well as provide insights into the development of effective drugs and the production of more efficient synthetic catalysts.

The work presented in this thesis focuses on elucidating the potential catalytic mechanisms of the metalloenzymes UDP-3-*O*-(*R*-3-hydroxymyristoyl)-*N*-acetylglucosamine deacetylase (LpxC) and nitric oxide synthase (NOS), as well as the non-metal redox active enzyme methionine sulfoxide reductase B (MsrB). In addition, the metallo-like complexation of the nitrosium cation (NO^+) to benzene and the side chains of the aromatic amino acids, phenylalanine, tyrosine, histidine and tryptophan is also examined, as well as the interactions formed by the nitroxyl anion (NO^-) with the aforementioned molecules.

References

- (1) McKee, T.; McKee, J. R. *Biochemistry: The Molecular Basis of Life*, 3rd ed.; McGraw-Hill Companies, Inc.: Toronto, 2003.
- (2) Whitford, D. *Proteins: Structure and Function*; John Wiley & Sons, Ltd.: Etobicoke, 2005.
- (3) Nelson, D. L.; Cox, M. M. *Lehninger: Principles of Biochemistry*, 4th ed.; W. H. Freeman and Company: New York, 2005.
- (4) Kraut, D. A.; Carroll, K. S.; Herschlag, D. *Annu. Rev. Biochem.* **2003**, *72*, 517.
- (5) Schramm, V. L. *Annu. Rev. Biochem.* **1998**, *67*, 693.
- (6) Voet, D.; Voet, J. G.; Pratt, C. W. *Fundamentals of Biochemistry*, Upgrade ed.; John Wiley & Sons, Inc.: Toronto, 2002.
- (7) Wilson, C. J.; Apiyo, D.; Wittung-Stafshede, P. *Q. Rev. Biophys.* **2005**, *37*, 1.
- (8) Vallee, B. L.; Coleman, J. E.; Auld, D. S. *Proc. Natl. Acad. Sci. USA* **1991**, *88*, 999.

-
- (9) Vallee, B. L.; Auld, D. S. *Biochemistry* **1990**, *29*, 5647.
- (10) Dougherty, D. A. *Science* **1996**, *271*, 163.
- (11) Ma, J. C.; Dougherty, D. A. *Chem. Rev.* **1997**, *97*, 1303.
- (12) Lipscomb, W. N.; Sträter, N. *Chem. Rev.* **1996**, *96*, 2375.
- (13) McCall, K. A.; Huang, C.-C.; Fierke, C. A. *J. Nutr.* **2000**, *130*, 1437S.
- (14) Housecroft, C. E.; Sharpe, A. G. *Inorganic Chemistry*; Pearson Education, Ltd.: New York, 2001.
- (15) Hernick, M.; Fierke, C. A. *Arch. Biochem. Biophys.* **2005**, *433*, 71.
- (16) Bott, A. W. *Curr. Separations* **1999**, *18*, 47.
- (17) Atkins, P.; Jones, L. *Chemical Principles: The Quest for Insight*, 3rd ed.; W. H. Freeman and Company: New York, 2005.

Chapter 2

Theoretical Methods

2.1 Introduction

An alternative approach to experimentally investigating the properties of chemical systems is to study them using computers. This discipline of chemistry is known as computational chemistry. An attractive feature of computational chemistry is that reactive, short-lived species, that may not be observable experimentally, are as easily studied as stable, long-lived ones. Consequently, the properties of highly reactive species or transition states can be investigated using this technique. The methods employed in computational chemistry stem from quantum chemistry. Thus, in this chapter, a brief overview of some of the necessary theorems of quantum chemistry and the computational methods used throughout this thesis are discussed.

2.2 The Schrödinger Equation

The central equation in quantum chemistry is the time-independent Schrödinger equation:¹

$$\hat{H}\psi = E\psi \quad (2.1)$$

where \hat{H} is the Hamiltonian operator, E is the energy of the system, and ψ is the wave function of the total system. The wave function contains all possible information regarding the system and is a function of the particle's coordinates.² The wave function

cannot be directly measured; however, its probability density, $|\psi|^2$, can be experimentally observed as it is the electron distribution.² Importantly, the Schrödinger equation can extract the energy of the system from the wave function through the use of the Hamiltonian operator.

The Hamiltonian Operator may be divided into two terms, a kinetic energy term (\hat{T}) and a potential energy term (\hat{V}):²

$$\hat{H} = \hat{T} + \hat{V} \quad (2.2)$$

However, the Hamiltonian operator used for molecules, the molecular Hamiltonian, may be written as:²

$$\hat{H} = -\sum_{i=1}^{N_E} \frac{1}{2} \nabla_i^2 - \sum_{\alpha=1}^{N_N} \frac{1}{2M_\alpha} \nabla_\alpha^2 - \sum_{i=1}^{N_E} \sum_{\alpha=1}^{N_N} \frac{Z_\alpha}{r_{i\alpha}} + \sum_{i=1}^{N_E} \sum_{j>i}^{N_E} \frac{1}{r_{ij}} + \sum_{\alpha=1}^{N_N} \sum_{\beta>\alpha}^{N_N} \frac{Z_\alpha Z_\beta}{r_{\alpha\beta}} \quad (2.3)$$

where α and β represent the nuclei, while i and j represent the electrons. The first two terms in equation 2.3 are the kinetic energy terms for the electrons and nuclei, respectively. The third term is the potential for the nuclear-electron attractions, whereas the fourth and fifth terms are the potential energy terms for electron-electron and nuclear-nuclear repulsions, respectively.

Due to the complexity of the Hamiltonian operator, the Schrödinger equation cannot be solved exactly, with the exception of hydrogen and hydrogen-like atoms, e.g. He^+ and Li^{2+} .² As a result some approximations must be invoked, in order to simplify the Hamiltonian, thereby enabling it to be applicable to larger chemical systems.

2.3 The Born-Oppenheimer Approximation

The first approximation arises from the fact that nuclei are significantly heavier than electrons and as a result move much slower. The electrons can essentially be thought of as moving in a field of fixed nuclei. This approximation is the Born-Oppenheimer Approximation.³ It allows the wave function to be written as the product of electronic and nuclear wave functions:

$$\psi(q_i, q_\alpha) = \psi(q_i; q_\alpha) \psi(q_\alpha) = \psi_{el} \psi_{Nuc} \quad (2.4)$$

where q_i and q_α are the electronic and nuclear coordinates, respectively.

In addition, the assumption that the nuclei are stationary simplifies the Hamiltonian as the kinetic energy of the nuclei is now zero and the potential energy term for the nuclear-nuclear interactions is reduced to a constant. The resulting Hamiltonian is referred to as the electronic Hamiltonian:

$$\hat{H}_{el} = -\sum_{i=1}^{N_E} \frac{1}{2} \nabla_i^2 - \sum_{i=1}^{N_E} \sum_{\alpha=1}^{N_N} \frac{Z_\alpha}{r_{i\alpha}} + \sum_{i=1}^{N_E} \sum_{j>i}^{N_E} \frac{1}{r_{ij}} \quad (2.5)$$

Although the electronic Hamiltonian (2.5) is not as complex as the original Hamiltonian (2.3), it remains difficult to solve except in the case of the simplest chemical systems.

2.4 The Orbital Approximation

The orbital approximation allows for further simplification of the electronic wave function by assuming the motion of each electron is independent of the others. As such, each electron is assigned a separate one-electron wave function or spin-orbital (χ_i). This spin-orbital of each electron is the product of a spatial function, a function of the coordinates of the i^{th} electron $\psi_i(x_i, y_i, z_i)$ (e.g., a molecular orbital), and a spin function, α

and β . Thus, the wave function of an n -electron system can be constructed by the product of the spin-orbitals for the n electrons:⁴⁻⁶

$$\psi_{product} = \chi_1(1)\chi_2(2)\dots\chi_n(n) \quad (2.6)$$

This new wave function is known as a Hartree-product wave function. Implementation of the Hartree-product wave function helps reduce the difficulties associated when dealing with the total wave function, as now it is simply a series of one electron problems.

However, the Hartree-product is not a suitable wave function, as it does not take into account the indistinguishability of electrons. In addition, it does not satisfy the Pauli Exclusion Principle, which states that the wave function of an n -electron system must be anti-symmetric. That is, upon interchange of any two electrons, the wave function must change signs.⁴

To satisfy these requirements, the wave function may be written as a determinant of the spin orbitals. This is referred to as a Slater determinant:^{7,8}

$$\psi = \frac{1}{\sqrt{n!}} \begin{vmatrix} \chi_1(1) & \chi_2(1) & \cdots & \chi_n(1) \\ \chi_1(2) & \chi_2(2) & \cdots & \chi_n(2) \\ \vdots & \vdots & & \vdots \\ \chi_1(n-1) & \chi_2(n-1) & \cdots & \chi_n(n-1) \\ \chi_1(n) & \chi_2(n) & \cdots & \chi_n(n) \end{vmatrix} \quad (2.7)$$

where $1/\sqrt{n!}$ is a normalization constant. This constant ensures that the wave function is normalized and satisfies the equation:

$$\int \psi^* \psi d\tau = 1 \quad (2.8)$$

where ψ^* is the complex conjugate of ψ . Equation 2.8 verifies that the probability of finding an electron over its entire possible range equals one.²

2.5 Basis Set Expansion

Recall from above that a molecular orbital is the spatial function, ψ_i , of the spin orbital, χ_i . These molecular orbitals can be expressed as a linear combination of one-electron functions, known as basis functions:²

$$\psi_i = \sum_{\mu=1}^N c_{\mu i} \phi_{\mu} \quad (2.9)$$

where ϕ_{μ} are basis functions and $c_{\mu i}$ is the molecular orbital coefficient for the μ^{th} basis function in the i^{th} molecular orbital, ψ_i . In theory, the basis functions should form a mathematically complete set; however, this would require an infinite number of basis functions, which is not feasible in practice. Therefore, only a limited number of basis functions are used. It should be noted that as the number of basis functions increases, ψ_i improves. In addition, when the ϕ_{μ} are considered as the atomic orbitals of the chemical system, ψ_i is referred to as a linear combination of atomic orbitals (LCAO).

2.6 The Variational Theorem

The Variational Theorem states that the energy, E_{approx} , obtained from any trial wave function, ψ_{approx} , will always be an upper bound to the exact energy, E_{exact} , from the ground-state wave function.² This is shown in the following equation:

$$E_{approx} = \frac{\int \psi_{approx}^* \hat{H} \psi_{approx} d\tau}{\int \psi_{approx}^* \psi_{approx} d\tau} \geq E_{exact} \quad (2.10)$$

Fortuitously, it has been found that even with a poor estimate of the wave function, reasonable energies may be obtained. This occurs since E_{approx} approaches E_{exact} faster than ψ_{approx} approaches ψ_{exact} .² In addition, the Variational Theorem provides a tool in which the quality of the trial wave function can be evaluated. Thus, the best approximate ground-state wave function can be obtained by searching for the trial wave function that minimizes E_{approx} .

2.7 Hartree-Fock Theory

The Hartree-Fock (HF) method serves as the fundamental wave function-based method in computational chemistry. Importantly, it employs the central field approximation, which enables the simplification of the mathematically rigorous electron repulsion term, $1/r_{ij}$. This is achieved via integration of this term. However, as a result the electrons do not interact explicitly, but rather they feel the other electrons in an average way.²

The HF method provides a way to obtain the molecular orbital coefficients, $c_{\mu i}$, used in the basis set expansion, through the Roothaan-Hall equation:^{9,10}

$$\sum_{\mu=1}^N c_{\mu i} (F_{\mu\nu} - \epsilon_i S_{\mu\nu}) = 0 \quad \mu = 1, 2, \dots, N \quad (2.11)$$

where $F_{\mu\nu}$ is the Fock matrix, ϵ_i is the orbital energy of the molecular orbital ψ_i , and $S_{\mu\nu}$ is the overlap matrix, which accounts for the overlap between basis functions. From equation 2.11 it can be seen that the desired molecular orbital coefficients and the Fock matrix are interdependent on each other. Thus, in order to solve for the molecular orbital coefficients, a set of guessed $c_{\mu i}$'s must initially be employed from which an initial Fock

matrix may be formed and used to produce a new set of improved coefficients. This improved set of coefficients is then used to construct a new Fock matrix, so as to further enhance the quality of the coefficients. This evaluation process continues until there is no possible improvement between the old and new coefficients. That is, it has reached a self-consistency. This iterative process to solve for the molecular orbital coefficients and the orbital energies is known as the Hartree–Fock Self-Consistent Field (SCF) procedure.^{4-6,11}

2.8 Restricted and Unrestricted Hartree-Fock Theory

In the Hartree-Fock method described above, all electrons are assigned to molecular orbitals as pairs. Thus, this method is suitable only for those chemical systems where all the electrons are paired, i.e., closed-shell systems. This approach is referred to as restricted Hartree-Fock (RHF) theory.¹² However, some chemical systems have electrons that are unpaired, i.e., open-shell systems, for which the RHF method is inadequate, as it allows for only paired electrons. A common approach taken with open-shell systems is the unrestricted Hartree-Fock (UHF) method, where the alpha and beta electrons are assigned to separate spatial orbitals.¹² Separating the electrons into alpha and beta spins results in two sets of molecular orbital coefficients:

$$\psi_i^\alpha = \sum_{\mu=1}^N c_{\mu i}^\alpha \phi_\mu \quad , \quad \psi_i^\beta = \sum_{\mu=1}^N c_{\mu i}^\beta \phi_\mu \quad (2.12)$$

These are solved via a pair of Roothaan-Hall equations, called the Pople-Nesbet equations:¹³

$$\sum_{\mu=1}^N c_{\mu i}^\alpha (F_{\mu\nu}^\alpha - \epsilon_i^\alpha S_{\mu\nu}) = 0 \quad , \quad \sum_{\mu=1}^N c_{\mu i}^\beta (F_{\mu\nu}^\beta - \epsilon_i^\beta S_{\mu\nu}) = 0 \quad , \quad \mu = 1, 2, \dots, N \quad (2.13)$$

The energy obtained through UHF calculations will always be less than or equal to that calculated using the RHF method, due to the Variational Theorem. However, with UHF calculations, the wave function is no longer an eigenfunction of the total spin operator. As a result, it is possible to obtain errors due to the mixing of the states of high multiplicity, known as spin-contamination.¹⁴

2.9 Electron Correlation

One shortcoming of the HF method arises from the use of the Central Field Approximation, where the individual electrons move in a 'smeared field' of the other electrons. However, in reality, each electron's motion is influenced by the motions of the other electrons, which is referred to as electron correlation.² In the HF method, as the description of the wave function is improved, through the inclusion of more basis functions, the energy calculated converges to what is known as the Hartree-Fock Limit.¹⁴ The difference in energy between the energy calculated at the Hartree-Fock Limit (E_{HF}) and the exact ground-state energy (E_{real}) is the energy due to electron correlation (E_{corr}):

$$E_{corr} = E_{real} - E_{HF} \quad (2.14)$$

Due to the Variational Theorem, the Hartree-Fock energy will always be greater than that of the real system, thus the electron correlation energy is always negative.² One manner in which to improve the accuracy of the calculated energies is to recover this electron correlation energy. Two common approaches used to accomplish this are discussed below.

2.10 Configuration Interactions

In configuration interaction (CI) methods, the excitations of the electrons from the occupied orbitals (occ.) to the virtual orbitals (vir.) are added as determinants to the HF wave function:¹⁴

$$\Psi_{CI} = \Psi_{HF} + \sum_i \sum_r^{occ.vir.} a_i^r \Psi_i^r + \sum_{i < j} \sum_{r < s}^{occ.vir.} a_{ij}^{rs} \Psi_{ij}^{rs} + \dots \quad (2.15)$$

If all of the possible excitations are included this method is known as Full-CI. In theory, with the use of an infinite basis set, Full-CI can solve the electronic Schrödinger equation exactly.¹⁴ Another attractive feature of this method is that it is both variational, the predicted energy is always greater than or equal to the exact energy (see section 2.6), and size-consistent, the error in the energy increases in proportion to the size of the chemical system. However, consideration of all possible excitations is computationally expensive, and as a result, the Full-CI method is impractical for all but the smallest of systems. Alternatively, if only a limited number of configurations are included in the calculation, CI calculations become computationally feasible for larger systems. These methods are referred to as limited-CI methods and are characterized by the excitations that are included. For example, inclusion of only double excitations is CID and single and double excitations is CISD.¹⁴ Although the limited-CI methods are variational, they are not size-consistent.

2.11 Møller-Plesset Perturbation Theory

Møller-Plesset Theory improves the HF method by considering the effects of electron correlation as a perturbation.² As such, to the Hartree-Fock Hamiltonian, \hat{H}_0 , a perturbation, λV , is added to obtain the complete Hamiltonian, \hat{H} :

$$H = H_0 + \lambda V \quad (2.16)$$

The perturbation is then defined as the difference between the complete Hamiltonian and the Hartree-Fock Hamiltonian:

$$\lambda V = \lambda(H - H_0) \quad (2.17)$$

where λ is a dimensionless parameter.

From perturbation theory, the wave function (Ψ_λ) and energy (E_λ) of the system described by the complete Hamiltonian (\hat{H}_λ) may be expressed as a Taylor series:²

$$\Psi = \Psi_0^{(0)} + \lambda \Psi_0^{(1)} + \lambda^2 \Psi_0^{(2)} + \dots \quad (2.18)$$

$$E = E_0^{(0)} + \lambda E_0^{(1)} + \lambda^2 E_0^{(2)} + \dots \quad (2.19)$$

where

$$\Psi_0^{(n)} = \frac{1}{n!} \left. \frac{\partial^n \Psi_0}{\partial \lambda^n} \right|_{\lambda=0} \quad E_0^{(n)} = \frac{1}{n!} \left. \frac{\partial^n E_0}{\partial \lambda^n} \right|_{\lambda=0} \quad n = 1, 2, \dots \quad (2.20)$$

Møller-Plesset perturbation theory methods are referred to as MPn methods and are classified by the nth order, where the Taylor series is truncated. For example, MP1 calculations include only the first-order perturbation and its energy corresponds to that obtained by the Hartree-Fock method. Inclusion of the second-order perturbations, i.e., MP2, however, improves the Hartree-Fock method. Third- and Fourth-order perturbations methods, MP3 and MP4, are also available. These MPn methods are size-consistent, but not variational.

2.12 Density Functional Theory

An alternative to the wave function based methods is density functional theory (DFT). Instead of using the wave function to obtain the information of the system, DFT uses the electron density. This is advantageous for several reasons. Firstly, unlike the physically unobservable wave function, the electron density can be experimentally measured.¹⁵ In addition, electron correlation is inherently included in the electron density and when integrated over all space the density produces the total number of electrons of the system (N):

$$N = \int \rho(r) dr \quad (2.21)$$

Furthermore, the positions of the nuclei correspond to local maxima in the electron density. Therefore, the electron density can be a powerful tool, however, its implementation into a method was not realized until after the formulation of key theorems.

2.12.1 Hohenberg-Kohn Theorem

The Hohenberg-Kohn existence theorem states that the energy, wave function and other properties of a system can be obtained as a function of the ground-state electronic probability density of the system.¹⁶ It should be noted that a functional is a function of a function,² and in this case the density, ρ , is a function of the x, y, z coordinates of the nuclei, while the energy (E) is a function of ρ , indicated by $E[\rho]$. Thus, this offers a simplification relative to the wave function, which recall is a function of three spatial functions and one spin function for each electron. Regardless of the number of electrons, the electron density is a function of only three variables.² This theorem, however, only

proves that the density may be used to elucidate the information of the system. However, it does not provide a procedure to predict the density.

2.12.2 Kohn-Sham Theorem

Kohn and Sham, however, devised a method to solve Hohenberg-Kohn's problem. Firstly, they showed that the density, ρ , can be expressed as the sum of one-electron density orbitals, ψ_i^{KS} , known as Kohn-Sham orbitals:¹⁵

$$\rho = \sum_{i=1}^n |\psi_i^{KS}|^2 \quad (2.22)$$

These Kohn-Sham orbitals are obtained through a Self-Consistent procedure similar to that used by Hartree-Fock theory, and thus, DFT methods are, in principle, variational.

In addition, Kohn and Sham showed that the total energy (E_{exact}) can be divided into its component energies:¹⁷

$$E_{exact}[\rho] = E^T[\rho] + E^V[\rho] + E^J[\rho] + E^{XC}[\rho] \quad (2.23)$$

where E^T is the kinetic energy of the non-interacting electrons, E^V is the potential energy term for the nuclear-electron attraction and the nuclear-nuclear repulsions, E^J is the electron-electron repulsion term and E^{XC} is the exchange-correlation term. The kinetic energy and potential energy terms can be solved exactly; however, E^{XC} must be approximated as it cannot be determined explicitly.¹⁵ The E^{XC} term is commonly broken up into two components, the exchange energy term (E^X) and the correlation energy term (E^C):

$$E^{XC} = E^X + E^C \quad (2.24)$$

Various functionals have been developed to approximate the exchange and correlation terms and are used to classify the DFT methods.

The local-density approximation (LDA) functionals consider the electron density to be uniformly distributed at all positions. This allows for the exchange and correlation energies at any position to be computed directly from the density of that point.¹⁵ Common examples of LDA methods are the Slater exchange functional and the Vosko-Wilk-Nusair (VWN) correlation functional.

A drawback from the LDA methods is that the true electron density of molecular systems is not uniform. Therefore, functionals have been improved to account for not only the local density, but also how it changes, i.e., its gradient. Functionals of this type are collectively known as generalized-gradient approximations (GGA).¹⁵ Examples of GGA methods include Becke 88 (B) exchange functional and Lee-Yang-Parr (LYP) correlation functional.

2.12.3 The B3LYP Hybrid Functional

One of the most popular DFT methods is the B3LYP functional. This functional is a hybrid method, as it is obtained through the mixing of local density and gradient-corrected exchange with correlation functionals and includes some contribution from the Hartree-Fock method:¹⁸⁻²⁰

$$E_{xc}^{B3LYP} = (1-a)E_x^{LSDA} + aE_x^{HF} + b\Delta E_x^B + (1-c)E_c^{LSDA} + cE_c^{LYP} \quad (2.25)$$

The constants a , b , and c are used to modulate the contributions of exchange and correlation. These values have been optimized to reproduce experimental data (atomization energies, ionization energies, and proton affinities).¹⁵

2.14 Basis Sets

Basis sets are a set of mathematical functions, known as basis functions, that are used to describe the molecular and Kohn–Sham orbitals of the system under investigation. They are usually constructed by one of two types of basis functions: Slater-type orbitals (STOs) or Gaussian-type functions (GTFs).¹⁴ STOs accurately represent the atomic orbitals; however, they have a large computational cost associated with them. GTFs, on the other hand, are computationally cheaper, but less accurate. However, a linear combination of GTFs can be used to accurately reproduce STOs and still remain cheaper.¹⁴ Minimal basis sets are the simplest basis sets available, as they use only one basis function per orbital. However, this may provide a poor description of the orbitals and lead to inaccurate results. Thus, the quality of basis sets may be increasing the number of basis functions. These various schemes to accomplish this are described below.

2.14.1 Split-Valence Basis Sets

Split-valence basis sets use more basis functions to describe the valence orbitals, thus, resulting in greater flexibility in the radial size of the orbitals.²¹ This is achieved by using two or more basis functions to describe each valence orbital. For example, a Double-Zeta basis set uses two basis functions per valence orbital, e.g., 6-31G and cc-

pVDZ for Pople and Dunning basis sets, respectively, while a Triple-Zeta basis set would use three, e.g., 6-311G and cc-pVTZ.

2.14.2 Polarization Basis Sets

Polarization basis sets allow for the electron density of an atom to be displaced away from the nucleus, thus enabling orbitals to change shape.²¹ This is achieved by including additional unoccupied atomic basis functions of higher angular-momentum, i.e., polarization functions. For example, additional p -, d -, etc... basis functions are included for hydrogen atoms, while additional d -, f -, etc... basis functions are included on non-hydrogen atoms. In the case of Pople basis sets, the inclusion of diffuse functions must be indicated explicitly, e.g., 6-31G(d,p) puts d -functions on heavy atoms and p -functions on hydrogen atoms, whereas for Dunning basis sets they are included in the definition.

2.14.3 Diffuse Functions

Diffuse functions are spatially large atomic orbitals that allow the orbital to occupy a larger area of space.²¹ Within Pople basis sets, a single "+" sign denotes the inclusion of diffuse function on heavy atoms only, e.g., 6-31+G, whereas "++" signifies that they are included on both heavy atoms and hydrogens, e.g., 6-31++G. In the case of Dunning basis sets, the addition of diffuse functions is symbolized by the prefix "aug", e.g., aug-cc-pVDZ.

2.14.4 Pople Diagram

In theory, a Full-CI calculation with an infinitely sized basis set would provide an exact solution to the Schrödinger equation. However, such calculations are impossible as the basis set must be truncated at some point. In addition, a large computational cost, i.e. CPU time and the computer resources required, is associated with the use of high electron correlation methods and large basis sets. Thus, a compromise between the computational costs and chemical accuracy must be made. This relationship is illustrated in a Pople diagram (Figure 2.1).

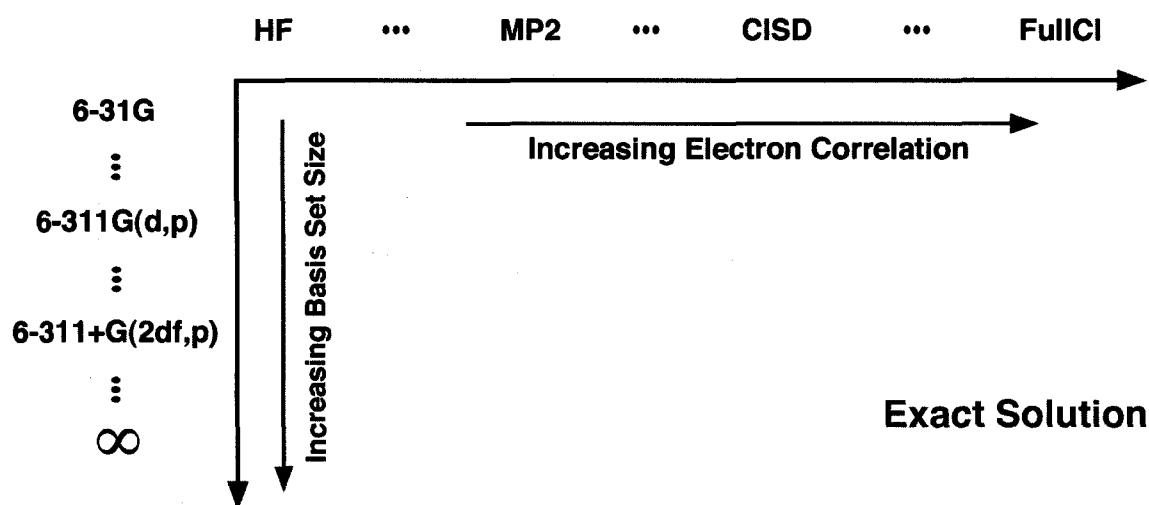


Figure 2.1. Illustration of a Pople Diagram.

2.14.5 Compound Methods

Low level of theory calculations with moderate sized basis sets are often found to predict reliable geometries of chemical systems. However, for accurate energies, higher levels of theory and larger basis sets are required. Therefore, a common approach is to determine the geometry of a system at a lower level of theory and use it as the input for a single-point energy calculation. In order to be valid, however, it is assumed that the

difference in the geometry obtained at the lower level of theory to that of the higher level of theory is negligible. A single-point calculation is an example of a compound method.

The general basis set notation used to indicate the level of theory of a calculation is:

$$\text{Method 1 / Basis Set 1 // Method 2 / Basis Set 2} \quad (2.26)$$

where a single-point energy calculation was performed at the Method 1 and Basis Set 1 level of theory using the geometry optimized at the Method 2 and Basis Set 2 level of theory. For example, the notation:

$$\text{B3LYP/6-311+G(2df,p)//B3LYP/6-31G(d)} \quad (2.27)$$

indicates that a single point energy calculation was performed using the B3LYP method in combination with the 6-311+G(2df,p) basis set using the geometry optimized at the B3LYP method with the 6-31G(d) basis set.

2.15 Basis Set Superposition Error

The interaction energy of a non-covalent bimolecular complex (AB) may be determined by taking the difference between the complex energy ($E(\text{AB})$) and the energy of the isolated monomers ($E(\text{A})$ and $E(\text{B})$) as seen below:¹⁴

$$\Delta E_{\text{bind}} = E^{\text{ab}}(\text{AB}) - [E^{\text{a}}(\text{A}) + E^{\text{b}}(\text{B})] \quad (2.28)$$

where the superscripts a and b refer to the basis functions of molecules A and B, respectively. Note, that if a large, yet incomplete basis set is employed, the complex AB has more basis functions available to it than the monomers. This enhances the flexibility of the basis set of the complex as one monomer may borrow basis functions from the

other. This results in an improvement of its wave function, thereby, lowering the energy of the complex and overestimating the resulting interaction energy. This phenomenon is known as the basis set superposition error (BSSE).¹⁴

Boys and Bernardi proposed a counterpoise method to correct for BSSE.²² In their method, a counterpoise correction (CP), which takes into account the stabilization provided by the additional basis functions in the complex, is subtracted from the interaction energy to obtain a CP corrected energy:

$$\Delta E_{\text{bind}}^{\text{CP}} = E^{\text{ab}}(\text{AB}) - [E^{\text{a}}(\text{A}) + E^{\text{b}}(\text{B})] - \text{CP} \quad (2.29)$$

This CP correction is determined as follows:

$$\text{CP} = [E^{\text{ab}}(\text{A})_{\text{AB}} - E^{\text{a}}(\text{A})_{\text{AB}}] + [E^{\text{ab}}(\text{B})_{\text{AB}} - E^{\text{b}}(\text{B})_{\text{AB}}] \quad (2.30)$$

where the subscript AB denotes the energy of the molecule (A or B), which was optimized using its geometry from the AB complex. In equation 2.30, $E^{\text{ab}}(\text{A})_{\text{AB}}$ is the energy of monomer A in its geometry in the complex with the basis functions of monomer B present, but not the B monomer itself.

2.16 Calculations

The geometry of the structures under investigation must be optimized in order to provide any valid information relating to the chemical system. A structure's geometry is optimized when the first derivative of the energy with respect to position of the nuclei, i.e., the gradient, is zero. At this point, the nuclei are oriented in such a manner that there are no forces acting on them. The ultimate goal of optimizations is to obtain the lowest energy structure. In order to find this minimum, the optimization procedure must first determine the energy and gradient of the energy of the inputted geometry. The gradient

of the energy is then evaluated to determine which direction along the potential energy surface the system should follow, e.g., the path with the greatest decrease in energy. The optimization will follow along the potential energy surface until it can no longer lower the energy. Such a point is referred to as a minima and corresponds to the equilibrium geometry. Since the optimization follows the potential energy surface of the system based on the inputted geometry, it is necessary to choose the initial geometry of the system carefully. In addition, the level of theory used for the optimization has an effect on the predicted geometry, as more accurate geometries are obtained using higher levels of theory. However, as mentioned previously, there is an elevated computational cost associated with these higher levels of theories. Optimized minima have all real, positive frequencies, and are seen as "wells" on potential energy surfaces (see Figure 2.2). Another type of optimization involves the location of transition structures. Optimized transition structures have only one imaginary frequency that corresponds to the transitional motion linking the two minima. Frequency calculations provide the vibrational data required for characterizing stationary points. In addition, they determine the zero-point vibrational energy (ZPVE) correction. The ZPVE correction arises due to the Born-Oppenheimer approximation, where the nuclei are assumed to be stationary, however, even at zero Kelvin, they exhibit some vibrational motion.¹⁴ Therefore, adding the ZPVE correction to the calculated energy may allow for a more accurate energy of the system to be obtained.

2.17 Potential Energy Surfaces

Due to the approximations used to define the electronic Hamiltonian, the energy of the system is dependent upon the coordinates of the nuclei (see equation 2.4).² A

potential energy surface (PES) illustrates the energy of the system corresponding to the location of its nuclei, as shown in Figure 2.2.

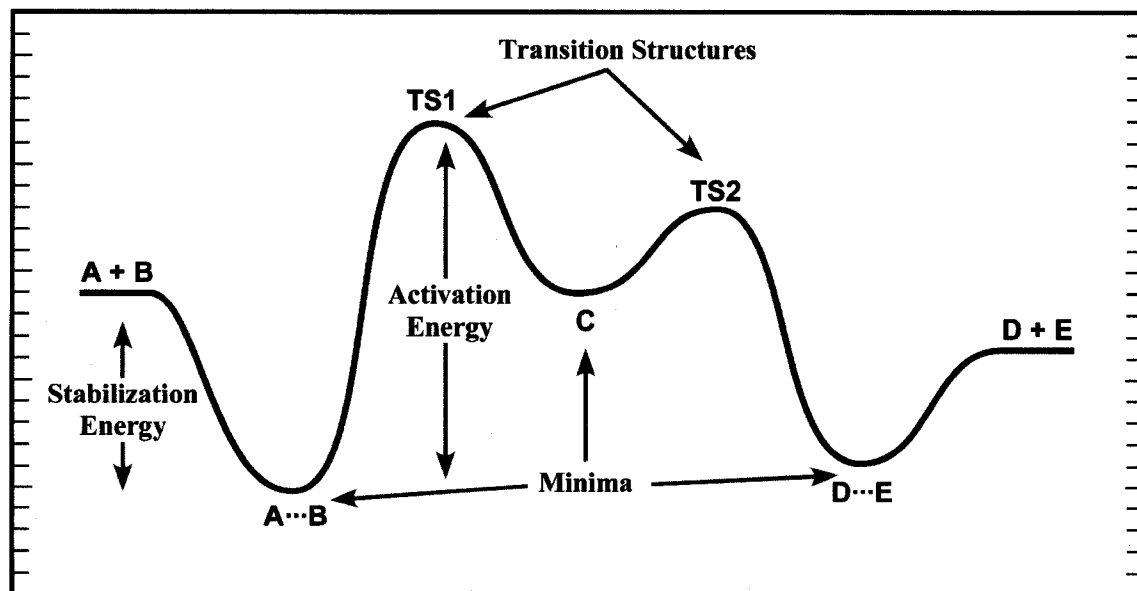


Figure 2.2. Illustration indicating key features of a potential energy surface for the reaction of A and B to produce C and D.

To completely evaluate a PES, the energy of the system must be calculated at all locations of the nuclei; however, this is not feasible due to the extreme computational cost associated with it. Thus, usually only the optimized stationary points corresponding to minima, e.g., equilibrium structures, and first-order saddle points, e.g., transition structures, are shown as they are usually the most mechanistically important points.

2.18 Solvation

Calculations are by default carried out in the gas-phase (dielectric constant of 1); however, this may not accurately represent natural conditions, as chemical reactions often occur in the presence of solvent, which have a dielectric constant greater than 1. Thus, in some chemical systems, the inclusion of solvation effects may be important. In general, there are two approaches for modeling the inclusion of solvent. In the first

method explicit solvent molecules can be added to the system. However, this can become complicated due to the multitude of possible arrangements they may assume and it is also computationally demanding. An alternative approach is to add the solvent implicitly via a continuum of dielectric constant. This approach is more computationally practical and two solvation methods are briefly discussed below.

Two solvation methods are used throughout this thesis: the Integral Equation Formalism (IEF) method²³⁻²⁵ and the Poisson-Boltzmann (PB) method.^{26,27} Although they differ slightly in the manner by which they calculate the effects of the polarization of the solute by the solvent, both of these methods employ the Polarized Continuum method (PCM). Both the IEF- and PB-PCM methods employ Tomasi's PCM method, where the contour of the solvent accessible contour is constructed by a series of interlocking spheres centered on the atoms as illustrated, in Figure 2.3.²¹ The van der Waals radius of the atom on which the sphere is centered determines the size of the sphere.

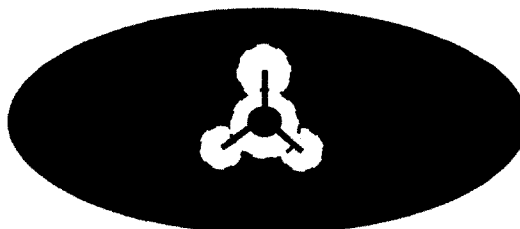


Figure 2.3. Diagram of the cavity created for the solute in Tomasi's PCM solvation model.

2.18 Technical Aspects and Units

For this investigation, all the calculations were performed using the Gaussian 03²⁸ and Jaguar 5.5²⁹ suites of programs.

The relative energies reported in this thesis are in kilojoules per moles (kJ mol^{-1}) or kilocalories per mole (kcal mol^{-1}), obtained using the following conversion factors from hartrees (h):

$$1 \text{ h} = 2625.5 \text{ kJ mol}^{-1}$$

$$1 \text{ h} = 627.5 \text{ kcal mol}^{-1}$$

References

- (1) Schrödinger, E. *Phys. Rev.* **1926**, *28*, 1049.
- (2) Levine, I. N. *Quantum Chemistry*, 4th ed.; Prentice-Hall, Inc.: New Jersey, 1991.
- (3) Born, M.; Oppenheimer, J. R. *Physik* **1927**, *84*, 457.
- (4) Hartree, D. R. *Proc. Cam. Phil. Soc.* **1928**, *24*, 89.
- (5) Hartree, D. R. *Proc. Cam. Phil. Soc.* **1928**, *24*, 111.
- (6) Hartree, D. R. *Proc. Cam. Phil. Soc.* **1928**, *24*, 246.
- (7) Slater, J. C. *Phys. Rev.* **1929**, *34*, 1293.
- (8) Slater, J. C. *Phys. Rev.* **1930**, *35*, 509.
- (9) Roothaan, C. C. J. *Rev. Mod. Phys.* **1951**, *23*.
- (10) Hall, G. G. *Proc. Roy. Soc. London* **1951**, *205*, 541.
- (11) Fock, V. Z. *Phys.* **1930**, *61*, 126.
- (12) Young, D. *Computational Chemistry: A Practical Guide for Applying Techniques to Real World Problems*; John Wiley and Sons, Inc.: New York, 2001.
- (13) Pople, J. A.; Nesbet, R. K. *J. Chem. Phys.* **1954**, *22*, 571.
- (14) Cramer, C. J. *Essentials of Computational Chemistry*; Wiley and Sons, Inc.: New York, 2002.
- (15) Koch, W.; Holthausen, M. C. *A Chemist's Guide to Density Functional Theory*, 2nd ed.; Wiley-VCH: Toronto, 2001.
- (16) Hohenburg, P.; Kohn, W. *Phys. Rev.* **1965**, *136*, 864.
- (17) Kohn, W.; Sham, L. J. *Phys. Rev. A* **1965**, *140*, 1133.

- (18) Becke, A. D. *J. Chem. Phys.* **1993**, *98*, 1372.
- (19) Lee, C.; Yang, W.; Parr, R. G. *Phys. Rev. B* **1988**, *37*, 785.
- (20) Stephens, P. J.; Devlin, F. J.; Chabalowski, C. F.; Frisch, M. J. *J. Phys. Chem.* **1994**, *98*, 11623.
- (21) Foresman, J. B.; Friesch, Æ. *Exploring Chemistry with Electronic Structure Methods*, 2nd ed.; Gaussian Inc.: Pittsburg, 1996.
- (22) Boys, S. F.; Bernardi, F. *Mol. Phys.* **1970**, *19*, 553.
- (23) Cancès, E.; Mennucci, B.; Tomasi, J. *J. Chem. Phys.* **1997**, *107*, 3032.
- (24) Mennucci, B.; Cancès, E.; Tomasi, J. *J. Phys. Chem.* **1997**, *101*, 10506.
- (25) Mennucci, B.; Tomasi, J. *J. Chem. Phys.* **1997**, *106*, 5151.
- (26) Tannor, D. J.; Marten, B.; Murphy, R.; Friesner, R. A.; Sitkoff, D.; Nicholls, A.; Ringnalda, M. N.; Goddard, W. A.; Honig, B. *J. Am. Chem. Soc.* **1994**, *116*, 11875.
- (27) Marten, B.; Kim, K.; Cortis, C.; Friesner, R. A.; Murphy, R. B.; Ringnalda, M. N.; Sitkoff, D.; Honig, B. *J. Phys. Chem.* **1996**, *100*, 11775.
- (28) Frisch, M. J.; Trucks, G. W.; Schlegel, H. B.; Scuseria, G. E.; Robb, M. A.; Cheeseman, J. R.; Montgomery, J. A. J.; Vreven, T.; Kudin, K. N.; Burant, J. C.; Millam, J. M.; Iyengar, S. S.; Tomasi, J.; Barone, V.; Mennucci, B.; Cossi, M.; Scalmani, G.; Rega, N.; Petersson, G. A.; Nakatsuji, H.; Hada, M.; Ehara, M.; Toyota, K.; Fukuda, R.; Hasegawa, J.; Ishida, M.; Nakajima, T.; Honda, Y.; Kitao, O.; Nakai, H.; Klene, M.; Li, X.; Knox, J. E.; Hratchian, H. P.; Cross, J. B.; Adamo, C.; Jaramillo, J.; Gomperts, R.; Stratmann, R. E.; Yazyev, O.; Austin, A. J.; Cammi, R.; Pomelli, C.; Ochterski, J.; Ayala, P. Y.; Morokuma, K.; Voth, G. A.; Salvador, P.; Dannenberg, J. J.; Zakrzewski, V. G.; Dapprich, S.; Daniels, A. D.; Strain, M. C.; Farkas, O.; Malick, D. K.; Rabuck, A. D.; Raghavachari, K.; Foresman, J. B.; Ortiz, J. V.; Cui, Q.; Baboul, A. G.; Clifford, S.; Cioslowski, J.; Stefanov, B. B.; Liu, G.; Liashenko, A.; Piskorz, P.; Komaromi, I.; Martin, R. L.; Fox, D. J.; Keith, T. A.; Al-Laham, M. A.; Peng, C. Y.;

Nanayakkara, A.; Challacombe, M.; Gill, P. M. W.; Johnson, B. G.; Chen, W.; Wong, M. W.; Gonzalez, C.; Pople, J. A. Gaussian 03; Gaussian Inc.: Wallingford CT, 2004.

(29) Schrödinger, L. L. C. In *Jaguar 5.5* Portland, OR, 1991-2003.

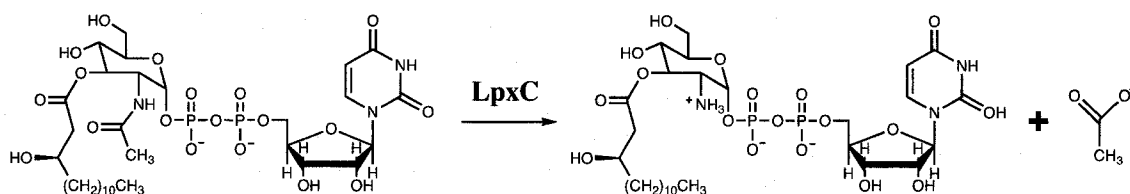
Chapter 3

A DFT Investigation on the Mechanism of the Deacetylation Reaction Catalyzed by LpxC

3.1 Introduction

UDP-3-*O*-(*R*-3-hydroxymyristoyl)-*N*-acetylglucosamine deacetylase (LpxC) has attracted increasing attention in recent years as an antibacterial target.¹⁻⁸ This is due in large part to the fact that it catalyzes the first *committed* step in the production of Lipid A,⁹ which anchors the lipopolysaccharides that form the outer membrane of gram-negative bacteria to the cell wall.¹⁰ Furthermore, Lipid A is responsible for the pathogenesis of gram-negative bacteria and is involved in antibiotic resistance.⁴ Thus, information on the catalytic mechanism of LpxC may provide insights for creating more effective antibiotics against gram-negative bacteria.

Scheme 3.1. LpxC catalyses the conversion of UDP-3-*O*-(*R*-3-hydroxymyristoyl)-*N*-acetylglucosamine to UDP-3-*O*-(*R*-3-hydroxymyristoyl)glucosamine and acetate.¹⁰



More specifically, LpxC catalyzes the second step in the biosynthesis of Lipid A, deacetylation of UDP-3-*O*-(*R*-3-hydroxymyristoyl)-*N*-acetylglucosamine to give UDP-3-*O*-(*R*-3-hydroxymyristoyl)glucosamine and acetate (Scheme 3.1).¹⁰ LpxC is a metalloenzyme that has been found to employ a zinc (II) metal ion in its active site.¹¹

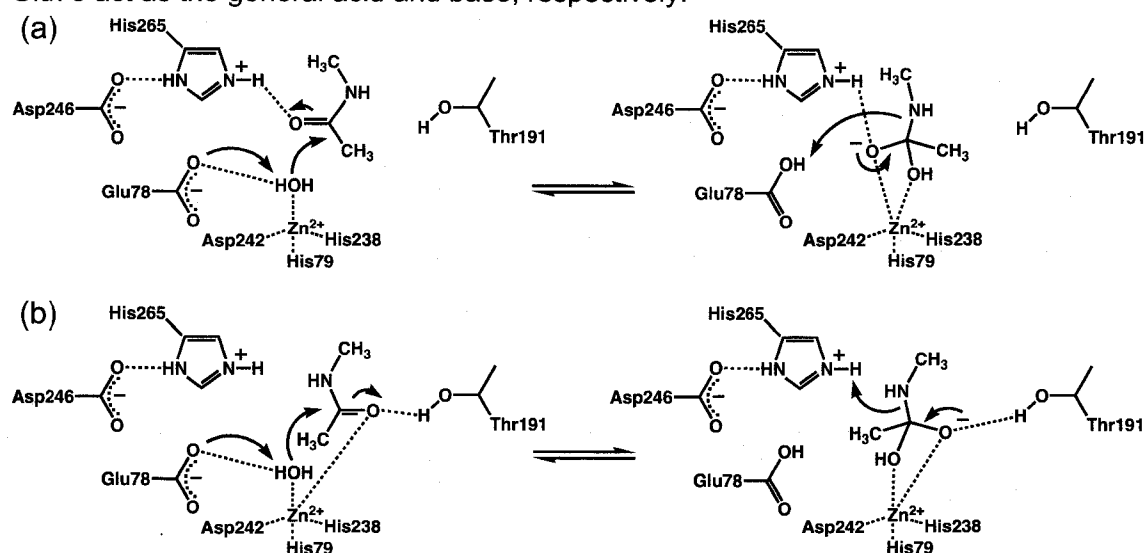
Through mutagenesis,¹² EXAFS studies¹³ and X-ray crystallographic efforts,¹⁴ it is now known that the Zn^{2+} ion directly coordinates to three amino acid residues: two histidines (His79 and His242) and an aspartate (Asp238). The fourth ligand is a water molecule, a typical key component of zinc hydrolases.^{15,16} Recently, Gennadios *et al.*¹⁷ examined the available crystal structures of LpxC and observed that the active site Zn^{2+} ion exhibits both square pyramidal and tetrahedral geometries, owing to the flexibility of its coordination sphere. Interestingly, from the structure of the LpxC–imidazole complex, which is believed to show the Zn^{2+} in its native state, the Zn^{2+} ion is square pyramidal with two water molecules coordinated. Therefore, it was proposed that binding of the substrate displaces one of these water molecules in order to accommodate a substrate···Zn interaction, while the second water molecule is retained.¹⁷ This suggested coordination geometry for the substrate was further supported by the X-ray crystal structure of LpxC co-crystallized with the substrate analogue TU-514.¹⁷

The catalytic mechanism of LpxC is generally accepted to proceed via a general acid/base mechanism, common to many Zn^{2+} -dependent enzymes.^{16,18} Specifically, a general base deprotonates the Zn^{2+} -bound H_2O . The resulting hydroxyl then nucleophilically attacks the substrate's carbonyl carbon to form a tetrahedral (*gem*-diolate) intermediate. The subsequent intermediate then accepts a proton at its amino nitrogen from a general acid, cleaving the amide bond and forming the desired products. Although, the general mechanism is agreed upon, the exact nature of the general acid and base are unclear. Initially, Whittington *et al.*¹⁴ proposed a mechanism (Scheme 3.2) in which the active site glutamate (Glu78) acts as the general base. Furthermore, they also proposed that once protonated Glu78– H^+ acts as the general acid as they deemed it to be better positioned to do so than a protonated active site histidine (His265– H^+). Instead, His265– H^+ was proposed to simply help stabilize the transition state.¹⁴ Shortly thereafter, however, based on the structure of LpxC complexed with TU-514 and

mutagenesis studies, Coggins *et al.*¹⁹ proposed that the His265 residue is in fact more appropriately suited to serve as *both* the general acid and base in the mechanism, with the Glu78 serving only a secondary role in the catalytic mechanism. However, in a more recent study by Coggins *et al.*²⁰ the pK_a of His265 was determined to be 7.6, suggesting that it is most likely protonated within the LpxC active site and thus unable to accept a proton from the Zn²⁺-bound water molecule. Recently, based on kinetic studies of wild type and mutant enzymes both McClerren *et al.*²¹ and Hernick *et al.*²² proposed that Glu78 acts as the general base in the mechanism. This proposal is further supported by the structural features observed in the LpxC-cacodylate and LpxC-palmitate complexes obtained by Hernick *et al.*²² However, these structures also suggest that His265-H⁺ might in fact be more suitably positioned than Glu78-H⁺ to protonate the amino nitrogen of the intermediate. Based on these findings, they proposed a mechanism in which His265-H⁺ and Glu78 work together as a general acid/base pair (Scheme 3.2).²² In particular, they proposed that Glu78 accepts a proton from the Zn²⁺-bound H₂O, while His265-H⁺ protonates the intermediate's nitrogen, thus cleaving the amide bond.

In this chapter we have used density functional theory in order to investigate the roles of the active site amino acids as well as to elucidate the overall catalytic mechanism of LpxC.

Scheme 3.2. Proposed mechanisms for the deacetylation reaction catalyzed by LpxC in which: (a) Glu78 acts as both the general acid and base^{14,22} and (b) His265-H⁺ and Glu78 act as the general acid and base, respectively.²²

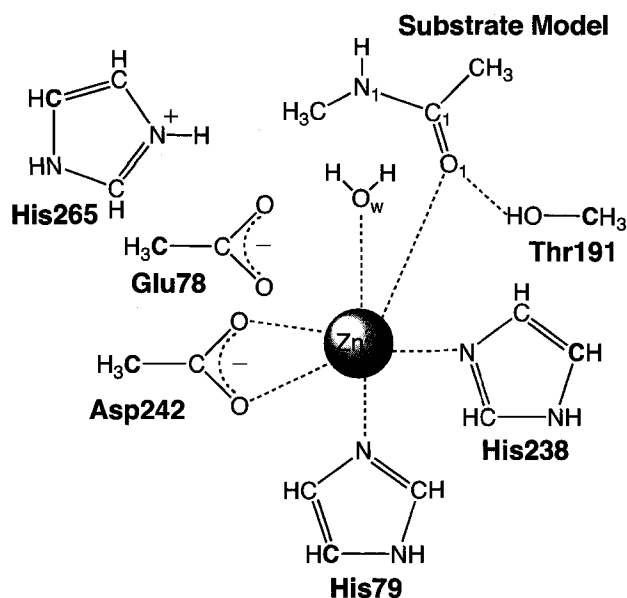


3.2 Computational Methods

All calculations were performed using the density functional theory (DFT) method B3LYP, a combination of Becke's three-parameter hybrid exchange functional²³ with the Lee-Yang-Parr correlation functional²⁴ as implemented in Jaguar 5.5.²⁵ The LACVP** basis set was employed for all optimizations. Effects due to the polar environment around the active site were modelled using the Poisson-Boltzmann polarizable continuum method (PB-PCM) as implemented in Jaguar (i.e., PB-PCM-B3LYP/LACVP**).²⁵ A dielectric constant of 4.0 was chosen as it has been previously suggested for modeling the environment of proteins.^{26,27} All structures were characterized as minima or transition structures via gas-phase frequency calculations in Gaussian 03.²⁸ Relative energies were obtained by performing single-point calculations at the B3LYP/LACV3P+** level of theory in combination with the PB-PCM solvation method ($\epsilon=4.0$) using the above optimized structures (i.e., PB-PCM-B3LYP/LACV3P+**//PB-PCM-B3LYP/LACVP**).

The chemical model employed in this chapter (Scheme 3.3) was obtained from the LpxC–cacodylate crystal structure (PDB: 1YHC).²² In our system, the substrate UDP-3-*O*-(*R*-3-hydroxymyristoyl)-*N*-acetylglucosamine was modeled by *N*-methylacetamide. In addition, we have included the Zn²⁺ ion as well as its coordinated ligands (His79, His238, Asp242 and water). We have also incorporated additional amino acid residues that have been proposed to be catalytically important, namely Glu78 and His265–H⁺ and Thr191. These residues are modeled as follows: histidines (His) as imidazoles, glutamate (Glu) and aspartate (Asp) as acetate, and threonine (Thr) as methanol. Furthermore, each of these model amino acids have had their terminal carbon atom fixed at the crystal structure position, in order to maintain the integrity of the active site (fixed atoms are shown in red bold print in Scheme 3.3).

Scheme 3.3. Schematic illustration of the LpxC active site model used in this chapter. Atoms held fixed throughout optimizations are bolded and coloured red.



3.3 Results and Discussion

3.3.1 The Water-Assisted Deacetylation Mechanism

In order to be able to provide greater insights into the enzyme catalyzed deacetylation mechanism, we first investigated the water-assisted hydrolysis of the amide bond in *N*-methylacetamide, our substrate model, via both concerted (red dashed) and step-wise (blue solid) mechanisms. The resulting potential energy surfaces (PESs) are given in Figure 3.1. It should be noted that these and related reactions have also been previously studied elsewhere.²⁹⁻³⁶

In the water-assisted hydrolysis of the amide bond in *N*-methylacetamide, the initial reactant complex (**1_{aq}**) lies 29.2 kJ mol⁻¹ lower in energy than the isolated reactants as a result of the hydrogen bond chain formed by the waters to the carbonyl oxygen of the methylacetamide.

The concerted mechanism then proceeds via the transition structure **TSC_{aq}** in which the oxygen (**O_w**) of one of the waters attacks at the carbonyl carbon centre (**C₁**) of the substrate. Simultaneously, however, the second water acts as a base and an acid by accepting a proton from the first attacking H₂O while concomitantly donating one of its own to the amide nitrogen (**N₁**), cleaving the amide bond (see Figure 3.1). In **TSC_{aq}**, the **C₁—N₁** bond has lengthened markedly by 0.196 Å to 1.544 Å relative to that observed in **1_{aq}**. Notably, the barrier for this mechanism is quite high at 175.4 kJ mol⁻¹ relative to **1_{aq}**, while the resulting hydrogen bonded product complex **3_{aq}** lies 11.9 kJ mol⁻¹ higher in energy than **1_{aq}**.

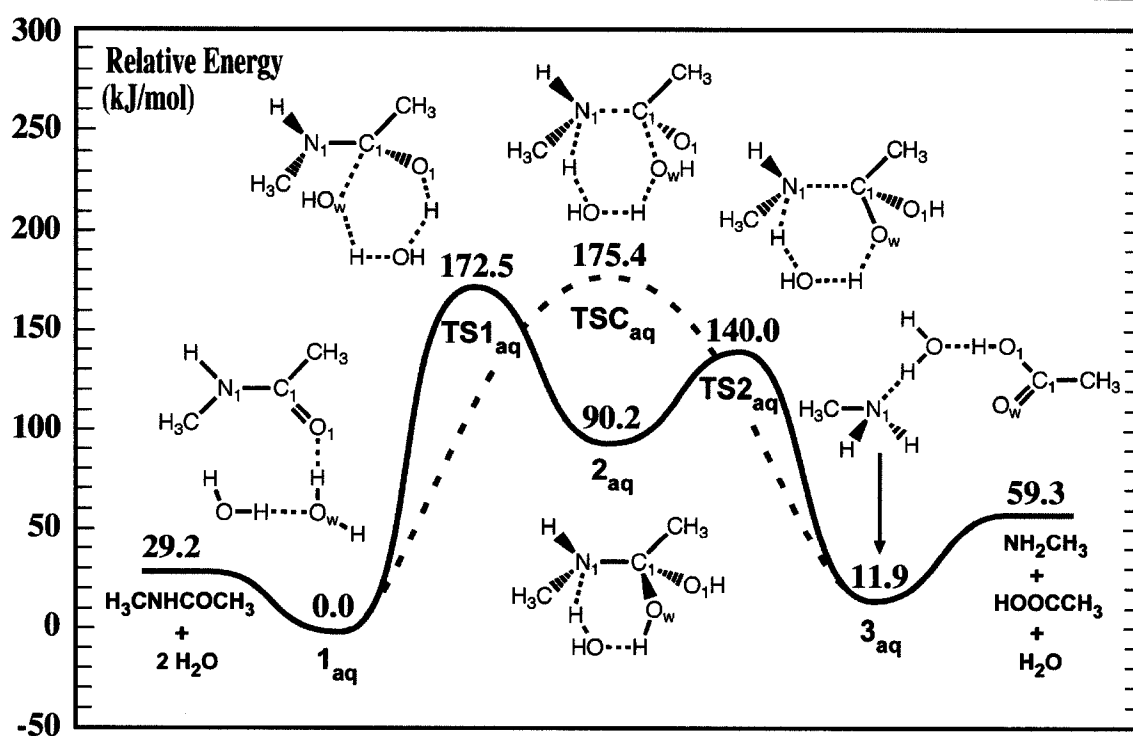


Figure 3.1. Potential energy surfaces for water-assisted hydrolysis of the amide bond of *N*-methylacetamide via concerted (red dashed) and step-wise (blue solid) mechanisms.

The step-wise mechanism cleaves the amide bond via a two-step process. In the first step, one water again attacks the substrate's carbonyl carbon centre while the 'assisting' water once again accepts one of its protons. However, now the 'assisting' H_2O donates one of its own protons to the substrate's carbonyl oxygen (O_1) thus forming the *gem*-diol intermediate 2_{aq} . This reaction step proceeds via TS1_{aq} at a cost of $172.5 \text{ kJ mol}^{-1}$, slightly lower than the barrier for the concerted mechanism. In contrast to TSC_{aq} , in TS1_{aq} the $\text{C}_1\text{—N}_1$ bond has elongated by only 0.025 \AA to 1.373 \AA , while the carbonyl $\text{C}_1=\text{O}_1$ distance has increased from 1.246 \AA to 1.312 \AA . The resulting 2_{aq} intermediate lies 90.2 kJ mol^{-1} higher in energy than the initial reactant complex 1_{aq} . Notably, the remaining H_2O in 2_{aq} is hydrogen bonded to both hydroxyl groups (2.077 \AA and 1.998 \AA to O_1 and O_w , respectively) and to the amide nitrogen (1.858 \AA). The $\text{C}_1\text{—N}_1$ bond in 2_{aq} resembles a typical C—N single bond with a length of 1.485 \AA , while both $\text{C}_1\text{—O}$

bonds resemble typical C—O single bonds with lengths of 1.407 and 1.406 Å. The second step involves the transfer of a proton from a C—OH group to the amine nitrogen. This reaction proceeds via **TS2_{aq}** at a cost of 49.8 kJ mol⁻¹ relative to **2_{aq}** or 140.0 kJ mol⁻¹ relative to **1_{aq}**. In **TS2_{aq}**, the remaining H₂O moiety abstracts a proton from a C—OH group while simultaneously donating one of its own to the amino nitrogen. It is noted that the breaking C₁—N₁ bond in **TS2_{aq}** is significantly longer (1.615 Å) than observed for **TSC_{aq}** of the concerted mechanism. Thus, overall the step-wise mechanism occurs with a slightly lower energy barrier than the concerted mechanism, the rate-determining step being the initial hydroxylation of the substrate at its C₁ center.

3.3.2 The Active Site–Bound Substrate Complex

We began our investigation of the actual LpxC catalyzed deacetylation mechanism by considering substrate binding within the active site. As noted above, we have used *N*-methylacetamide to model the UDP-3-*O*-(*R*-3-hydroxymyristoyl)-*N*-acetylglucosamine substrate. In the actual enzyme, the substrate's uridine 5'-diphosphate interacts with a region of basic amino acids,³⁷ while its 3-*O*-(*R*-3-hydroxymyristoyl) moiety is believed to interact with a hydrophobic region.¹⁴ Thus, the terminal methyl group of *our* model substrate should be directed towards this region in the active site model. In addition, upon binding to the active site, the substrate is believed to displace one of the two water molecules bound to the pentacoordinated Zn²⁺.¹⁷ Taking into account these considerations, there appears to be two potential orientations of the substrate within the active site. We have considered both possibilities with the lowest energy structures of each being shown in Figure 3.2.

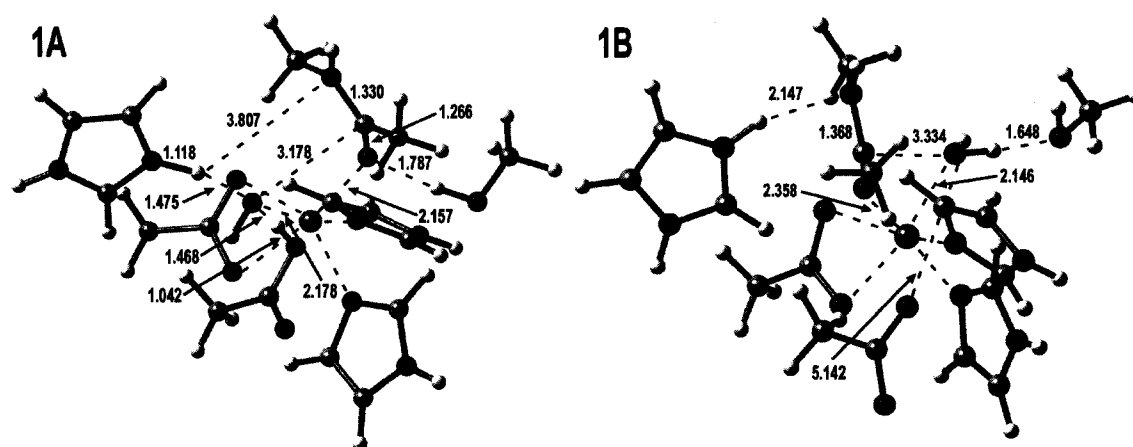


Figure 3.2. Lowest energy active site-bound substrate complexes: (1A) substrate bound between a Zn^{2+} -bound H_2O and Thr191 residue, (1B) substrate bound between His265- H^+ and a Zn^{2+} bound H_2O . Select optimized distances (Å) are also shown. [Zn (purple); C (gray); N (blue); O (red); H (white)].

In the first orientation, **1A**, the substrate binds between the zinc-bound $\text{H}_2\text{O}/\text{OH}^-$ moiety and the threonine residue. In the alternative orientation, **1B**, the substrate binds on the side of the Zn^{2+} -coordinated $\text{H}_2\text{O}/\text{OH}^-$ near the histidine. The lower energy structure is found to correspond to **1A** with the substrate bound via its carbonyl oxygen (O_1) to the Zn^{2+} ion at a distance of 2.157 Å. In addition, O_1 also forms a strong hydrogen bond with the hydroxyl group of the nearby Thr191 residue (1.787 Å). Interestingly, upon optimization of **1A** the H_2O also bound to the Zn^{2+} gave up its proton to Glu78. Thus, the initial substrate complex in fact contains a protonated Glu78 (Glu78- H^+) and a $\text{Zn}^{2+}\cdots\text{OH}^-$ moiety. The oxygen of the resulting hydroxide ion (O_w) interacts with the Zn^{2+} at a distance of 2.178 Å and also forms strong hydrogen-bond interactions with both Glu78- H^+ , through its previously donated proton, and His265- H^+ at distances of 1.468 and 1.475 Å, respectively. The distance between O_w of the hydroxide ion and the carbonyl carbon (C_1) of the substrate is 3.178 Å. In the higher energy structure **1B** the substrate coordinates to the Zn^{2+} ion through its carbonyl oxygen at a distance of 2.358 Å. The Zn^{2+} -bound H_2O is 2.146 Å away from the metal ion and

also forms a strong hydrogen bond to the oxygen of Thr191 (1.648 Å). However, unlike **1A**, in **1B** the Zn^{2+} -bound H_2O is not readily deprotonated by the glutamate residue, which is now in fact 5.142 Å away. Structure **1B** is significantly higher in energy than **1A** by 89.7 kJ mol^{-1} . If we consider the alternative **1B** structure in which the Zn^{2+} - OH_2 moiety has transferred a proton to the Glu78 residue, the resulting structure still lies more than 30 kJ mol^{-1} higher in energy than **1A**. Thus, **1A** was considered the most appropriate substrate bound active site model for further study.

3.3.3 The LpxC Catalyzed Deacetylation Reaction

The catalytic mechanism of LpxC was then investigated. The potential energy surface obtained for the overall mechanism is given in Figure 3.3.

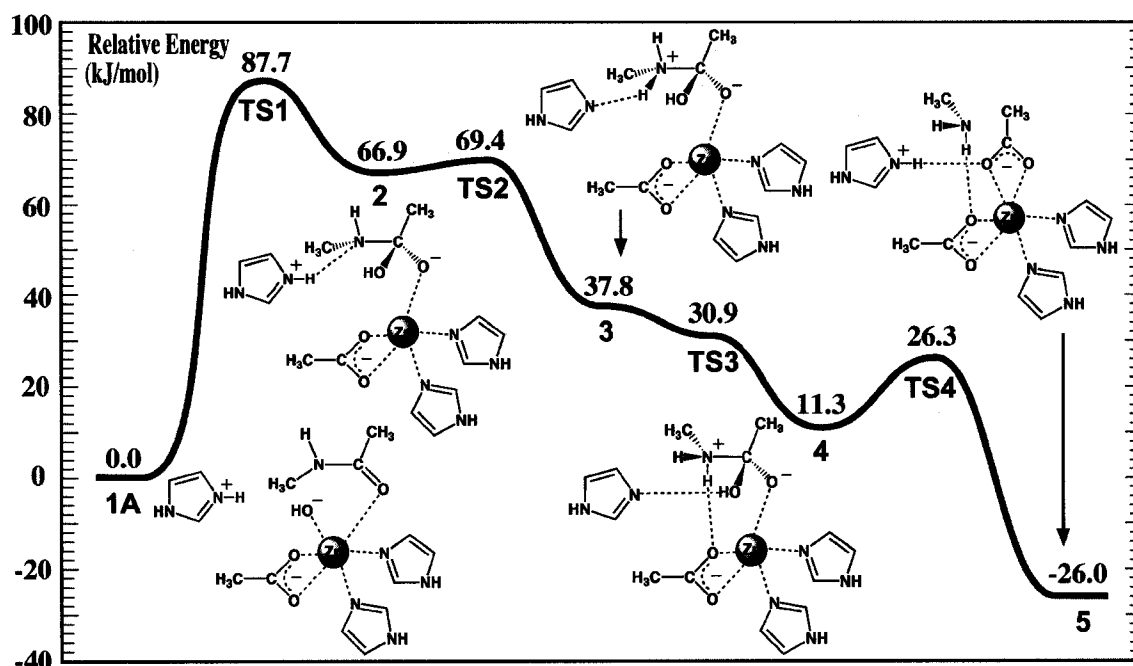


Figure 3.3. Potential energy surface for the overall reaction mechanism of LpxC. Key residues of minima are schematically shown in order to highlight changes in the system during the reaction. For clarity, the Thr191 and Glu78- H^+ residues have been omitted.

Analogous to the water assisted mechanism, the first step is found to be nucleophilic attack of the oxygen of the Zn^{2+} -bound hydroxyl group at the substrate's carbonyl carbon C_1 to form the *gem*-diolate intermediate (**2**). This step proceeds via **TS1** with a barrier of 87.7 kJ mol^{-1} , with **2** now lying just 66.9 kJ mol^{-1} higher in energy than the initial reactant complex **1A**. This barrier is only about half of that observed for the water-assisted mechanism (cf. Figure 3.1). This much lower barrier is likely indicative of the greater nucleophilicity of the OH^- oxygen relative to that of H_2O , as well as stabilization of the resulting *gem*-diolate intermediate by the active site. We note that the $\text{O}_w \cdots \text{C}_1$ distance in **TS1** (1.619 \AA) is significantly shorter than observed for **TS1_{aq}** (1.954 \AA) suggesting that the transition structure occurs later in the reaction, more closely resembling the intermediate in accordance with Hammond's postulate.³⁸ It also possibly reflects, in part, structural constraints due to the active site.

In **2**, the $\text{C}_1\text{—N}_1$ bond has also lengthened significantly by 0.194 \AA to 1.524 \AA and indeed is now slightly longer than observed in the solution-phase ($\epsilon=4.0$) optimized structure of the *gem*-diolate (1.505 \AA , not shown). In addition, the newly formed $\text{C}_1\text{—O}_w$ bond resembles a typical C—O single bond with a length of 1.478 \AA , while the $\text{C}_1\text{—O}_1$ bond has elongated from 1.266 \AA in **1A** to 1.332 \AA , suggesting that O_1 retains marked oxyanion character. Furthermore, as the substrate's carbonyl oxygen has formally become an oxyanion, its interaction with the metal ion has strengthened, as the $\text{O}_1 \cdots \text{Zn}^{2+}$ distance has shortened from 2.157 \AA to 1.973 \AA . However, as indicated by the $\text{O}_w \cdots \text{Zn}^{2+}$ distance of 3.191 \AA , the hydroxyl group transferred from the Zn^{2+} moiety to the substrate is no longer coordinated to the metal ion. This also illustrates the flexibility of the coordination sphere of Zn^{2+} . It should also be noted that the Zn^{2+} coordination environment of **2** is similar to that observed in the cacodylate-LpxC crystal structure: the oxyanion and not the hydroxyl group of the substrate is coordinated to the Zn .²² Other changes in active site interactions upon hydroxylation of the substrate are

also apparent. Upon transfer, the interaction between the $-O_wH$ oxygen and Glu78- H^+ 's proton has lengthened from 1.468 Å to 1.727 Å. Notably, His265- H^+ is now orientated such that its acidic proton forms a strong hydrogen bond with the nitrogen center of intermediate **2** (1.622 Å). In addition, the hydrogen bond between Thr191 and O_1 of the intermediate is markedly longer by 0.324 Å at 2.111 Å than that observed in **1A**.

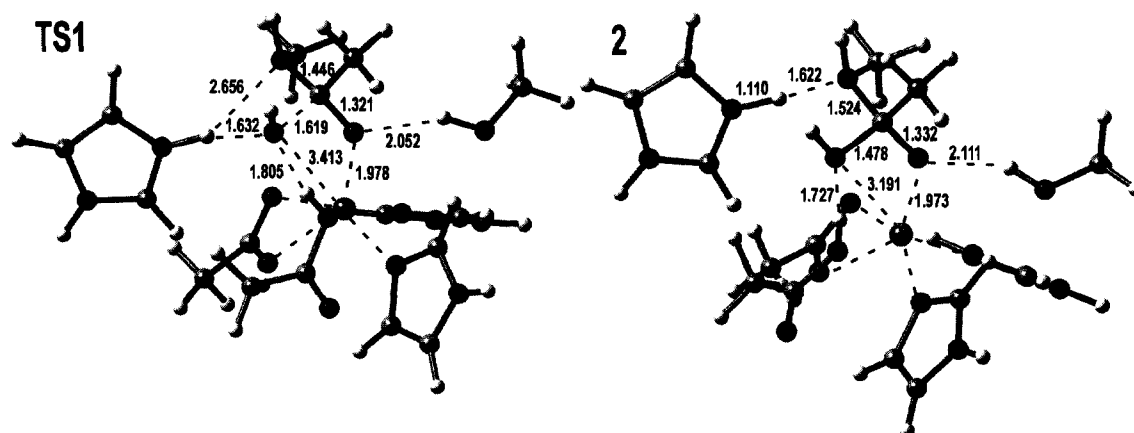


Figure 3.4. Optimized geometries of transition structure **TS1** and *gem*-diolate intermediate **2** arising from the addition of the hydroxide ion at the substrate's carbonyl carbon. Select optimized distances (Å) are also shown. [Zn (purple); C (gray); N (blue); O (red); H (white)].

Again, similar to the water-assisted mechanism, the second step is found to correspond to protonation of intermediate **2**'s nitrogen (N_1) center. If this reaction were to proceed via a single bifunctional acid/base amino acid residue as has been previously proposed,¹⁴ Glu78- H^+ would now have to act as an acid and donate its proton derived from the initial $Zn^{2+} \cdots OH_2$ moiety. However, based on the geometry of **2**, this seems unlikely as the distance between glutamate's proton and the amino nitrogen is 4.067 Å. Furthermore, the intermediate's hydroxyl group sits between them. Thus, the optimized structure of **2** appears to support the proposal of Hernick *et al.* that His265- H^+ is more aptly positioned to provide the additional proton in the alternate acid/base pair

mechanism.²² Indeed, the transfer of a proton from the protonated histidine to N₁ proceeds via **TS2** with a barrier of only 2.5 kJ mol⁻¹ to give the *gem*-diolate intermediate **3** which lies just 37.8 kJ mol⁻¹ higher in energy than **1A**. We note that the optimized structure of **TS2** is indicative of such a low, early reaction barrier with the transferring H⁺ lying much closer to the appropriate nitrogen center of His265 than that of the intermediate, as shown in Figure 3.5. In the resulting doubly protonated intermediate **3**, the N₁-H group forms a hydrogen bond (1.819 Å) to the basic N center of His265. However, the addition of the second proton to N₁ in **3** has not resulted in the cleavage of the C₁-N₁ bond, although it has lengthened significantly to 1.616 Å. This is unlike that observed in the water-assisted mechanism. Interestingly, the stability of **3** appears to be due, in large part, to its coordination to the Zn²⁺ ion via its remaining unprotonated oxygen (see Figure 3.5). For related models, when the Zn²⁺...O₁ interaction was broken, the C₁-N₁ bond instantly cleaved (not shown). As a result, unlike the water-assisted mechanism, LpxC requires additional reaction steps. We note that in **3** the C₁-O_w and C₁-O₁ distances have both shortened slightly by 0.042 and 0.020 Å, respectively, to 1.436 and 1.312 Å, compared to **2**. Furthermore, the active site interactions observed in **2** are retained. The hydrogen bond from O_w to the proton of glutamate has lengthened slightly to 1.826 Å, while that between the threonine-OH group and the oxyanion of the intermediate has shortened by 0.087 Å to 2.024 Å, compared to that observed in **2**. It should be noted, that related doubly protonated intermediates are mechanistically quite common among other previously theoretically investigated metallopeptidases (e.g., thermolysin,³⁹ peptide deformylase⁴⁰ and matrix metalloproteinases⁴¹). However, the above results suggest that LpxC forms this intermediate via a two step process whereas thermolysin,³⁹ peptide deformylase⁴⁰ and matrix metalloproteinases⁴¹ have all been found to achieve this intermediate in one step via a concomitant hydroxyl attack and proton transfer.

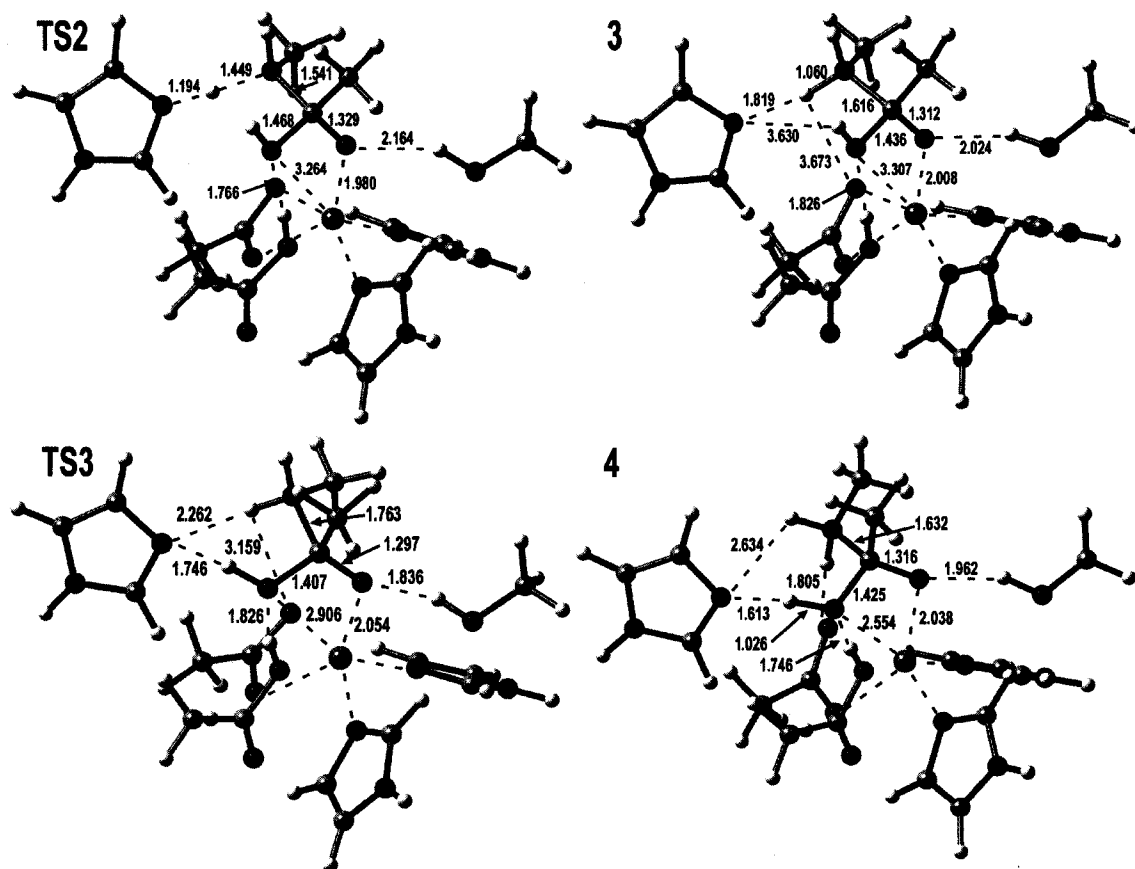


Figure 3.5. Optimized geometries of the transition structures and intermediates arising from proton transfer from His265-H⁺ to the amino nitrogen of the intermediate (**TS2** and **3**), as well as reorientation of His265 within the active site (**TS3** and **4**). Select optimized distances (Å) are also shown. [Zn (purple); C (gray); N (blue); O (red); H (white)].

From previous computational studies on the aforementioned metallopeptidase enzymes,³⁹⁻⁴³ cleavage of the C₁—N₁ bond is typically achieved by the transfer of the remaining C₁—O_wH proton from the intermediate to some nearby base in the active site. However, at this stage of the reaction there appears to be no amino acid residue immediately capable of accepting this proton in the LpxC active site in **3**. The Glu78-H⁺ residue already has the proton from the initial water moiety, while the nitrogen of His265 is hydrogen bonded to a proton of the intermediate's amino group. However, if the histidine were to break this hydrogen bond and instead form one with the C₁—O_wH

group of the intermediate, such a proton transfer might then be possible. Indeed, such a switch in the hydrogen-bonding network is found to proceed via **TS3** with little or no barrier to give intermediate **4** which now lies just 11.3 kJ mol⁻¹ higher in energy than **1A**. We note that the other metallopeptidases mentioned above do not exhibit a step analogous to this one due to the reasons indicated above.³⁹⁻⁴³ In **4**, His265 now forms a strong hydrogen bond (1.613 Å) with the substrate's -O_wH proton (Figure 3.5). In addition, it no longer interacts with the N₁-H amino proton (3.252 Å) which now forms a hydrogen bond with an oxygen of the Zn²⁺ coordinating Asp242 residue with a distance of 1.805 Å. The other proton on N₁ lies 2.634 Å away from the now basic nitrogen of His265. The hydrogen bonds from Thr191 and Glu78-H⁺ to O₁ and O_w respectively have both shortened in **4** to 1.962 Å and 1.746 Å, respectively. In addition, the Zn²⁺...O_w distance has also shortened significantly to 2.554 Å, while the Zn...O₁ interaction has lengthened slightly to 2.038 Å. The C-N bond of **4** has now also lengthened slightly by 0.016 Å to 1.632 Å (Figure 3.5).

The next, and final, step in the mechanism of LpxC is cleavage of the C₁-N₁ bond. This is achieved by transfer of the C₁-O_wH proton of the substrate to the nitrogen of His265. This reaction proceeds via **TS4** at a cost of only 15.0 kJ mol⁻¹ relative to **4**, 26.3 kJ mol⁻¹ overall. In the resulting final product complex **5**, the desired ultimate products have been formed but remain bound in the active site. Furthermore, it lies 26.0 kJ mol⁻¹ lower in energy than **1A** (Figure 3.3). In **5**, His265-H⁺ now forms a hydrogen bond through its newly acquired proton to O_w of the product acetate at a distance of 1.732 Å (Figure 3.6) which itself remains bound to the Zn²⁺ ion center. Notably, the acetate is now coordinated to the Zn²⁺ ion through both of its oxygens as illustrated by the Zn²⁺...O_w and Zn²⁺...O₁ optimized distances of 2.399 and 2.150 Å, respectively (Figure 3.6). The C₁-O_w and C₁-O₁ bonds are both much shorter at 1.287 and 1.265 Å, respectively, as expected for an acetate anion. Interestingly, the Glu78-H⁺ residue

still forms a strong Glu–OH \cdots O_w hydrogen bond with a length of 1.748 Å. This suggests that release of the product acetate may also result in regeneration of the initial Glu78 anion. The hydrogen bond between O₁ and Thr191 has also shortened by 0.098 Å to 1.864 Å. The product methylamine is found to also retain its hydrogen bond with an oxygen of Asp242, albeit it is now slightly longer at 2.180 Å. We note that the structure of **5** is similar to the reported structure of the product analogue palmitate bound to the Zn²⁺ ion in the active site. Indeed, the experimentally determined interatomic distances for the Zn²⁺ \cdots O_w, Zn²⁺ \cdots O₁, Glu(O) \cdots O_w, His(N) \cdots O_w and Thr(O) \cdots O₁ interactions are 2.3, 2.1, 3.0, 2.9 and 3.1 Å, respectively.²² Comparing these values to those obtained in our model, 2.4, 2.2, 2.7, 2.8 and 2.8 Å respectively, we see that our predicted interaction distances are generally in good agreement with those of the crystal structure.

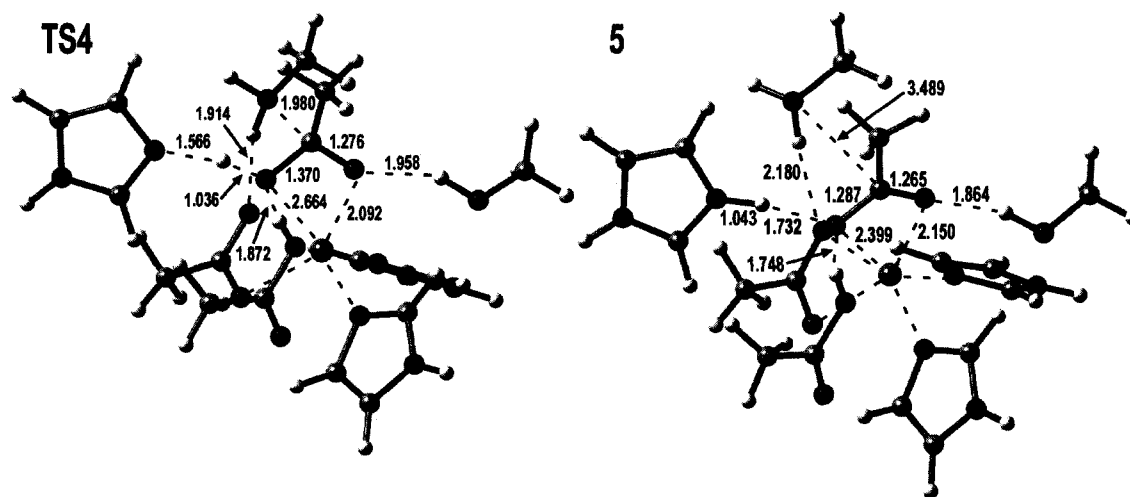


Figure 3.6. Optimized geometries of the transition structure and the resulting product complex associated with the transfer of the substrate's hydroxyl proton to His265. Select optimized distances (Å) are also shown. [Zn (purple); C (gray); N (blue); O (red); H (white)].

3.3.4 Overall Mechanism

It can be seen from Figure 3.3 that the overall rate-determining barrier of the mechanism is the nucleophilic attack of the hydroxide on the substrate, as this first step proceeds with a barrier of 87.7 kJ mol^{-1} . This is in agreement with the results from the step-wise water-assisted hydrolysis of the amide bond (Figure 3.1), as the hydroxylation is the highest energy step of this mechanism. Interestingly, from this step in the mechanism onward, all subsequent intermediates and transition structures are lower in energy than the one preceding it until the C—N bond is cleaved and the products are formed.

3.4 Conclusions

From the present DFT investigation into the hydrolysis of an amide bond via a water-assisted mechanism and the LpxC enzyme, several conclusions can be drawn:

- (1) Binding of the substrate to the LpxC active site preferentially occurs with the substrate's carbonyl oxygen coordinating to the Zn^{2+} ion between the Zn-bound water and the threonine residue. Interestingly, upon coordination of the substrate, the active site Glu78 readily deprotonates the Zn-bound water, resulting in a $\text{Zn}^{2+} \cdots \text{OH}^-$ moiety and Glu78-H^+ .
- (2) Similarly, in both the step-wise water-assisted mechanism and the LpxC mechanism, the initial step where the carbonyl carbon of the substrate is hydroxylated is the rate-determining step. However, the barrier for the LpxC mechanism (87.7 kJ mol^{-1}) is approximately half that of the water-assisted system ($172.5 \text{ kJ mol}^{-1}$). This is due in part to the increased nucleophilicity of the OH^- moiety compared to H_2O , as well as stabilization of the transition structure and initial *gem*-diolate intermediate by the active site.

- (3) Analogous to the water-assisted mechanism the proceeding step in the LpxC catalyzed reaction is a proton transfer to the amino nitrogen of the intermediate. LpxC employs the protonated histidine residue (His265-H⁺) in order to do so. However, unlike the water-assisted system, in which the amide bond is cleaved at this step, the resulting protonated intermediate is stabilized by coordination to the Zn²⁺ ion via its C—O⁻ oxyanion in the LpxC active site. Thus, additional reaction steps are required for cleavage of the amide bond.
- (4) The final two steps of the LpxC catalyzed reaction involve an initial change in the hydrogen-bonding network of His265 from an N₁—H group of the intermediate to the C₁—O_wH hydroxyl group, positioning itself to then abstract the hydroxyl proton resulting in the cleavage of the C—N bond. This step to change the hydrogen-bonding network is not required in other metallopeptidases investigated to date, as they already have a free basic residue properly situated to do so.
- (5) Overall, LpxC utilizes His265-H⁺ and Glu78 in an acid and base pair mechanism. Energetically, after the initial rate determining step, all subsequent minima and transition states are lower in energy than the corresponding stationary point preceding it.

References

- (1) Onishi, H. R.; Pelak, B. A.; Gerckens, L. S.; Silver, L. L.; Kahan, F. M.; Chen, M.-H.; Patchett, A. A.; Galloway, S. M.; Hyland, S. A.; Anderson, M. S.; Raetz, C. R. H. *Science* **1996**, *274*, 980.

- (2) Jackman, J. E.; Fierke, C. A.; Tumeyi, L. N.; Pirrung, M.; Uchiyama, T.; Tahir, S. H.; Hindsgaul, O.; Raetz, C. R. H. *J. Biol. Chem.* **2000**, *275*, 11002.
- (3) Clements, J. M.; Coignard, F.; Johnson, I.; Chandler, S.; Palan, S.; Waller, A.; Wijkmans, J.; Hunter, M. G. *Antimicrob. Agents Chemother.* **2002**, *46*, 1793.
- (4) White, R. J.; Margolis, P. S.; Trias, J.; Yuan, Z. *Curr. Opin. Pharmacol.* **2003**, *3*, 502.
- (5) McClerren, A. L.; Endsley, S.; Bowman, J. L.; Andersen, N. H.; Guan, Z.; Rudolph, J.; Raetz, C. R. H. *Biochemistry* **2005**, *44*, 16574.
- (6) Mdluli, K. E.; Witte, P. R.; Kline, T.; Barb, A. W.; Erwin, A. L.; Mansfield, B. E.; McClerren, A. L.; Pirrung, M. C.; Tumey, L. N.; Warrenner, P.; Raetz, C. R. H.; Stover, C. K. *Antimicrob. Agents Chemother.* **2006**, *50*, 2178.
- (7) Barb, A. W.; McClerren, A. L.; Snehelatha, K.; Reynolds, C. M.; Zhou, P.; Raetz, C. R. H. *Biochemistry* **2007**, *46*, 3793.
- (8) Kadam, R. U.; Chavan, A.; Roy, N. *Bioorg. Med. Chem. Lett.* **2007**, *17*, 861.
- (9) Andersen, M. S.; Bull, H. G.; Galloway, S. M.; Kelly, T. M.; Mohan, S.; Radika, K.; Raetz, C. R. H. *J. Biol. Chem.* **1993**, *268*, 19858.
- (10) Raetz, C. R. H.; Whitfield, C. *Annu. Rev. Biochem.* **2002**, *71*, 635.
- (11) Jackman, J. E.; Raetz, C. R. H.; Fierke, C. A. *Biochemistry* **1999**, *38*, 1902.
- (12) Jackman, J. E.; Raetz, C. R. H.; Fierke, C. A. *Biochemistry* **2001**, *40*, 514.
- (13) McClure, C. P.; Rusche, K. M.; Peariso, K.; Jackman, J. E.; Fierke, C. A.; Penner-Hahn, J. E. *J. Inorg. Biochem.* **2003**, *94*, 78.
- (14) Whittington, D. A.; Rusche, K. M.; Shin, H.; Fierke, C. A.; Christianson, D. W. *Proc. Natl. Acad. Sci. USA* **2003**, *100*, 8146.
- (15) Vallee, B. L.; Auld, D. S. *Biochemistry* **1990**, *29*, 5647.
- (16) Hernick, M.; Fierke, C. A. *Arch. Biochem. Biophys.* **2005**, *433*, 71.
- (17) Gennadios, H. A.; Whittington, D. A.; Li, X.; Fierke, C. A.; Christianson, D. W. *Biochemistry* **2006**, *45*, 7940.

- (18) Lipscomb, W. N.; Sträter, N. *Chem. Rev.* **1996**, *96*, 2375.
- (19) Coggins, B. E.; Li, X.; McClerren, A. L.; Hindsgaul, O.; Raetz, C. R. H.; Zhou, P. *Nature Struct. Biol.* **2003**, *10*, 645.
- (20) Coggins, B. E.; McClerren, A. L.; Jiang, L.; Li, H.; Rudolph, J.; Hindsgaul, O.; Raetz, C. R. H.; Zhou, P. *Biochemistry* **2005**, *44*, 1114.
- (21) McClerren, A. L.; Zhou, P.; Guan, Z.; Raetz, C. R. H.; Rudolph, J. *Biochemistry* **2005**, *44*, 1106.
- (22) Hernick, M.; Gennadios, H. A.; Whittington, D. A.; Rusche, K. M.; Christianson, D. W.; Fierke, C. A. *J. Biol. Chem.* **2005**, *280*, 16969.
- (23) Becke, A. D. *J. Chem. Phys.* **1993**, *98*, 1372.
- (24) Lee, C.; Yang, W.; Parr, R. G. *Phys. Rev. B* **1988**, *37*, 785.
- (25) Schrödinger, L. L. C. In *Jaguar 5.5* Portland, OR, 1991-2003.
- (26) Siegbahn, P. E. M.; Blomberg, M. R. A. *Chem. Rev.* **2000**, *100*, 421.
- (27) Noodleman, L.; Lovell, T.; Han, W.-G.; Li, J.; Himo, F. *Chem. Rev.* **2004**, *104*, 459.
- (28) Frisch, M. J.; Trucks, G. W.; Schlegel, H. B.; Scuseria, G. E.; Robb, M. A.; Cheeseman, J. R.; Montgomery, J. A. J.; Vreven, T.; Kudin, K. N.; Burant, J. C.; Millam, J. M.; Iyengar, S. S.; Tomasi, J.; Barone, V.; Mennucci, B.; Cossi, M.; Scalmani, G.; Rega, N.; Petersson, G. A.; Nakatsuji, H.; Hada, M.; Ehara, M.; Toyota, K.; Fukuda, R.; Hasegawa, J.; Ishida, M.; Nakajima, T.; Honda, Y.; Kitao, O.; Nakai, H.; Klene, M.; Li, X.; Knox, J. E.; Hratchian, H. P.; Cross, J. B.; Adamo, C.; Jaramillo, J.; Gomperts, R.; Stratmann, R. E.; Yazyev, O.; Austin, A. J.; Cammi, R.; Pomelli, C.; Ochterski, J.; Ayala, P. Y.; Morokuma, K.; Voth, G. A.; Salvador, P.; Dannenberg, J. J.; Zakrzewski, V. G.; Dapprich, S.; Daniels, A. D.; Strain, M. C.; Farkas, O.; Malick, D. K.; Rabuck, A. D.; Raghavachari, K.; Foresman, J. B.; Ortiz, J. V.; Cui, Q.; Baboul, A. G.; Clifford, S.; Cioslowski, J.; Stefanov, B. B.; Liu, G.; Liashenko, A.; Piskorz, P.; Komaromi, I.; Martin, R. L.; Fox, D. J.; Keith, T. A.; Al-Laham, M. A.; Peng, C. Y.;

- Nanayakkara, A.; Challacombe, M.; Gill, P. M. W.; Johnson, B. G.; Chen, W.; Wong, M. W.; Gonzalez, C.; Pople, J. A. Gaussian 03; Gaussian Inc.: Wallingford CT, 2004.
- (29) Oie, T.; Loew, G. H.; Burt, S. K.; Binkley, J. S.; MacElroy, R. D. *J. Am. Chem. Soc.* **1982**, *104*, 6169.
- (30) Krug, J. P.; Popelier, P. L. A.; Bader, R. F. W. *J. Phys. Chem.* **1992**, *96*, 7604.
- (31) Janssen, J. H.; Baldrige, K. K.; Gordon, M. S. *J. Phys. Chem.* **1992**, *96*, 8340.
- (32) Antonczak, S.; Ruiz-Lopez, M. F.; Rivail, J.-L. *J. Am. Chem. Soc.* **1994**, *116*, 3912.
- (33) Antonczak, S.; Ruiz-Lopez, M. F.; Rivail, J.-L. *J. Mol. Model.* **1997**, *3*, 434.
- (34) Kallies, B.; Mitzner, R. *J. Mol. Model.* **1998**, *4*, 183.
- (35) Zahn, D. *Eur. J. Org. Chem.* **2004**, 4020.
- (36) Gorb, L.; Asensio, A.; Tuñón, I.; Ruiz-Lopez, M. F. *Chem. Eur. J.* **2005**, *11*, 6743.
- (37) Gennadios, H. A.; Christianson, D. W. *Biochemistry* **2006**, *45*, 15216.
- (38) Hammond, G. S. *J. Am. Chem. Soc.* **1955**, *77*, 334.
- (39) Pelmeshnikov, V.; Blomberg, M. R. A.; Siegbahn, P. E. M. *J. Biol. Inorg. Chem.* **2002**, *7*, 284.
- (40) Leopoldini, M.; Russo, N.; Toscano, M. *J. Phys. Chem. B* **2006**, *110*, 1063.
- (41) Pelmeshnikov, V.; Siegbahn, P. E. M. *Inorg. Chem.* **2002**, *41*, 5959.
- (42) Wu, X.-H.; Quan, J.-M.; Wu, Y.-D. *J. Chem. Phys. B* **2007**, *111*, 6236.
- (43) Xiao, C.; Zhang, Y. *J. Phys. Chem. B* **2007**, *111*, 6229.

Chapter 4

A DFT Investigation on the Mechanism of the Second Half-Reaction of Nitric Oxide Synthase

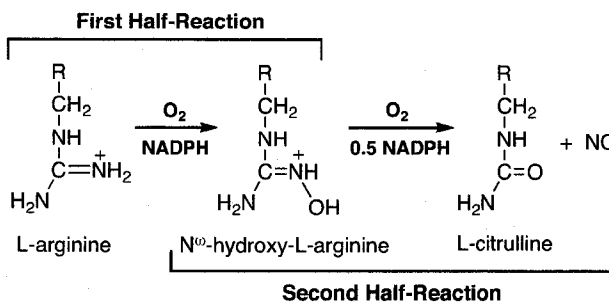
4.1 Introduction

Nitric oxide (NO) is an important biosignalling molecule that has been found to play key roles in a diverse range of physiological processes, including neurotransmission, blood pressure regulation and the immune system.¹⁻⁴ Consequently, there is considerable and increasing interest in better understanding its biological chemistry. Due in part to its central importance to NO-biochemistry, particular attention has focused on elucidating the mechanism by which it is synthesized *in vivo*.

Within mammals,^{5,6} NO is synthesized by the class of enzymes known as the Nitric Oxide Synthases (NOSs). Three NOS isozymes are known: neuronal (nNOS), endothelial (eNOS) and inducible (iNOS).⁶⁻⁸ Despite their differences, they have all been found to possess similar structures and require the same cofactors. For example, each isozyme can be divided into two domains: an N-terminal reductase and C-terminal oxygenase domain. The former binds the cofactors nicotinamide adenine dinucleotide phosphate (NADPH), flavin adenine dinucleotide (FAD) and flavin mononucleotide (FMN), and is responsible for donating electrons into the active site during the reaction.⁸⁻¹⁰ The latter contains the active site itself in which is bound a heme, immediately adjacent to which binds an (6R)-5,6,7,8-tetrahydro-L-biopterin (H₄B) moiety.^{7,8} Importantly, however, all three isozymes possess a very highly conserved active site. As a result, they are all believed to produce NO via the same enzymatic

mechanism, in which arginine is sequentially oxidized via two half-reactions to give citrulline and NO as illustrated in Scheme 4.1.

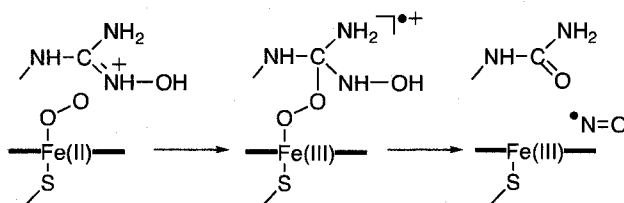
Scheme 4.1. The overall mechanism catalysed by nitric oxide synthases illustrating its two component half-reactions ($R = -(\text{CH}_2)_2\text{CH}(\text{NH}_2)\text{COOH}$).



In the first half-reaction, arginine is oxidized to give N^ω -hydroxy-L-arginine (NHA) as shown in Scheme 4.1. This is generally thought to occur via a mechanism analogous to that of P450-like oxidase enzymes, as it consumes one O_2 and two electrons from NADPH.^{8,11-13} In the second half-reaction, NHA is oxidized to ultimately give citrulline and NO. However, while this again consumes one O_2 , it requires just one additional electron. Remarkably, there appears to be no known analogous enzymatic reaction. As a result, this latter half-reaction has been the particular focus of numerous experimental investigations. Based on these studies, a number of mechanisms have been proposed and reviewed in detail elsewhere.^{8,11,14-20} Unfortunately, however, due to the elusiveness of intermediates to experimental observation beyond an $\text{Fe}_{\text{heme}}\text{-OO}^-$ intermediate,²¹ the exact mechanism remains unclear. Such studies were further hindered by uncertainties about the exact nature of the NHA substrate. Specifically, it was initially thought that its key $-\text{NOH}$ group was unprotonated. However, recent experimental²² and computational^{23,24} studies have suggested that it is in fact most likely protonated at its nitrogen centre, i.e., $-\text{NHOH}^+$. Nevertheless, while the proposed

mechanisms differ with respect to key mechanistic details, they generally share some common features that are summarized in Scheme 4.2. In particular, the second half-reaction is thought to begin with binding of an O_2 to the active site heme group with addition of an electron. The resulting $Fe_{\text{heme}}-O_2$ species (or derivative) is thought to then attack the NHA substrate (or derivative) at its guanidinium carbon (C_{guan}). The resulting 'tetrahedral' species containing a peroxo $Fe_{\text{heme}}-O-O-C_{\text{guan}}$ linkage is proposed to then react further to ultimately give citrulline and NO.

Scheme 4.2. Summary of common features of the various proposed mechanisms for the second half-reaction in which NO is formed via a tetrahedral intermediate. Note, proposed ionization and protonation states may vary.



Recently, however, a computational investigation²⁵ examined a variety of previously proposed 'tetrahedral' derivatives as well as some possible alternatives. Based on their results they suggested that such species most likely lie too high in energy to be mechanistically feasible. In addition, they also considered various possible initial steps that may occur once the O_2 is bound to the heme centre. Intriguingly, they found that the most likely initial step involves the transfer of both hydrogens from the substrate's protonated $-NHOH^+$ group to the $Fe_{\text{heme}}-O_2$ moiety to give a heme-bound hydrogen peroxide, i.e., $Fe_{\text{heme}}-(H)OOH$. Furthermore, such an intermediate was calculated to be almost thermoneutral with the initial reactants, lying just marginally higher in energy.²⁵

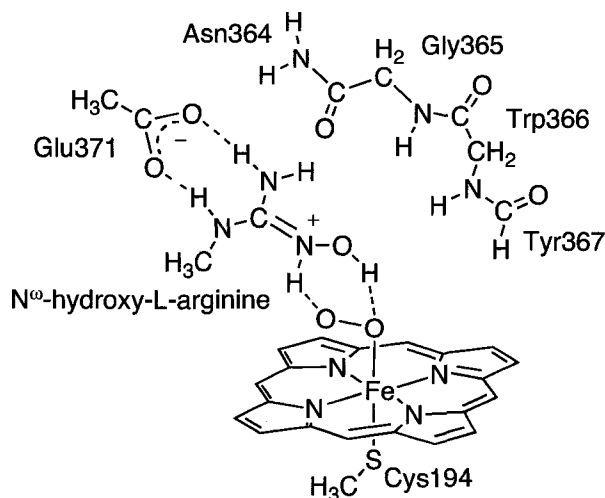
In this present chapter we have employed density functional theory methods to investigate the complete mechanism for the second half-reaction of Nitric Oxide Synthases.

4.2 Computational Methods

All calculations were performed using the hybrid density functional theory (DFT) method B3LYP, a combination of Becke's three-parameter hybrid exchange functional²⁶ with the Lee-Yang-Parr correlation functional²⁷ as implemented in Gaussian 03²⁸ and Jaguar 5.5.²⁹ Optimized structures and frequencies were obtained using the LACVP basis set on all atoms except sulfur for which LACV3P** was used. General effects due to the polarity of the protein environment (solvation correction) were modeled by performing single point calculations at the above level of theory on the optimized structures, using the Poisson-Boltzmann-PCM method with a dielectric constant (ϵ) of 4.0. Relative energies were obtained by performing single point calculations using the larger LACV3P** basis set on all atoms, i.e., at the B3LYP/LACV3P** level of theory, with inclusion of the appropriate solvation correction (ΔE^{solv}). Spin density values mentioned in the text were obtained at the above higher level of theory.

The active site was modeled as previously reported²⁵ based on the iNOS crystal structure PDB:1DWX¹⁴ (Scheme 3). Specifically, the heme was modeled as an Fe-porphyrin with a thiolmethyl anion as the axial Cys194, while the active site residue Glu371 was modeled as an acetate. The substrate NHA has been modeled by 1-methyl-2-hydroxy-guanidinium. The protein backbone between the carboxylate carbon of Asn364 and the amide nitrogen of Tyr367 has also been included. In order to maintain the integrity of the protein's active site, a minimal number of terminal atoms were held fixed according to their positions in the above crystal structure (highlighted in red in Scheme 4.3 and marked by an X in all Figures). See also reference 25 for further details.

Scheme 4.3. Schematic depiction of the active site of NOS as modeled in this chapter. Atoms highlighted in red were held fixed in the crystal structure position throughout the optimizations.



We have previously successfully employed the above methods and models to the study of the binding of NHA within the iNOS active site,²⁴ and to the study of possible tetrahedral intermediates and initial steps in the second half-reaction of NOSs.²⁵ The applicability of such computational approaches to the study of related enzymatic systems has also been previously discussed.³⁰

4.3 Results and Discussion

4.3.1 Substrate Bound Active Site and Initial Reaction Step

As noted in the introduction, computational methods have previously been used to investigate the binding of the substrate (NHA) within the active site with an O₂ moiety simultaneously bound to the Fe_{heme} centre.²⁴ In addition, a variety of possible initial steps for the second half-reaction were also considered.²⁵ It should be noted that in these previous studies an additional electron, from H₄B or NADPH, was also added to the system in order to enable the O₂ to bind to the Fe_{heme} centre.^{24,25} The resulting system, shown in Scheme 4.3, is hereafter referred to as the bound active site (1). In order to

assist in placing the present results into context, the most relevant findings from these previous computational studies are summarized here.

In **1**, the lowest energy structure corresponds to the -NHOH^+ group of NHA forming two hydrogen bonds with the Fe-bound O_2 ($\text{Fe}_{\text{heme}}\text{-O}_2$). Specifically, the -OH and -NH- groups hydrogen bond to the inner (O_{in}) and outer (O_{out}) oxygens of the $\text{Fe}_{\text{heme}}\text{-O}_2$ group respectively. In addition, the lowest energy state has a multiplicity (multi) of 1, i.e., $\mathbf{1}^1$. The most likely initial step was found to involve the concomitant transfer of both hydrogens from the -NHOH^+ group to O_2 moiety via the transition structure **TS1** with a relative energy barrier (multi = 1) of $14.8 \text{ kcal mol}^{-1}$.²⁵ The resulting $\text{Fe}_{\text{heme}}\text{-(H)OOH}$ intermediate ($\mathbf{2}^1$) was to lie only slightly higher in relative energy than $\mathbf{1}^1$ by $2.4 \text{ kcal mol}^{-1}$.²⁵

In this present chapter, the relative energies of the singlet and triplet states of the intermediates and transition structures encountered were found to generally lie quite close in energy and furthermore, lower than that of higher multiplicities. Thus, all relative energies mentioned herein refer to the multi = 1 and 3 states unless otherwise noted. However, as the structures of both states exhibit the same general features, only those of the singlets are shown herein while those of the corresponding triplets are given in Table B.1 of Appendix B.

4.3.2 Possible Reactions of the $\text{Fe}_{\text{heme}}\text{-(H)OOH}$ Intermediate

In this study, we began by systematically considering possible reaction pathways for the $\text{Fe}_{\text{heme}}\text{-(H)OOH}$ species (**2**). The schematic potential energy surfaces (PESs) obtained are shown in Figure 4.1 while optimized structures of the resulting singlet state transition structures and intermediates are shown in Figure 4.2.

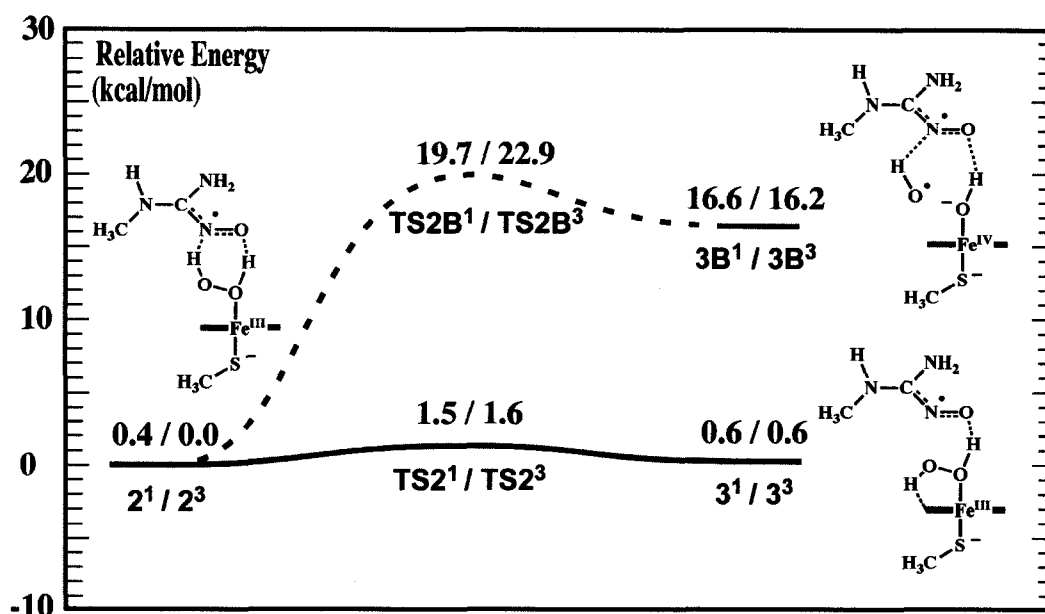


Figure 4.1. Schematic potential energy surfaces obtained for possible reactions of the $\text{Fe}_{\text{heme}}-(\text{H})\text{O}-\text{OH}$ intermediate **2**. Relative energies shown in kcal mol^{-1} .

As can be seen in Figure 4.1, the relative energies of the singlet and triplet states of **2** (2^1 and 2^3) are quite close with the triplet lying just $0.4 \text{ kcal mol}^{-1}$ lower in energy. The lowest energy reaction path for both states is found to correspond to simple rotation about the $\text{Fe}_{\text{heme}}(\text{H})\text{O}-\text{OH}$ bond. This conformational change proceeds via $\text{TS}2^1$ and $\text{TS}2^3$ with essentially equal barriers of just 1.5 and $1.6 \text{ kcal mol}^{-1}$ respectively. In the resulting alternate $\text{Fe}_{\text{heme}}-(\text{H})\text{O}-\text{OH}$ conformer **3**, the $-\text{O}_{\text{out}}\text{H}$ group is now directed down towards a nitrogen (N_{heme}) centre of the porphyrin with an $-\text{O}_{\text{out}}\text{H}\cdots\text{N}_{\text{heme}}$ distance of 2.049 \AA in 3^1 (Figure 2). In contrast, the $-\text{O}_{\text{in}}\text{H}-$ group remains hydrogen bonded to the oxygen of the substrate's $-\text{NO}$ group, although this bond has now shortened considerably. For example, as can be seen in Figure 4.2, in 3^1 it has a length of just 1.437 \AA , a decrease of 0.501 \AA from that observed for the corresponding intermediate 2^1 .²⁵ More importantly, however, 3^1 and 3^3 are calculated to lie very close in energy and furthermore, just $0.6 \text{ kcal mol}^{-1}$ higher in energy than the initial $\text{Fe}_{\text{heme}}-(\text{H})\text{O}-\text{OH}$ conformer 2^3 .

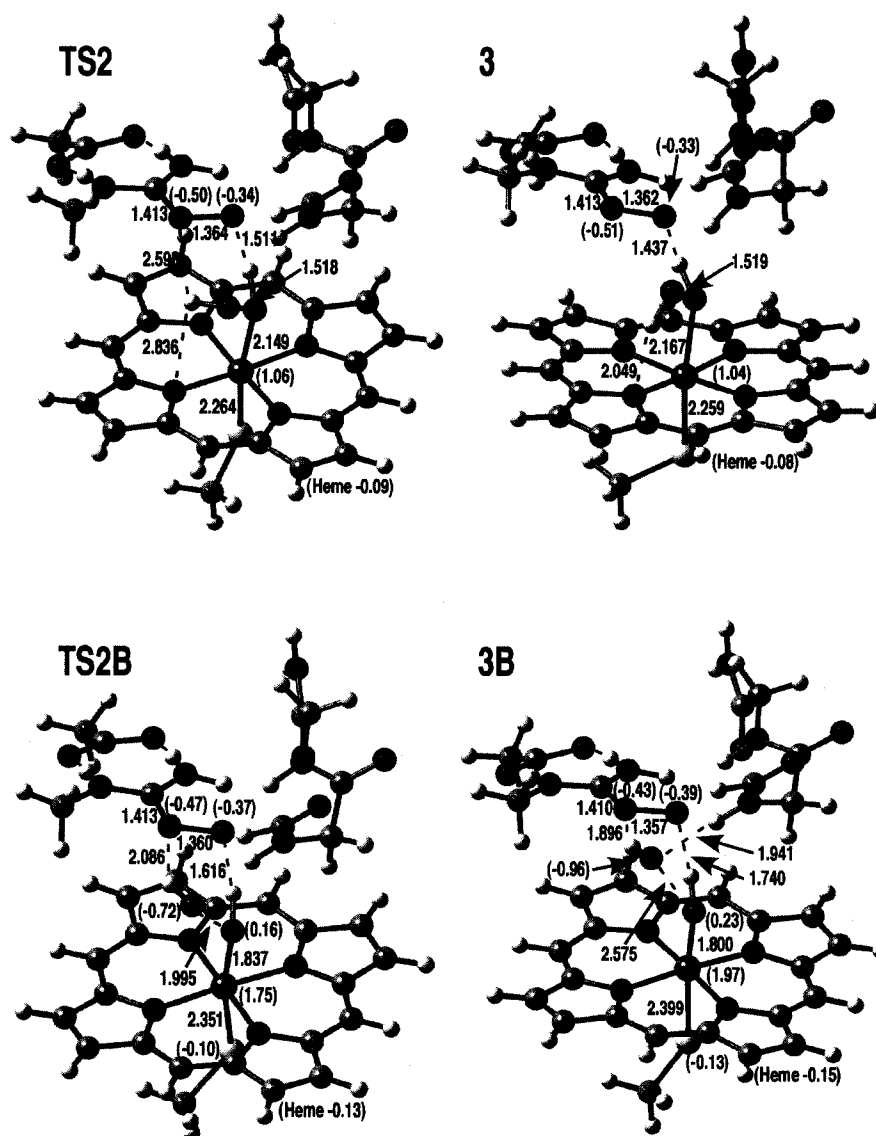


Figure 4.2. Optimized structures of the singlet state intermediates and transition structures shown in Figure 4.1 arising from the reaction of the $\text{Fe}_{\text{heme}}(\text{H})\text{O}-\text{OH}$ intermediate 2. Selected optimized distances (Å) and spin densities (in brackets) are also shown. [Fe (purple); S (yellow); C (gray); N (blue); O (red); H (white)].

A potential alternate pathway, shown in Figure 4.1 (red-dashed line), was also found in which the $\text{Fe}_{\text{heme}}(\text{H})\text{O}-\text{OH}$ bond undergoes homolytic cleavage to give an $\text{Fe}_{\text{heme}}-\text{OH}$ type species and $\cdot\text{OH}$ radical. An analogous reaction step for an $\text{Fe}_{\text{heme}}-\text{OOH}$ species has been previously considered in the mechanism of cytochrome P450cam.³¹

However, such a reaction proceeds via **TS2B** with very high relative energy barriers of 19.7 and 22.9 kcal mol⁻¹ for the singlet and triplet states respectively, (Figure 4.1). This is markedly higher than that of the above essentially free rotation path. Furthermore, the resulting intermediates formed by such a reaction, **3B¹** and **3B³**, lie significantly higher in energy than **2³** by 16.6 and 16.2 kcal mol⁻¹, respectively (Figure 4.1). Thus, in the present system such a reaction is highly unlikely to be competitive and hence is not discussed further.

4.3.3 Formation of 'Compound I' from *Fe_{heme}-(H)OOH Intermediate 3*

We then considered possible reactions of the *Fe_{heme}-(H)OOH* containing intermediate **3**. The reaction PES obtained is shown in Figure 4.3 while optimized structures of the various singlet state intermediates and transition structures are shown in Figure 4.4. As for the lower energy *Fe_{heme}-(H)OOH* conformer **2**, **3** can alternately also homolytically cleave at its O—O bond. However, such a mechanism was again found to have a significantly higher barrier to reaction. Thus, again, such a reaction is unlikely to be competitive.

Instead, the lowest energy pathway, other than rearrangement back to **2**, corresponds to transfer of the heme-peroxide's —O_{in}H— proton back to the substrate's —NO[•] group's oxygen. This reaction proceeds via **TS3¹** and **TS3³** at a cost of 12.2 and 13.9 kcal mol⁻¹, respectively (Figure 4.3). The singlet (**4¹**) and triplet (**4³**) states of the resulting intermediate **4** lie close in energy and just 9.0 and 9.1 kcal mol⁻¹, respectively, higher in relative energy than **3**. Based on the calculated spin densities and optimized structural parameters (Figure 4.4) the heme-oxy species within **4** resembles *Fe_{heme}-O(•)OH*, while the substrate derivative now contains a terminal =NOH^{•+} group. As a result, the *Fe_{heme}O—OH* bond has lengthened slightly. For example, the O—O bond in **4¹** is 0.038Å longer than observed for **3¹** (cf. Figure 4.2). Intriguingly, however,

as shown in Figure 4.4, the substrate's $=\text{NOH}^{++}$ moiety has in fact now formed a quite short hydrogen bond with the *outer* oxygen (O_{out}) of the $\text{Fe}_{\text{heme}}\text{-O}(\text{O})\text{OH}$ group.

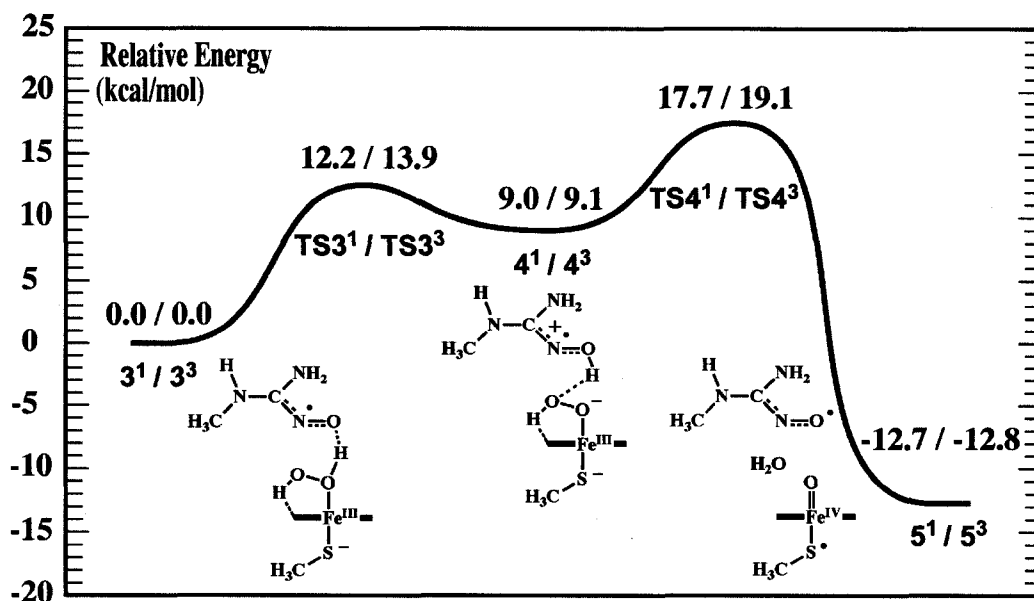


Figure 4.3. Schematic potential energy surface for the formation of Compound I from the $\text{Fe}_{\text{heme}}\text{-(H)O-OH}$ intermediate **3**. Relative energies shown in kcal mol^{-1} .

As might be anticipated based on the structure of **4**, its lowest energy reaction corresponds to transfer of the proton of the substrate's $=\text{NOH}^{++}$ group onto O_{out} of the $\text{Fe}_{\text{heme}}\text{-O}(\text{O})\text{OH}$ moiety. This step proceeds via TS4^1 and TS4^3 at a cost of 8.7 and 10.0 kcal mol^{-1} , respectively, and results in cleavage of the $\text{HO}_{\text{out}}\text{-O}_{\text{in}}$ bond with release of O_{out} as H_2O and with concomitant formation of a Compound I-type species (Figure 4.4). The corresponding resultant singlet and triplet product complexes **5**¹ and **5**³ are calculated to lie markedly lower in energy than **4**¹ by 21.7 and 21.5 kcal mol^{-1} respectively. In fact, as can be seen in Figure 4.3 they are also lower in energy than the initial $\text{Fe}_{\text{heme}}\text{-(H)OOH}$ complexes **3**¹ and **3**³. It is noted that in the iron-oxo moiety of **5**¹, the $\text{Fe}_{\text{heme}}\text{-O}$ bond has shortened significantly by 0.299 Å from that observed in **4**¹ to 1.650 Å (Figure 4.4). Conversely, the $\text{Fe}_{\text{heme}}\text{-S}$ bond has lengthened considerably by

0.282 Å to 2.621 Å. Similar changes in bond lengths were also observed for 5^3 . Notably, such bond lengths have previously been found to be characteristic of Compound I-type species.³²⁻³⁴

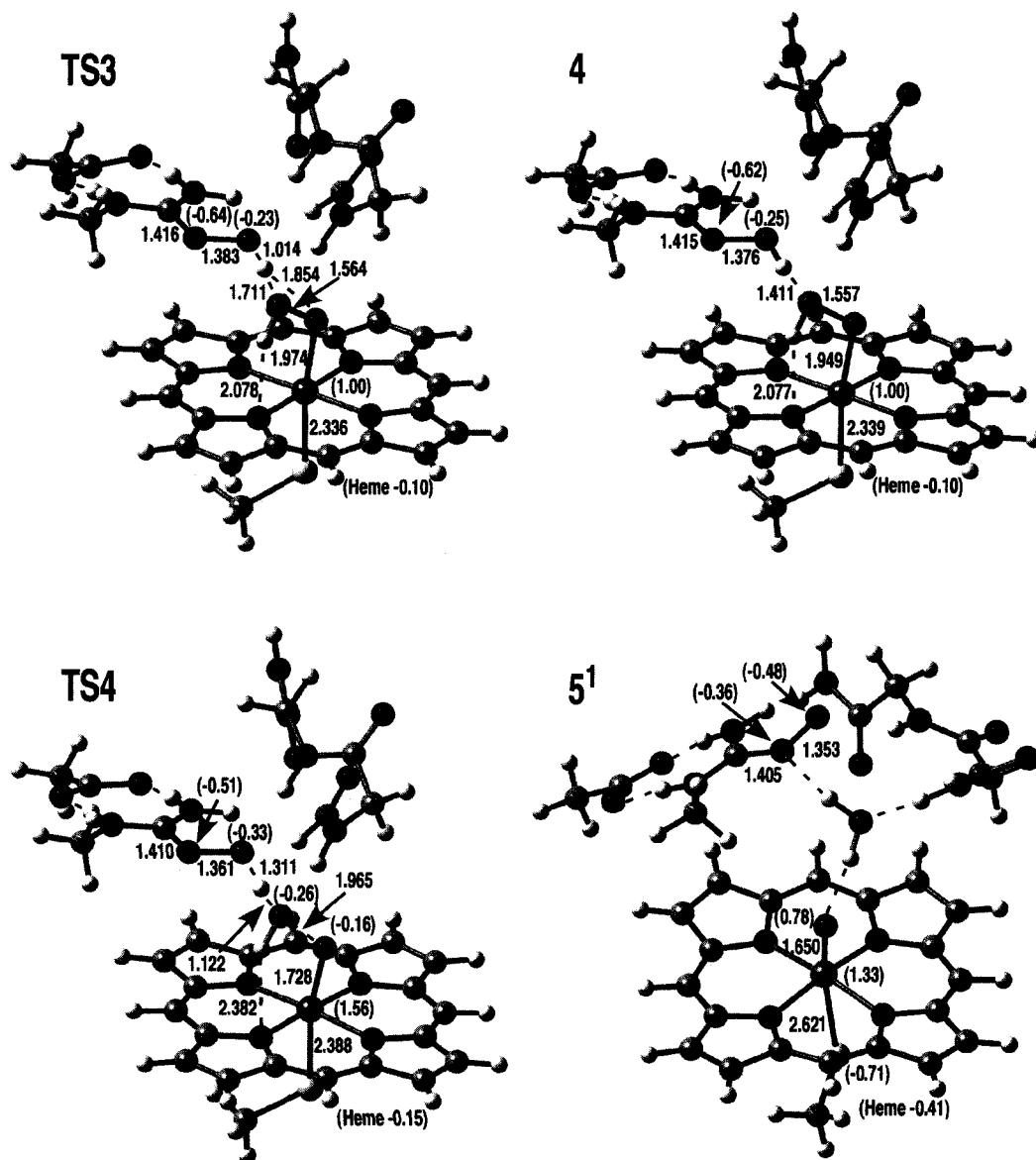


Figure 4.4. Optimized structures of the singlet state intermediates and transition structures shown in Figure 4.3 arising from the reaction of the $\text{Fe}_{\text{heme}}(\text{H})\text{O}-\text{OH}$ intermediate **3**. Selected optimized distances (Å) and spin densities (in brackets) are also shown. [Fe (purple); S (yellow); C (gray); N (blue); O (red); H (white)].

It is interesting to note that in the above pathway the formation of intermediate **4** effectively corresponds to transfer of just the -NH- hydrogen of the original NHA substrate's =NHOH^+ moiety to the initial $\text{Fe}_{\text{heme}}\text{-O}_2$ species. However, rather than occurring directly via the high energy intermediates identified previously²⁵ it has instead been achieved via a series of markedly lower energy intermediates and reactions. Previous experimental studies have suggested that NO formation still occurs, though at a reduced rate, when substrate analogs lacking the -OH proton are used.²⁰ The above results suggest that in such cases an intermediate **4**-type species could potentially still be formed, though by transfer of just the substrates relevant -NH- hydrogen via a series of higher energy intermediates and reactions.²⁵ Then, as in related P450-type enzymes, a second proton could possibly then be obtained from the aqueous solution or other source. Again this would result in the release of O_{out} as H_2O with concomitant formation of a Compound I-type species.

The overall pathway described above shows several similarities to enzymatic peroxidase-type mechanisms.³² Indeed, both employ a common intermediate $[\text{Fe}_{\text{heme}}\text{-(H)OOH}]$. Then, via a 'ping-pong' acid-base catalysis mechanism, they both transfer the proton from the $\text{-O}_{\text{in}}\text{H-}$ to the $\text{-O}_{\text{out}}\text{H}$ group of the heme-bound hydrogen peroxide. As a result, the O-O bond is cleaved with formation of water and a compound I species. However, unlike in the peroxidases, which have been shown to typically employ active site amino acid residues, for example histidine, in order to catalyse such a proton transfer,³² NOSs appear to utilize the substrate itself for this role.

4.3.4 Formation of the Final Products, Citrulline and NO

Possible mechanisms were then considered by which the heme-oxo (Compound I) component of intermediate complex **5** may react with the substrate derivative to give the final products, citrulline and NO. The schematic potential energy surface for the

lowest energy pathway obtained for the second half-reaction, including the final step, is shown in Figure 4.5, while the optimized structures for the triplet state of intermediate **5** (5^3) and corresponding triplet transition structure ($TS5^3$) and product (6^3) complexes are given in Figure 4.6.

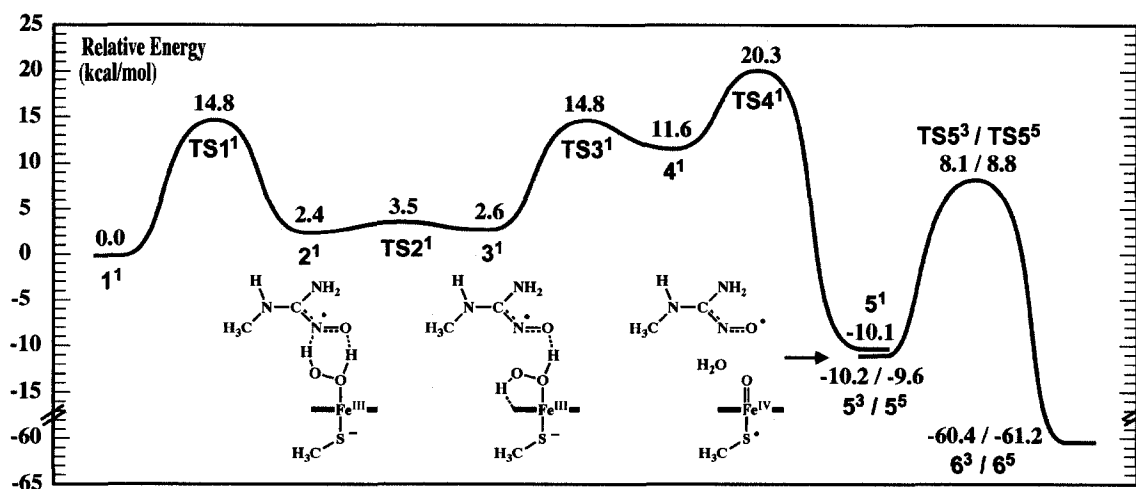


Figure 4.5. Schematic potential energy surface for the overall mechanism of the second half-reaction of NOSs. Relative energies shown in kcal mol⁻¹.

As noted above, the singlet state of **5** (5^1) is calculated to lie marginally higher in energy than the triplet (5^3) by 0.2 kcal mol⁻¹. However, it should also be noted that the quintet state 5^5 (Figure B.1 in Appendix B) lies just 0.5 kcal mol⁻¹ higher in energy. For 5^1 , the lowest energy pathway (not shown) found at the present level of theory corresponds to attack of the Fe_{heme}-O moiety at the nitrogen of the substrate's -NO group. However, such a reaction was calculated to have a quite a high reaction barrier of 23.1 kcal mol⁻¹.

Instead, a markedly lower energy pathway was found to occur via the triplet and quintet states of **5**, 5^3 and 5^5 , respectively. Specifically, in both cases the Fe_{heme}-O oxygen directly attacks at the substrate's C_{guan} centre via the 'tetrahedral-transition

structures' TS5^3 and TS5^5 at a cost of 18.3 and 18.4 kcal mol⁻¹, respectively, to directly give the corresponding final product complexes 6^3 and 6^5 , i.e., a one-step reaction. For the triplet and quintet state reactions the final product complexes 6^3 and 6^5 lie considerably lower in energy than their corresponding compound I reactant complexes 5^3 and 5^5 by 50.2 and 51.6 kcal mol⁻¹ respectively. The singlet state product complex 6^1 (Table B.1) lies 50.4 kcal mol⁻¹ lower in energy than 5^1 . It is noted that the final product complexes used in this present study correspond to the newly formed citrulline and NO remaining within the active site along with the H₂O released upon forming compound I.

It is interesting to note that while in both transition structures the Fe_{heme}—O bond is significantly lengthened, it does not yet appear to be completely broken. For example, in 5^3 the Fe_{heme}—O bond length is 1.650 Å, while in the corresponding transition structure TS5^3 it is now significantly longer at 1.936 Å (Figure 4.6). However, this latter distance is still shorter than that observed in the initial bound active site complex 1^1 .^{24,25} As described in the introduction, nearly all previously proposed mechanisms have involved the formation of a tetrahedral intermediate in which an Fe_{heme}—O₂ species attacks the substrate C_{guan} centre to form an Fe_{heme}—O—O—C_{guan} linkage. The present study suggests that while such 'tetrahedral' peroxo-linked intermediates do not play a role in the second half-reaction of NOSs, a 'tetrahedral' Fe_{heme}—O—C_{guan} oxo-linked transition structure does. It is also noted that the mechanism shown in Figure 4.5 shares some similarities to one previously proposed by Crane and coworkers¹⁴ based on their experimental observations. In particular, they suggested that a Compound I species is formed during the second half-reaction. However, they suggested that this occurs via a P450-like mechanism and that furthermore, it reacts with the substrate to form an oxaziridine species which undergoes an intramolecular rearrangement to give the final products, rather than via the above direct attack at C_{guan} route.

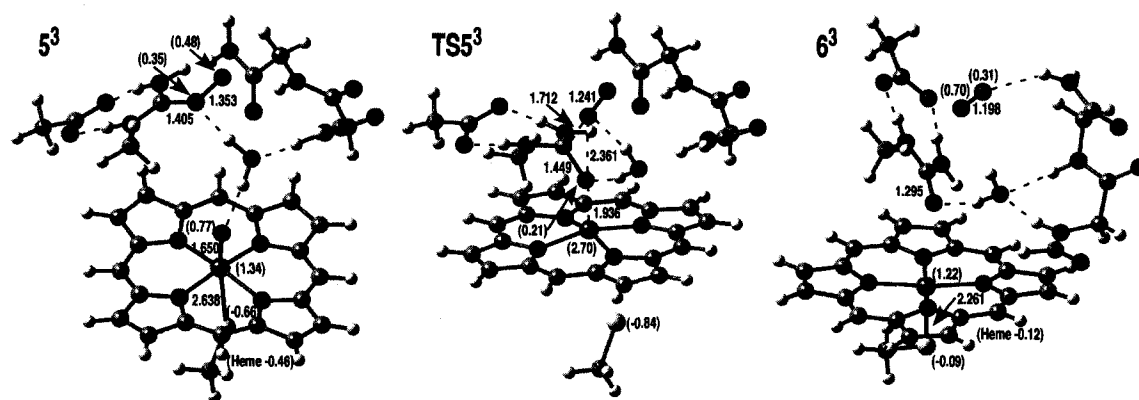


Figure 4.6. Optimized structures of the triplet state intermediate **5** (5^3) and corresponding transition structure ($TS5^3$) for formation of the triplet product (6^3) complex. Selected optimized distances (Å) and spin densities (in brackets) are also shown. [Fe (purple); S (yellow); C (gray); N (blue); O (red); H (white)].

4.4 Conclusions

In this present chapter, we have used density functional theory (DFT) methods in combination with large active site models in order to investigate the second half-reaction of nitric oxide synthases (NOSs). Specifically, we first investigated the possible reactions of the previously²⁵ suggested most probable initial intermediate $Fe_{\text{heme}}-(H)OOH$ (**2**). We have then systematically investigated the possible reactions of the subsequent intermediates in order to elucidate the overall lowest energy pathway leading to formation of citrulline and NO from NHA. It is noted that our active site model corresponds to the addition of one substrate NHA molecule and O_2 to the active site along with one additional electron. This corresponds to that which is known from experiments to be consumed during the second half-reaction.

It is found that once both protons of the $-NHOH^+$ group of the initial NHA substrate transfer to the heme-bound O_2 ($Fe_{\text{heme}}-O_2$) to give the $Fe_{\text{heme}}-(H)OOH$ intermediate **2**, the lowest energy pathway corresponds to an effectively free rotation

about the peroxide bond. This leads to the formation of the alternate $\text{Fe}_{\text{heme}}\text{-(H)OOH}$ conformer **3** in which the $\text{-O}_{\text{out}}\text{H}$ proton is directed downwards towards the heme porphyrin, while the $\text{-O}_{\text{in}}\text{H}$ group remains hydrogen bonded to the oxygen of the substrate -NO group. Furthermore, both the singlet and triplet states of **3** (3^1 and 3^3 , respectively) are almost thermoneutral with the initial $\text{Fe}_{\text{heme}}\text{-(H)OOH}$ intermediate **2** lying just $0.6 \text{ kcal mol}^{-1}$ higher in energy. The proton of the $\text{Fe}_{\text{heme}}\text{-O}_{\text{in}}\text{H}$ group can then transfer back to the oxygen of the substrate -NO group, thus forming an $\text{Fe}_{\text{heme}}\text{-OOH}$ species, while the substrate now contains a terminal =NOH^{++} group (**4**). The latter -NOH moiety is then able to transfer its proton to the *outer* oxygen (O_{out}) of the $\text{Fe}_{\text{heme}}\text{-OOH}$ species, causing the release of O_{out} as H_2O with concomitant formation of a Compound I-type species ($\text{Fe}_{\text{heme}}\text{-O}$). This final proton transfer is found to correspond to the highest overall barrier of the mechanism.

This pathway is analogous to the ping-pong mechanism by which heme peroxidases form a Compound I species from an initial $\text{Fe}_{\text{heme}}\text{-(H)OOH}$ species. Now, however, the substrate itself appears to play a role in its own oxidation by acting as the amino acid 'base species' that such peroxidases commonly use to transfer the proton from the $\text{-O}_{\text{in}}\text{H}$ to $\text{-O}_{\text{out}}\text{H}$ group.

The formation of the final products, citrulline and NO, is then found to be able to occur via a one-step reaction. Specifically, the lowest energy pathway is found to involve attack of the $\text{Fe}_{\text{heme}}\text{-O}$ moiety at the C_{guan} centre of the substrate via a 'tetrahedral-like' transition structure (TSS^3) containing a heme-oxo cross-link $\text{Fe}_{\text{heme}}\text{-O-C}_{\text{guan}}$, which 'decomposes' to give citrulline and NO directly.

References

- (1) Kerwin Jr., J. F.; Lancaster Jr., J. R.; Feldman, P. L. *J. Med. Chem.* **1995**, *38*, 4343.

- (2) Garthwaite, J.; Boulton, C. L. *Annu. Rev. Physiol.* **1995**, *57*, 683.
- (3) Schmidt, H. H. H. W.; Walter, U. *Cell* **1994**, *78*, 919.
- (4) Nath, A. K.; Madri, J. A. *Devel. Biol.* **2006**, *292*, 25.
- (5) Stuehr, D. J. *Biochem. Biophys. Acta* **1999**, *1411*, 217.
- (6) Knowles, R. G.; Moncada, S. *Biochem. J.* **1994**, *298*, 249.
- (7) Wei, C.-C.; Crane, B. R.; Stuehr, D. J. *Chem. Rev.* **2003**, *103*, 2365.
- (8) Alderton, W. K.; Cooper, C. E.; Knowles, R. G. *Biochem. J.* **2001**, *357*, 593.
- (9) Guan, Z.-W.; Kamatani, D.; Kimura, S.; Iyanagi, T. *J. Biol. Chem.* **2003**, *278*, 30859.
- (10) Jachymova, M.; Martasek, P.; Panda, S.; Roman, L. J.; Panda, M.; Shea, T. M.; Ishimura, Y.; Kim, J.-J. P.; Masters, B. S. S. *Proc. Natl. Acad. Sci. USA* **2005**, *102*, 15833.
- (11) Griffith, O. W.; Stuehr, D. J. *Annu. Rev. Physiol.* **1995**, *57*, 707.
- (12) Stuehr, D. J.; Santolini, J.; Wang, Z.-Q.; Wei, C.-C.; Adak, S. *J. Biol. Chem.* **2004**, *279*, 36167.
- (13) Crane, B. R.; Arvai, A. S.; Ghosh, D. K.; Wu, C.; Getzoff, E. D.; Stuehr, D. J.; Tainer, J. A. *Science* **1998**, *279*, 2121.
- (14) Crane, B. R.; Arvai, A. S.; Ghosh, S.; Getzoff, E. D.; Stuehr, D. J.; Tainer, J. A. *Biochem.* **2000**, *39*, 4608.
- (15) Rusche, K. M.; Spiering, M. M.; Marletta, M. A. *Biochem.* **1998**, *37*, 15503.
- (16) Clague, M. J.; Wishnok, J. S.; Marletta, M. A. *Biochem.* **1997**, *36*, 14465.
- (17) Korth, H.-G.; Sustmann, R.; Thater, C.; Butler, A. R.; Ingold, K. U. *J. Biol. Chem.* **1994**, *269*, 17776.
- (18) Marletta, M. A. *J. Biol. Chem.* **1993**, *268*, 12231.
- (19) Rosen, G. M.; Tsai, P.; Pou, S. *Chem. Rev.* **2002**, *102*, 1191.
- (20) Huang, H.; Hah, J.-M.; Silverman, R. B. *J. Am. Chem. Soc.* **2001**, *123*, 2674.
- (21) Davydov, R.; Ledbetter-Rogers, A.; Martásek, P.; Larukhin, M.; Sono, M.; Dawson, J. H.; Masters, B. S. S.; Hoffman, B. M. *Biochem.* **2002**, *41*, 10375.

- (22) Tierney, D. L.; Huang, H.; Martásek, P.; Roman, L. J.; Silverman, R. B.; Masters, B. S. S.; Hoffman, B. M. *J. Am. Chem. Soc.* **2000**, *122*, 5405.
- (23) Tantillo, D. J.; Fukuto, J. M.; Hoffman, B. M.; Silverman, R. B.; Houk, K. N. *J. Am. Chem. Soc.* **2000**, *122*, 536.
- (24) Cho, K. B.; Gault, J. W. *J. Am. Chem. Soc.* **2004**, *126*, 10267.
- (25) Cho, K. B.; Gault, J. W. *J. Phys. Chem. B* **2005**, *109*, 23706.
- (26) Becke, A. D. *J. Chem. Phys.* **1993**, *98*, 1372.
- (27) Lee, C.; Yang, W.; Parr, R. G. *Phys. Rev. B* **1988**, *37*, 785.
- (28) Frisch, M. J.; Trucks, G. W.; Schlegel, H. B.; Scuseria, G. E.; Robb, M. A.; Cheeseman, J. R.; Montgomery, J. A. J.; Vreven, T.; Kudin, K. N.; Burant, J. C.; Millam, J. M.; Iyengar, S. S.; Tomasi, J.; Barone, V.; Mennucci, B.; Cossi, M.; Scalmani, G.; Rega, N.; Petersson, G. A.; Nakatsuji, H.; Hada, M.; Ehara, M.; Toyota, K.; Fukuda, R.; Hasegawa, J.; Ishida, M.; Nakajima, T.; Honda, Y.; Kitao, O.; Nakai, H.; Klene, M.; Li, X.; Knox, J. E.; Hratchian, H. P.; Cross, J. B.; Adamo, C.; Jaramillo, J.; Gomperts, R.; Stratmann, R. E.; Yazyev, O.; Austin, A. J.; Cammi, R.; Pomelli, C.; Ochterski, J.; Ayala, P. Y.; Morokuma, K.; Voth, G. A.; Salvador, P.; Dannenberg, J. J.; Zakrzewski, V. G.; Dapprich, S.; Daniels, A. D.; Strain, M. C.; Farkas, O.; Malick, D. K.; Rabuck, A. D.; Raghavachari, K.; Foresman, J. B.; Ortiz, J. V.; Cui, Q.; Baboul, A. G.; Clifford, S.; Cioslowski, J.; Stefanov, B. B.; Liu, G.; Liashenko, A.; Piskorz, P.; Komaromi, I.; Martin, R. L.; Fox, D. J.; Keith, T. A.; Al-Laham, M. A.; Peng, C. Y.; Nanayakkara, A.; Challacombe, M.; Gill, P. M. W.; Johnson, B. G.; Chen, W.; Wong, M. W.; Gonzalez, C.; Pople, J. A. *Gaussian 03*; Gaussian Inc.: Wallingford CT, 2004.
- (29) Schrodinger, L. L. C. In *Jaguar 5.5* Portland, OR, 1991-2003.
- (30) Blomberg, M. R. A.; Siegbahn, P. E. M. *J. Phys. Chem. B* **2001**, *105*, 9375.
- (31) Zheng, J.; Wang, D.; Thiel, W.; Shaik, S. *J. Am. Chem. Soc.* **2006**, *128*, 13204.
- (32) Wirstam, M.; Blomberg, M. R. A.; Siegbahn, P. E. M. *J. Am. Chem. Soc.* **1999**, *121*, 10178.

-
- (33) Shaik, S.; de Visser, S. P.; Kumar, D. *J. Biol. Inorg. Chem.* **2004**, *9*, 661.
- (34) Shaik, S.; Kumar, D.; de Visser, S. P.; Altun, A.; Thiel, W. *Chem. Rev.* **2005**, *105*, 2279.

Chapter 5

A Computational Study on the Interaction of the Nitric Oxide Ions NO^+ and NO^- with the Side Groups of the Aromatic Amino Acids

5.1 Introduction

Nitric oxide (NO) has long been of interest due in part to its role as an atmospheric pollutant.¹ This interest increased dramatically with the discovery of its *in vivo* synthesis² and the ongoing unveiling of its diverse physiological roles as an important secondary messenger molecule.³ In addition to $\cdot\text{NO}$ itself, the nitrosium cation (NO^+) and nitroxyl anion (NO^-) are also thought to be responsible for at least some of the diverse functions of nitric oxide.⁴⁻⁸ Furthermore, some of the roles of these NO species have also been attributed to *S*-nitrosothiols (RSNO's),⁹⁻¹¹ a common form for transporting and delivering NO and its ions around the body. For instance, NO^+ is thought to induce the release of Ca^{2+} from smooth muscle in a cGMP-independent manner,⁴ while the nitroxyl anion, or at least in its protonated form (HNO), is known to be able to modify the activity of some enzymes and receptors.⁵ Some of these regulatory roles are achieved via covalent modifications of amino acid residues. Recently, however, it was shown that *S*-nitrosoglutathione (GSNO) can non-covalently interact with aromatic rich regions of proteins and remarkably, induce structural changes.¹²

Many cations are known to be able to participate in non-covalent interactions with the π -systems of electron rich aromatic compounds.^{13,14} Such interactions themselves have been extensively studied and are now known to also be important in an array of

physiological functions including the structure and function of proteins.¹⁵⁻¹⁸ In addition to π ···cation or "half-sandwich" complexes, such interactions may also lead to the formation of π ···cation··· π or "sandwich" complexes. In particular, there is increasing experimental evidence that some proteins contain multiple aromatic rings that interact with a single cation.^{14,17} While such species are well-known in organometallic chemistry, their nature and potential roles in biochemical systems are less understood. Unfortunately, despite their importance, to date there have been relatively few studies on such species. Furthermore, those studies that have considered related model systems have in general only examined the interactions of cations with simple aromatic species such as benzene, pyrrole, and indole as models of the aromatic amino acids.¹⁷ It has been found that anions can also form analogous anion··· π complexes if the aromatic species is electron deficient.^{19,20} However, it was also determined that the anions may interact by forming hydrogen bonds.²⁰ In general, this occurs via appropriate substituents such as -OH or -NH- groups. However, C—H bonds are also polarized, although to a lesser extent, and have also been found to participate in hydrogen bonding.^{21,22} Indeed, such interactions have been previously shown to be important in a variety of biological activities.^{23,24}

Previously, the interaction of \bullet NO and NO⁺ with benzene has been investigated both experimentally²⁵⁻²⁸ and computationally.²⁸⁻³³ In particular, it was found²⁹ that \bullet NO can interact with the π -system of benzene, though only weakly, while in contrast, NO⁺ can form strong cation··· π interactions with aromatic compounds.^{28,30-33} However, their interaction and that of NO⁻ with biochemically important aromatic biomolecules have not been previously reported. In addition, recent experimental studies by Rosokha *et al.*^{26,27} found that remarkably, NO⁺ is also capable of forming sandwich complexes with aromatic species. However, they suggested that not all arenes were capable of forming such structures.

In this present chapter we have employed *ab initio* and density functional theory methods in order to investigate the interactions of the biochemically important NO⁺ and NO⁻ ions with benzene and the aromatic side chains of the amino acids phenylalanine, tyrosine, histidine and tryptophan (Figure 5.1). Furthermore, we have also examined the structures and energetics of their corresponding sandwich complexes.

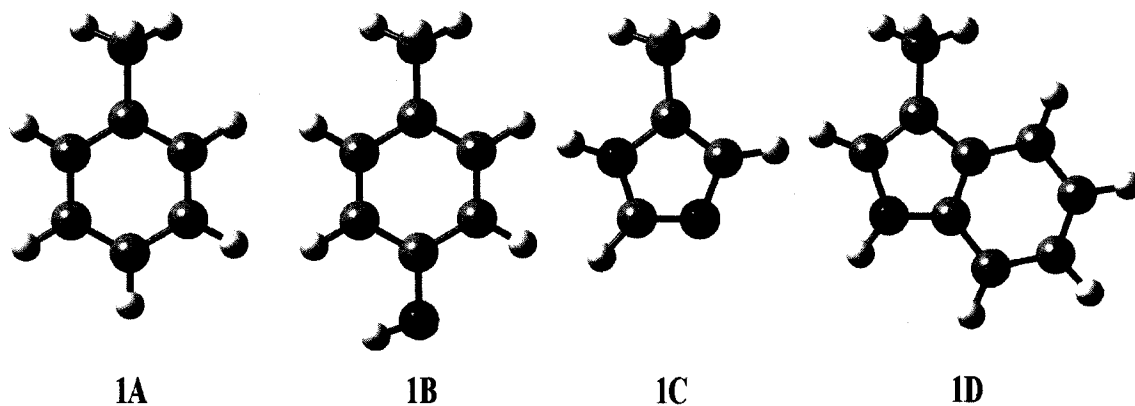


Figure 5.1. Models used in this present study for the side (R-) groups of the aromatic amino acids (1A) phenylalanine (Phe), (1B) tyrosine (Tyr), (1C) histidine (His) and (1D) tryptophan (Trp). [C (gray); N (blue); O (red); H (white)].

5.2 Computational Methods

All calculations were performed using the Gaussian 03³⁴ suite of programs. Density functional theory (DFT) calculations were performed using the B3LYP method, a pairing of Becke's three-parameter hybrid exchange functional³⁵ as implemented in the above programs³⁶ with the Lee-Yang-Parr correlation functional.³⁷ Depending on the chemical system, it was used in combination with a variety of Pople basis sets ranging from 6-311G(d,p) to 6-311+G(2df,p) as well as Dunning's aug-cc-pVDZ and aug-cc-pVTZ basis sets. The latter two basis sets were also used in combination with the *ab initio* Møller-Plesset second-order perturbation (MP2) method. Restricted methods were

used for all closed-shell species and complexes involving NO⁺. Unrestricted methods were used for all open-shell species and complexes with NO⁻, due to its ground-state triplet multiplicity. Spin contamination in all unrestricted calculations was negligible, with all $\langle S^2 \rangle$ values lying in the range 2.007 – 2.051 (see Table C.1 in Appendix C). In addition, for all complexes the stability of the wave function^{38,39} was tested and verified at each level of theory employed. Harmonic vibrational frequencies were obtained at each level of theory except MP2/aug-cc-pVTZ in order to verify that each complex obtained was an energy minimum. Complexation energies were corrected by including the appropriate zero-point vibrational energy (ZPVE), the MP2/aug-cc-pVDZ calculated ZPVE being used for MP2/aug-cc-pVTZ, and basis set superposition error (BSSE) correction as determined using the counterpoise method.^{40,41} The resulting energies (kJ mol⁻¹) are denoted by ΔE_{corr} . Unless otherwise noted, the abbreviations Phe, Tyr, His, and Trp refer to the models of the respective aromatic amino acids.

5.3 Results and Discussion

5.3.1 Assessment of Computational Methods

In computational studies, the size of the chemical system can impose a limit on the choice of method. Ultimately, we wish to investigate large sandwich-type complexes, beyond the tractability of most *ab initio* methods. Hence, we began by considering the ability of the widely used DFT method B3LYP in conjunction with a variety of basis sets to provide reliable results for aromatic...NO^{+/-} systems. The simplest complexes examined as part of this present study were considered, C₆H₆...NO^{+/-}, with the results being compared with those obtained at the conventional MP2/aug-cc-pVTZ level of theory.

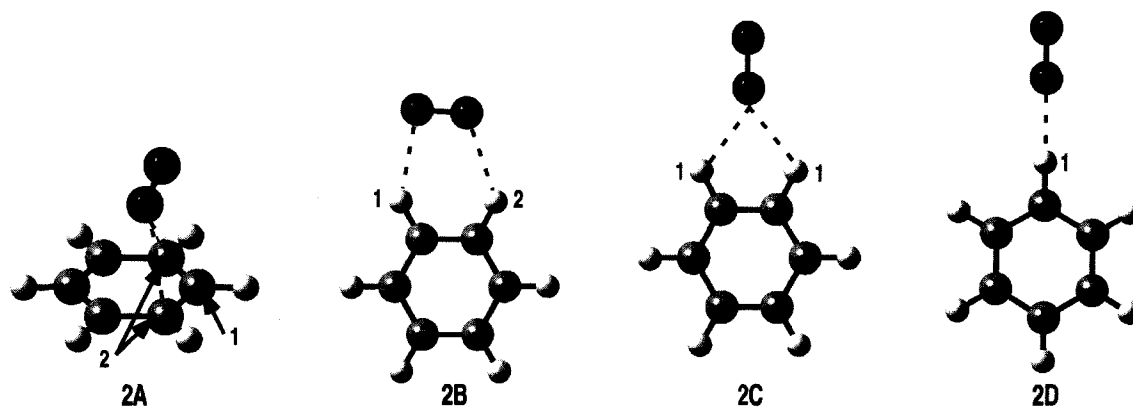


Figure 5.2. Illustration of the optimized structures of (**2A**) C₆H₆...NO⁺ and C₆H₆...NO⁻ with NO⁻ bound (**2B**) side-on or N-end-on via (**2C**) two hydrogen bonds or (**2D**) one hydrogen bond. [C (gray); N (blue); O (red); H (white)].

Table 5.1. Selected Optimized Distances (Å) and Complexation Energy (kJ mol⁻¹) of C₆H₆...NO⁺ (**2A**) Obtained Using the B3LYP and MP2 Methods in Combination with a Range of Basis Sets

Level of Theory					
Method	Basis Set	$r(\text{N}-\text{O})$	$r(\text{N}\cdots\text{C}_1)$	$r(\text{N}\cdots\text{C}_2)$	ΔE_{corr}
B3LYP	6-311G(d,p)	1.100	2.476	2.546	193.7
	6-311+G(d,p)	1.101	2.469	2.542	189.9
	6-311G++(d,p)	1.101	2.469	2.543	190.0
	6-311G(df,p)	1.098	2.484	2.547	190.8
	6-311G(2d,p)	1.099	2.450	2.530	193.5
	6-311+G(2df,p)	1.097	2.452	2.534	186.5
	aug-cc-pVDZ	1.109	2.450	2.526	194.6
	aug-cc-pVTZ	1.097	2.446	2.533	187.2
MP2	aug-cc-pVDZ	1.139	2.491	2.505	153.8
	aug-cc-pVTZ	1.125	2.400	2.455	158.7

$\text{C}_6\text{H}_6 \cdots \text{NO}^+$ complexes. Upon interacting, at all levels of theory, NO^+ binds towards one end of the face of C_6H_6 with its oxygen directed up and outwards from the face along a C—H bond (Figure 5.2), in agreement with previous observations.^{28,30-33} Selected optimized distances of the resulting C_s symmetric complex **2A** are given in Table 5.1.

Comparing the results obtained using both the B3LYP and MP2 methods with the aug-cc-pVTZ basis set enables evaluation of the applicability of the former method for such systems. The MP2 method predicts that upon binding to C_6H_6 , the bond length of the NO moiety ($r(\text{N—O})$) lengthens by 0.043 Å to 1.125 Å. Indeed, it is now only marginally shorter than the bond length of isolated $\bullet\text{NO}$ (Table 5.2). Thus, the complex formed resembles $\text{C}_6\text{H}_6^{\bullet+} \cdots \bullet\text{NO}$, i.e., almost complete electron transfer (see Table C.1 for atomic charges of all complexes). The B3LYP method also predicts $r(\text{N—O})$ to lengthen by 0.04 Å upon complexation. However, it has lengthened to just 1.097 Å, midway between the bond lengths of NO^+ and $\bullet\text{NO}$, as calculated at the same level of theory (Table 5.2). The resultant complex can thus be described as $[\text{C}_6\text{H}_6 \cdots \text{NO}]^+$, i.e., only partial electron transfer. It should be noted that B3LYP in combination with any basis set used in this present study gives $r(\text{N—O})$ of NO^+ to be approximately 0.03 Å shorter than obtained at the MP2 level (Table 5.2). The experimental adiabatic ionization energies (IE's) of C_6H_6 and NO are close at 891.9 and 893.9 kJ mol^{-1} respectively.⁴² Hence, upon interaction an equal sharing of an electron might reasonably be expected as observed with the B3LYP method. It is noted that their IE's, as calculated at the B3LYP/6-311G(2d,p) level, differ by 65.4 kJ mol^{-1} (Table 5.3). For the $\text{NO}^+ \cdots$ ring carbon distances $r(\text{N} \cdots \text{C}_1)$ and $r(\text{N} \cdots \text{C}_2)$, the MP2 (2.400 and 2.455 Å) and B3LYP (2.446 and 2.533 Å) methods are in reasonable agreement, and the B3LYP method predicts moderately longer interactions (0.046 and 0.078 Å). It should be noted that previous computational studies on this complex^{28,31-33} have reported $r(\text{N} \cdots \text{C}_1)$ distances of 2.44 – 2.46 Å, in agreement with our DFT results. In addition, other studies on

cation $\cdots\pi$ interactions have reported that the B3LYP method overestimates this interaction distance in comparison to the MP2 method.^{43,44} Importantly, however, both methods predict the same overall general structural features with the ON \cdots C₁ interaction being the shorter of the two by 0.055 Å (MP2) and 0.087 Å (B3LYP).

Table 5.2. Optimized N—O Bond Distances (Å) for Nitric Oxide and its Mono-ions Obtained Using the B3LYP and MP2 Methods in Combination with a Range of Basis Sets

Level of Theory		<i>r</i> (N—O)		
Method	Basis Set	NO ⁺	NO	NO ⁻
B3LYP	6-311G(d,p)	1.060	1.148	1.273
	6-311+G(d,p)	1.060	1.148	1.264
	6-311++G(d,p)	1.060	1.148	1.264
	6-311G(df,p)	1.058	1.147	1.271
	6-311G(2d,p)	1.058	1.148	1.273
	6-311+G(2df,p)	1.057	1.146	1.262
	aug-cc-pVDZ	1.068	1.154	1.266
	aug-cc-pVTZ	1.057	1.146	1.259
MP2	aug-cc-pVDZ	1.096	1.142	1.276
	aug-cc-pVTZ	1.082	1.137	1.265
Exptl. ^a			1.150	

^aReference ⁴⁵.

A variety of basis sets were then used in conjunction with the B3LYP method (Table 5.1). As noted above, the B3LYP method with all basis sets gives shorter *r*(N—O) distances than obtained using the MP2 method while consistently overestimating the *r*(N \cdots C₁) and *r*(N \cdots C₂) distances. For example, with the smallest basis set used in this present study, 6-311G(d,p), *r*(N \cdots C₁) and *r*(N \cdots C₂) are 0.076 and 0.091 Å

longer, respectively, than obtained at the MP2/aug-cc-pVTZ level. Only minor changes of less than 0.01 Å are observed upon inclusion of diffuse or f-functions on heavy atoms, 6-311+G(d,p) or 6-311G(df,p), respectively, or upon addition of diffuse functions on the hydrogen atoms, 6-311++G(d,p). Slightly larger effects are observed upon inclusion of a second set of d-functions, 6-311G(2d,p), with modest shortenings in both N··C₁ and N··C₂ by 0.026 and 0.016 Å to 2.450 and 2.530 Å, respectively. In fact, the resulting bond lengths are now in close agreement with those obtained at the B3LYP/aug-cc-pVDZ level (Table 5.1). Combining these individual enhancements to give the 6-311+G(2df,p) basis set does not significantly improve $r(\text{N}\cdots\text{C}_1)$ (2.452 Å) or $r(\text{N}\cdots\text{C}_2)$ (2.534 Å) further.

Thus, for the B3LYP method the 6-311G(2d,p), 6-311+G(2df,p), and aug-cc-pVDZ basis sets appear to provide the most reliable overall geometries. While the latter does give slightly more accurate geometries, the differences are not significant. In addition, Pople basis sets are more computationally feasible for larger sandwich complexes. Hence, optimized geometries of all further complexes with NO⁺ were obtained at the B3LYP/6-311G(2d,p) level of theory.

Complexation energies (ΔE_{corr}) for [C₆H₆···NO]⁺ were also determined at each level of theory employed (Table 5.1). Compared to that obtained at the MP2/aug-cc-pVTZ level (158.7 kJ mol⁻¹), for all basis sets presently used B3LYP consistently overestimates ΔE_{corr} by 27.8 – 35.9 kJ mol⁻¹ with the B3LYP/6-311+G(2df,p) level giving the closest agreement (186.5 kJ mol⁻¹). Thus, ΔE_{corr} for all further complexes involving NO⁺ was obtained by performing single point energy calculations at this level of theory using B3LYP/6-311G(2d,p) optimized geometries, i.e., B3LYP/6-311+G(2df,p)//B3LYP/6-311G(2d,p) (Table 5.1). Indeed, we note that this approach gives the ΔE_{corr} of [C₆H₆···NO]⁺ to be 186.3 kJ mol⁻¹ (Table 5.3).

Table 5.3. Calculated^a Adiabatic Ionization Energies (IE's) for NO, C₆H₆, and R-Groups^b of the Aromatic Amino Acids and Corrected Complexation Energies (kJ mol⁻¹) for the Ar...NO^{+/-} and Ar...NO^{+/-}...Ar Complexes

Species	IE	Complexation Energy			
		Ar...NO ⁺	Ar...NO ⁺ ...Ar	Ar...NO ⁻	Ar...NO ⁻ ...Ar
NO	931.5	–	–	–	–
C ₆ H ₆	866.1	186.3	219.2	24.1	49.5
Phe	822.3	205.6	243.5	25.6	59.0
Tyr	754.8	223.1	265.6	95.4	164.7
His	781.9	263.7	335.9	98.9	173.7
Trp	696.6	263.4	313.6	85.2	152.3

^aB3LYP/6-311G(2d,p) + ZPVE. ^bSee Figure 1.

C₆H₆...NO⁻ Complexes. In the interaction of NO⁻ with C₆H₆, no anion...π complexes were obtained; instead it only binds by forming hydrogen bonds. Several complexes are possible depending on whether one or two hydrogens of C₆H₆ are involved and the relative orientation of the NO⁻ moiety. At all levels of theory used in this study, the lowest energy complex (**2B**) corresponds to NO⁻ binding side-on to C₆H₆ via two hydrogens (Figure 5.2). Selected optimized distances obtained using the MP2 and B3LYP methods with a variety of basis sets are listed in Table 5.4.

Several differences can be seen upon comparing the optimized structures of **2B** obtained using both the MP2 and B3LYP methods with the aug-cc-pVTZ basis set. In particular, MP2 does not predict a shortening of the N—O bond upon complexation, whereas with B3LYP it shortens by 0.018 Å to 1.241 Å. While both methods predict similar structural characteristics with the N...H₁C hydrogen bond being shorter than the O...H₂C hydrogen bond, for MP2 *r*(N...H₁C) is only 0.040 Å shorter, whereas for B3LYP it is less by 0.168 Å. More importantly perhaps, the B3LYP method predicts

both interactions to be significantly longer by 0.149 and 0.277 Å, respectively, than obtained at the corresponding MP2 level.

Table 5.4. Selected Optimized Distances (Å) and Complexation Energy (kJ mol⁻¹) Obtained at Various Levels of Theory for the NO⁻ Bound Side-On C₆H₆⋯NO⁻ Complex
2B

Level of Theory		$r(\text{N}-\text{O})$	$r(\text{N}\cdots\text{H}_1)$	$r(\text{O}\cdots\text{H}_2)$	ΔE_{corr}
Method	Basis Set				
B3LYP	6-311G(d,p)	1.260	2.275	2.254	48.4
	6-311+G(d,p)	1.260	2.379	2.372	29.3
	6-311++G(d,p)	1.259	2.377	2.383	24.7
	6-311G(df,p)	1.258	2.276	2.262	37.4
	6-311G(2d,p)	1.261	2.278	2.263	37.4
	6-311+G(2df,p)	1.257	2.347	2.427	32.1
	aug-cc-pVDZ	1.261	2.309	2.468	21.9
	aug-cc-pVTZ	1.241	2.417	2.585	17.4
MP2	aug-cc-pVDZ	1.276	2.251	2.366	36.9
	aug-cc-pVTZ	1.265	2.268	2.308	25.2

Interestingly, when Pople rather than Dunning basis sets are used in combination with the B3LYP method, the results are in closer agreement with those obtained at the MP2/aug-cc-pVTZ level. In particular, when diffuse functions are *not included* in the basis set, i.e., 6-311G(d,p), 6-311G(df,p), and 6-311G(2d,p), the N⋯H₁C hydrogen bond distances are 2.275-2.278 Å, i.e., just slightly longer by 0.007-0.010 Å. Furthermore, these basis sets also give the second hydrogen bond lengths, $r(\text{O}\cdots\text{H}_2\text{C})$, to be only 0.045-0.054 Å shorter than at the MP2/aug-cc-pVTZ level. In addition, the N—O bond shortens upon complexation by 0.012-0.013 Å. In contrast, the B3LYP method in combination with Pople basis sets that *do include* diffuse functions, i.e., 6-

311+G(d,p), 6-311++G(d,p), and 6-311+G(2df,p), predicts lengths of both the N \cdots H₁C and O \cdots H₂C hydrogen bonds to be markedly longer than obtained at the MP2/aug-cc-pVTZ level by 0.079-0.111 and 0.064-0.119 Å, respectively. Reflecting the now weaker interaction between NO⁻ and C₆H₆, the N—O bond is concomitantly predicted to shorten by just 0.004-0.005 Å upon complexation. It is generally thought that diffuse functions should improve the accuracy of anionic structures. In this case, however, it appears that the inclusion of such functions causes an erroneous overestimation of such long, weak intermolecular interactions by the B3LYP method.

Table 5.5. Selected Optimized Distances (Å) and Complexation Energies (kJ mol⁻¹) Obtained at Various Levels of Theory for the NO⁻ Bound N-End-On C₆H₆ \cdots NO⁻ Complex

Level of Theory		<i>r</i> (N—O)	<i>r</i> (N \cdots H ₁)	ΔE_{corr}
Method	Basis Set			
B3LYP	6-311G(d,p) ^a	1.243	2.366	37.3
	6-311+G(d,p) ^a	1.250	2.490	31.2
	6-311++G(d,p) ^a	1.249	2.493	27.6
	6-311G(df,p) ^a	1.241	2.365	37.4
	6-311G(2d,p) ^a	1.243	2.367	36.1
	6-311+G(2df,p) ^a	1.247	2.497	26.5
	aug-cc-pVDZ ^b	1.252	2.100	15.7
	aug-cc-pVTZ ^b	1.232	2.256	13.8
MP2	aug-cc-pVDZ ^a	1.271	2.409	33.1
	aug-cc-pVTZ ^a	1.260	2.396	21.3

^aOptimized as **2C** in Figure 2. ^bOptimized as **2D** in Figure 2.

An alternative C₆H₆ \cdots NO⁻ complex with NO⁻ bound end-on via its nitrogen to C₆H₆ was found to lie just a few kJ mol⁻¹ higher in energy at all levels of theory.

Selected optimized distances for the resulting C_{2v} symmetric complexes **2C** and **2D** (Figure 5.2) are listed in Table 5.5. At the MP2/aug-cc-pVTZ level, the NO⁻ binds via two hydrogen bonds (**2C**) of length 2.396 Å and now has an N—O bond length of 1.260 Å. In contrast, at the corresponding B3LYP/aug-cc-pVTZ level, NO⁻ binds via a single (**2D**) considerably shorter (2.256 Å) hydrogen bond and has a shorter N—O bond of length 1.232 Å. We note that **2D** was only obtained when using Dunning basis sets used in combination with the B3LYP method. Analogous to that observed for **2B**, when Pople basis sets are used, there is a marked geometric sensitivity to the inclusion of diffuse functions on heavy atoms. As can be seen in Table 5.5, those that *do not include* such functions give optimized $r(\text{N}\cdots\text{H}_1)$ values in the narrow range 2.365–2.367 Å and just 0.03 Å shorter than obtained at the MP2/aug-cc-pVTZ level. In contrast, those that *do include* such functions give $r(\text{N}\cdots\text{H}_1)$ values that are decidedly longer by 0.094–0.101 Å, in the range of 2.490–2.497 Å.

Considering the results obtained for both side-on and end-on C₆H₆⋯NO⁻ complexes, the B3LYP/6-311G(2d,p) level of theory was chosen to obtain all further optimized structures for complexes involving NO⁻. As can be seen from Tables 5.4 and 5.5, the calculated complexation energies (ΔE_{corr}) for **2B** and **2C** are particularly sensitive to the inclusion of diffuse functions on *both* heavy and hydrogen atoms with decreases of 6.1–23.7 kJ mol⁻¹ upon their inclusion. However, ΔE_{corr} for the anionic complex **2B** is also sensitive to a set of f- or second set of d-functions on heavy atoms with observed decreases in ΔE_{corr} of 11.0 kJ mol⁻¹ for both upon their inclusion (Table 5.4). Thus, for all further anionic complexes ΔE_{corr} was obtained by performing single point calculations at the B3LYP/6-311++G(2df,p)//B3LYP/6-311G(2d,p) level of theory. Indeed, we note that at this level of theory the complexation energy for **2B** is 24.1 kJ mol⁻¹ (Table 5.3), in close agreement with that obtained at the MP2/aug-cc-pVTZ level.

5.3.2 $\text{Ar}\cdots\text{NO}^+$ Complexes

The aromatic R-groups (Ar) of the amino acids phenylalanine (Phe), tyrosine (Tyr), histidine (His), and tryptophan (Trp), Figure 5.1, were then allowed to interact with NO^+ in order to investigate the resulting structures and complexation energies. Unless noted, only the lowest energy complex for each is described with optimized structures and selected distances shown in Figure 5.3.

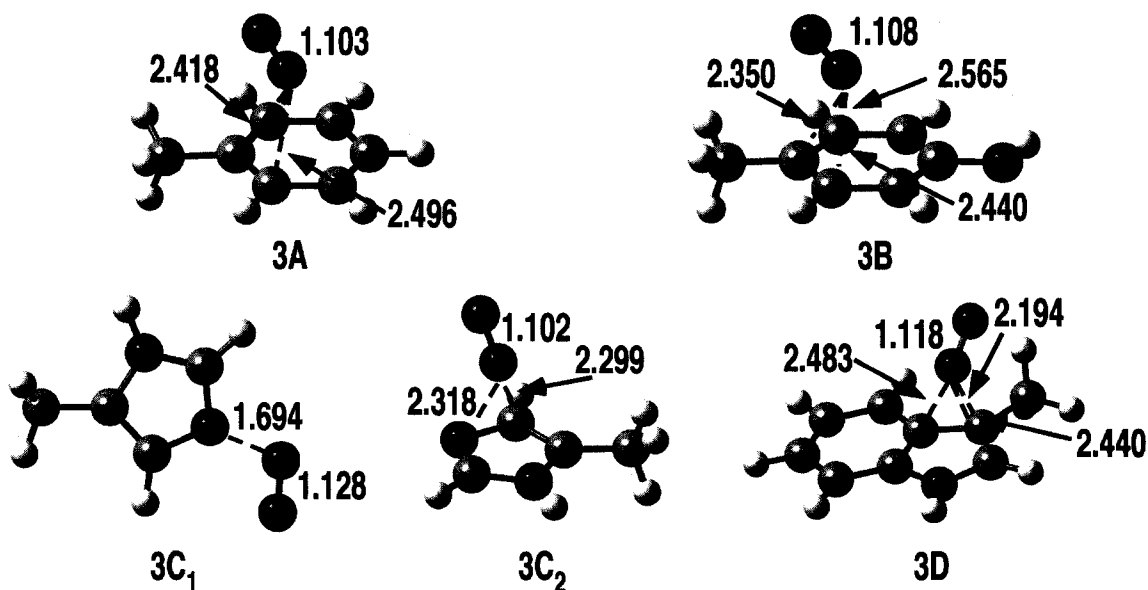


Figure 5.3. Optimized structures (B3LYP/6-311G(2d,p)) with selected distances (Å) for the $\text{Ar}\cdots\text{NO}^+$ complexes where Ar is (3A) Phe, (3B) Tyr, (3C₁) His with NO^+ bound via a ring nitrogen's lone pair, (3C₂) His with NO^+ bound via its π -system, and (3D) Trp. [C (gray); N (blue); O (red); H (white)].

$\text{Phe}\cdots\text{NO}^+$. Similar to that for C_6H_6 , the resulting complex (3A) is C_s symmetric. The NO^+ moiety is centered over the alkylated end of the ring with its oxygen directed up and out from the ring face along the $\text{C}-\text{CH}_3$ bond, in agreement with previous observations.³¹ The alkylated ring carbon is the most negatively charged in neutral toluene (Figure C.1 in Appendix C), our model for Phe. Furthermore, it will provide the

greatest stabilization of any positive charge build-up on the ring upon complexation. The N—O distance in **3A** is 1.103 Å, 0.045 Å longer than obtained for isolated NO⁺ at the same level of theory (cf. Table 2), and again indicating only partial electron transfer from the aromatic group upon complexation. It is also slightly longer than observed in C₆H₆···NO⁺, in agreement with the fact that the IE of Phe is lower than that of C₆H₆ (Table 5.3). As a result, NO⁺ binds more strongly to Phe than C₆H₆ as illustrated by the shorter ON···C1 (2.418 Å) and ON···C2 (2.496 Å) distances respectively, and the modestly larger complexation energy of 205.6 kJ mol⁻¹ (Table 5.3).

Tyr···NO⁺. The resulting lowest energy complex (**3B**) is similar to that with Phe (**3A**), in that NO⁺ preferentially binds nearly centered over the alkylated end of the ring face with its oxygen directed up and away from the face almost parallel to the C—CH₃ bond. Interestingly, this is despite the fact that tyrosine contains an —OH group. Indeed, a complex was found in which the NO⁺ sits atop, almost parallel with the C—OH bond with its nitrogen over the —OH oxygen. However, such a complex is found to, in fact, lie 33.0 kJ mol⁻¹ higher in energy (Table C.1). The IE of Tyr is calculated to be 67.5 kJ mol⁻¹ lower than that of Phe (Table 5.3). Consequently, *r*(N—O) is now slightly longer than observed for **3A** while conversely the ON···C1 (2.350 Å) and ON···C2 (2.440 Å) interactions are now shorter by 0.068 and 0.056 Å, respectively. We note that the ON···C2' distance (2.565 Å) is longer, due to the fact that the NO⁺ is slightly off center. In addition, the complexation energy for **3B** is also 17.5 kJ mol⁻¹ larger at 223.1 kJ mol⁻¹ (Table 5.3).

His···NO⁺. Histidine is an electron poor π-system due to the two nitrogens within the ring, one of which (denoted as N₁) has a free electron lone-pair in the plane of the ring. Indeed, in the lowest energy complex formed (**3C₁**) NO⁺ binds via its nitrogen center with this lone-pair resulting in a quite strong N1···NO⁺ interaction of 1.694 Å. Also,

$r(\text{N—O})$ itself has lengthened considerably to 1.128 Å, indicative of significant electron transfer from His to the NO⁺ moiety. In contrast, the π -bound complex **3C₂** lies 49.6 kJ mol⁻¹ higher in energy (Table C.1), with the NO⁺ moiety sitting 2.3 Å above the ring face with an N—O bond length of 1.102 Å, i.e., less electron transfer from His. The preference for the N1-bound complex is in agreement with previous observations on pyridine \cdots NO⁺ interactions.^{28,32} The complexation energy of **3C₁** is 263.7 kJ mol⁻¹ (Table 5.3), the largest of all Ar \cdots NO⁺ complexes considered in this study. While the IE of the aromatic group of histidine is lower (Table 5.3) than that of C₆H₆ and Phe, but higher than that of Tyr, it should be noted that it corresponds to ionization from its π -system. Indeed, **3C₂** has a lower complexation energy than **3B** as predicted.

Trp \cdots NO⁺. NO⁺ preferentially interacts via the alkylated carbon (C₁) of the pyrrole ring with an N \cdots C₁ distance of 2.194 Å to give the π -bound complex **3D**. In addition, its own N—O bond has lengthened by 0.060 Å to 1.118 Å. The former distance is the shortest interaction observed for any of the π -complexes considered in this present study, while the latter is the largest lengthening observed upon complexation. This is due to the fact that the tryptophan's aromatic group has the lowest IE of all aromatic groups considered; thus, there is greater electron transfer to the NO⁺ moiety, which is now also bound more tightly. Indeed, the complexation energy for **3D** is 263.4 kJ mol⁻¹ (Table 5.3), the highest of all of the π -bound complexes considered and only 0.3 kJ mol⁻¹ lower than that of the N1-bound histidine \cdots NO⁺ complex **5D₁**. An alternate complex lying only 10.0 kJ mol⁻¹ higher in energy was found in which the NO⁺ was bound via the π -system of the six-membered ring of the Trp aromatic group (not shown). This is in contrast to previous studies^{46,47} that found such a π -bound complex to in fact be preferred. We note, however, that these prior studies modeled the peptide backbone simply by using hydrogen. Thus, charge stabilization by the C1 center of tryptophan's aromatic group may have been underestimated.

5.3.3 $\text{Ar}\cdots\text{NO}^-$ Complexes

Optimized structures for the $\text{Ar}\cdots\text{NO}^-$ ($\text{Ar}=\text{Phe}$, Tyr , His , Trp) complexes with selected distances obtained at the B3LYP/6-311G(2d,p) level are shown in Figure 5.4.

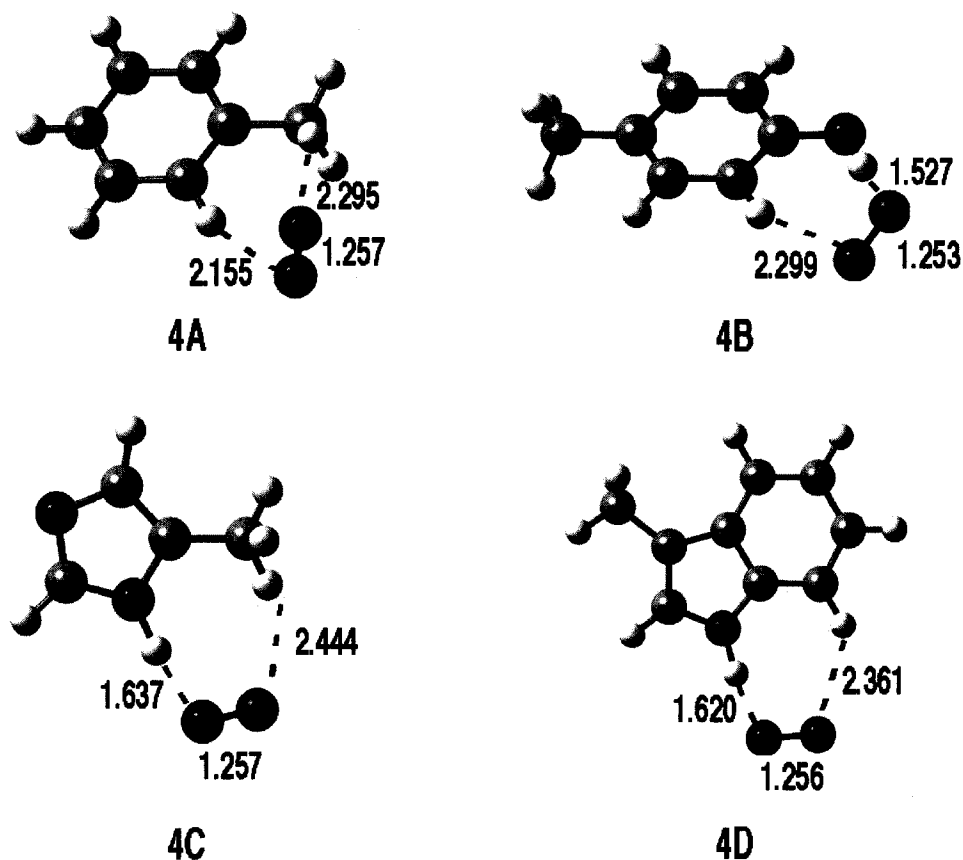


Figure 5.4. Optimized structures (B3LYP/6-311G(2d,p)) with selected distances (Å) for the lowest energy $\text{Ar}\cdots\text{NO}^-$ complexes where Ar is (4A) Phe, (4B) Tyr, (4C) His and (4D) Trp. [C (gray); N (blue); O (red); H (white)].

Unlike the cationic complexes, all of the lowest energy $\text{Ar}\cdots\text{NO}^-$ complexes exhibit similar intramolecular binding. Specifically, NO^- forms two hydrogen bonds with each aromatic species; its nitrogen binds via the strongest donor while its oxygen binds via the next best "spatially available" donor. For example, in the $\text{Phe}\cdots\text{NO}^-$ complex (4A) the NO^- nitrogen binds (2.295 Å) via a hydrogen of the $-\text{CH}_3$ group,

while the oxygen forms a shorter hydrogen bond (2.155 Å) with the adjacent ring C2–H moiety. In addition, the N–O bond itself has now shortened by 0.016 Å to 1.257 Å (cf. Table 5.2). The calculated complexation energy for **4A** is 25.6 kJ mol⁻¹, just 2.4 kJ mol⁻¹ larger than calculated for the C₆H₆⋯NO⁻ complex **2B**. For the corresponding complex with tyrosine (**4B**), the NO⁻ nitrogen forms quite a short and strong hydrogen bond (1.527 Å) with the tyrosyl's –OH group. Concomitantly, the NO⁻ oxygen forms a considerably weaker and longer bond (2.299 Å) with a nearby ring C–H group (Figure 5.4). The N–O bond itself has also shortened slightly to 1.253 Å. Because of the greater hydrogen bond donor capabilities of tyrosine's –OH group, the complexation energy for **4B** is 95.4 kJ mol⁻¹, almost 4 times greater than that for the analogous complexes with C₆H₆ and Phe (Table 5.3).

Similar to that described for the Tyr⋯NO⁻ complex, upon interacting with histidine, the NO⁻ nitrogen forms a short, strong bond with its best hydrogen bond donor, the ring –NH– group. It is noted that in the resulting complex **4C** this bond is now longer (1.637 Å) than the analogous bond in **4B** (Figure 5.4). Similarly, the NO⁻ oxygen forms a weaker, longer hydrogen bond (2.444 Å) with a hydrogen of the nearby –CH₃ group. Despite these longer distances, however, the complexation energy for **4C** is slightly higher than that of **4B** at 98.9 kJ mol⁻¹ (Table 5.3). Similarly, with the aromatic group of tryptophan the NO⁻ nitrogen forms a short hydrogen bond (1.620 Å) with its –NH– group (**4D**) while its oxygen forms a longer hydrogen bond with a nearby ring –CH– hydrogen. We note that at the present level of theory the NO⁻ oxygen prefers to interact with a –CH– group of the six-membered ring of the tryptophan's aromatic group with an O⋯HC distance of 2.592 Å. However, the alternate complex in which it interacts instead with a –CH– hydrogen of the five-membered ring lies just 1.5 kJ mol⁻¹ higher in energy. The complexation energy of **4D** is 85.2 kJ mol⁻¹, 13.7 kJ mol⁻¹ lower than for **4C** (Table 5.3).

5.3.4 [Ar...NO...Ar]⁺ Complexes

After the studies on the "half-sandwiches", we then considered "full-sandwich" complexes, specifically those in which both aromatic species are the same. Optimized structures and selected bond distances obtained at the B3LYP/6-311G(2d,p) level are shown in Figure 5.5. For simplicity, except for histidine, only the lowest energy complex is shown.

Interestingly, the cationic sandwich complexes do not correspond to a simple "doubling" of the half-sandwiches. For example, in **5A** the two C₆H₆ rings bind to opposite sides of the NO⁺ with one tilted markedly toward the other perpendicular to the NO bond, coming closest to each other at the nitrogen end of NO⁺ (Figure 5.5). As a result, the NO⁺ does not sit directly between the two rings nor is its distance to both rings equal. With respect to the more closely bound C₆H₆, the NO⁺ sits in the same position and orientation as observed in the corresponding half-sandwich **2A**: centered over one end of the ring with its oxygen directed up and outward from the face. The distance from the NO⁺ nitrogen to the nearest ring carbon (C_{ring}) is 2.588 Å. In contrast, the second C₆H₆ is orientated such that the NO⁺ effectively sits above its face, with its closest C_{ring}...NO distance being significantly longer at 2.786 Å. While both of these C_{ring}...N distances are notably longer than in **2A** (cf. Table 5.1) their combined effects result in *r*(N—O) of **5A** being equal to that in **2A**, indicating a similar overall extent of electron transfer to the NO⁺ moiety (cf. Table 5.2). From Figure 5.6 it can be seen that the HOMO of **5A** (**5A**_{HOMO}) corresponds to the two C₆H₆ rings interacting with the same antibonding π-orbital on NO⁺, one from above and the other below, in particular via its nitrogen.

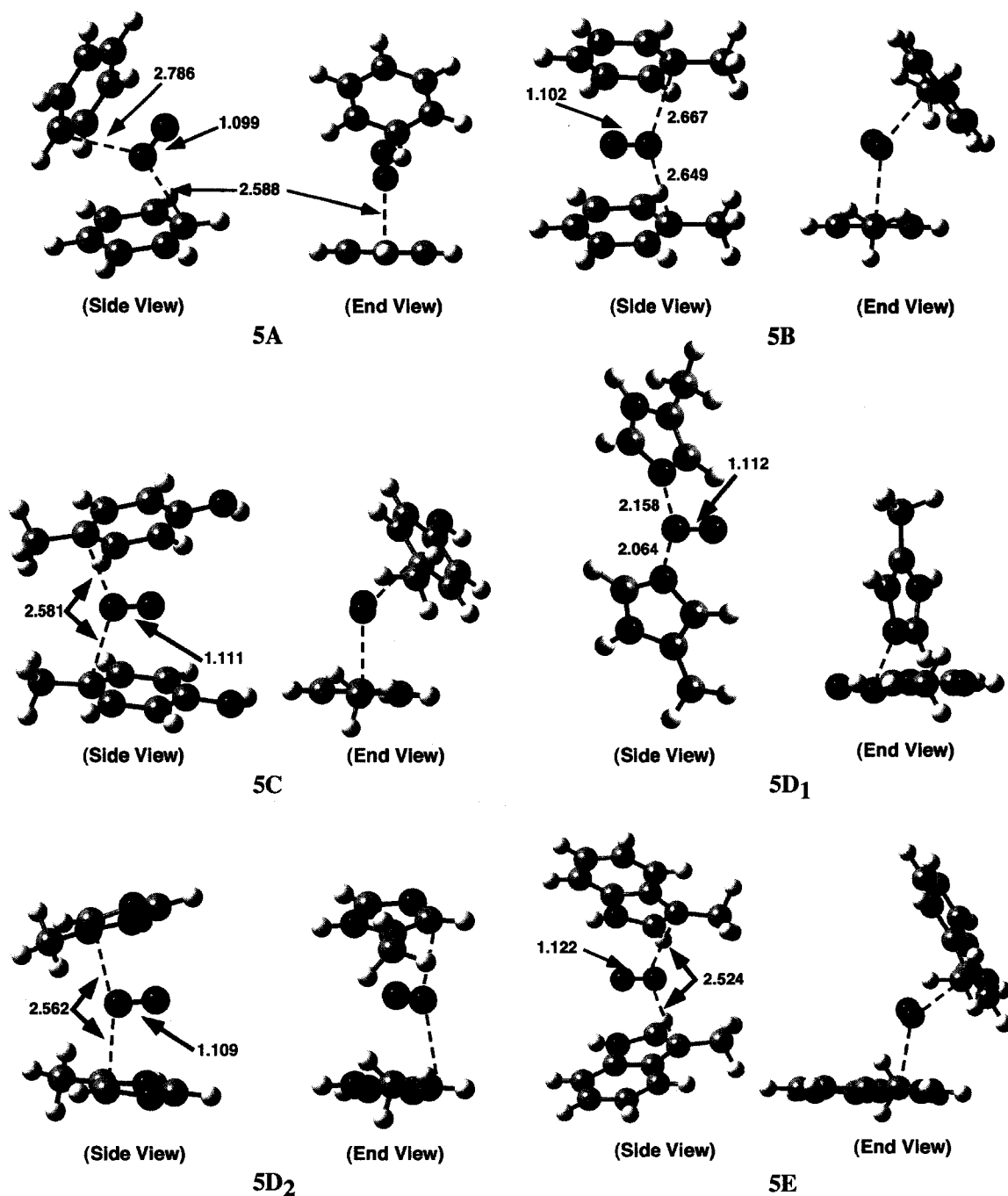


Figure 5.5. Optimized structures (B3LYP/6-311G(2d,p)) with selected distances (Å) of the $[\text{Ar}\cdots\text{NO}\cdots\text{Ar}]^+$ complexes where Ar is (5A) C_6H_6 , (5B) Phe, (5C) Tyr, (5D₁) His when bound via both ring nitrogens' lone-pairs, (5D₂) His when bound via both rings π -systems, and (5E) Trp. [C (gray); N (blue); O (red); H (white)].

The Phe (**5B**) and Tyr (**5C**) sandwiches, while possessing some similarities to their respective parent half-sandwiches **3A** and **3B** and the analogous C₆H₆-sandwich **5A**, exhibit a number of important differences. In both complexes the closest interactions again occur between the NO⁺ nitrogen and the alkylated ring carbons (C1) of each aromatic species with the distances to the tyrosine rings again being shorter than to the phenylalanine rings. In **5B**, these distances are again unequal although now they differ by just 0.018 Å (Figure 5.5). In contrast, in **5C** the NO⁺ sits equidistant from both rings with C1...NO distances of 2.581 Å. Significantly, however, in both complexes the NO⁺ moiety is now directed back over the faces of the rings involved rather than outward as in the corresponding half-sandwiches **3A** and **3B**, respectively (Figure 5.5). In addition, while the two rings in **5B** and **5C** are again tilted with respect to each other, the tilt axis is now essentially along the NO bond. As illustrated by the HOMO of the [Phe...NO...Phe]⁺ sandwich (**5B_{HOMO}**), shown in Figure 5.6, this results in both rings now interacting with the *same* side of the antibonding π-orbital on NO⁺. We note that as for **5A** and **2A**, despite the individually weaker C1...NO interactions in **5B** and **5C**, the N—O lengths are in close agreement with those of their related half-sandwiches **3A** and **3B**, respectively.

When the aromatic group of a second histidine (His_b) is allowed to interact with the lowest energy His_a...NO⁺ complex **3C₁**, it also preferentially binds with the nitrogen of the NO⁺ moiety via the lone-pair of its N1 center to give complex **5D₁** (Figure 5.5). However, the His_b group sits almost perpendicular to the plane of the initial His_a...NO⁺ moiety with a significantly longer (0.094 Å) N1...NO⁺ distance than for the His_a ring. An alternate C_s symmetric sandwich-type complex (**5D₂**) was also obtained, in which the NO⁺ moiety is positioned over the -CHN1CH- component of each ring, its nitrogen being 2.562 Å from the ring carbons adjacent to the alkylated carbons (Figure 5.5). However, such a complex lies significantly higher in energy than **5D₁** by 73.4 kJ mol⁻¹.

It should be noted that despite the structural differences between **5D₂** and **5B/5C**, it possesses a similar HOMO with regards to orientation and mode of interaction between the aromatic rings and NO⁺ (Figure C.2).

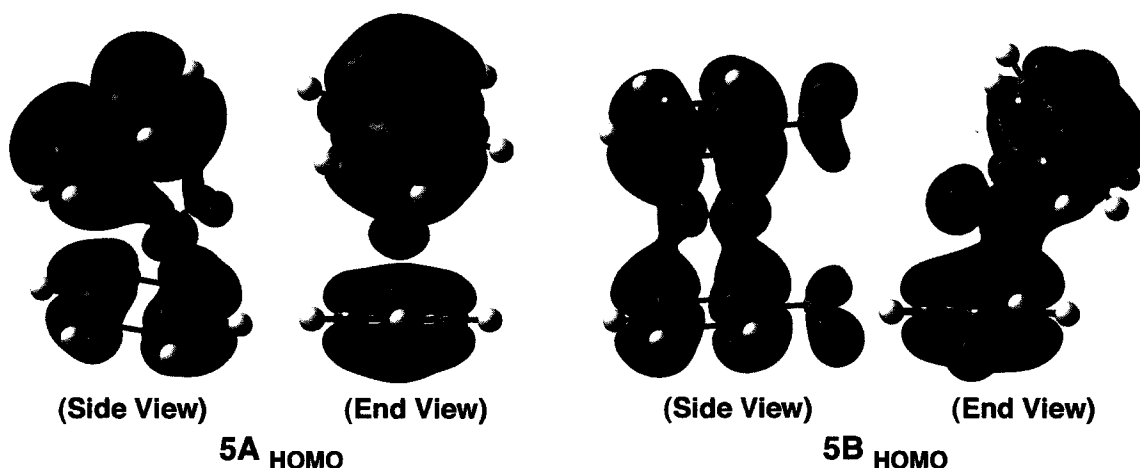


Figure 5.6. The highest occupied molecular orbital (HOMO) for the optimized structures of the Ar...NO⁺...Ar sandwich complexes where Ar is (**5A_{HOMO}**) C₆H₆ and (**5B_{HOMO}**) Phe. [C (gray); N (blue); O (red); H (white)].

For the aromatic group of tryptophan, the lowest energy sandwich (**5E**) corresponds to NO⁺ interacting equally with both pyrrole rings, its closest contact being the ON...C1 (alkylated carbon) distance at 2.524 Å (Figure 5.5). Similar to that observed for sandwiches **5B** and **5C** formed by the aromatic groups of Phe and Tyr, respectively, the NO⁺ is directed back over the faces of the pyrrole rings. Furthermore, the tryptophan rings are also tilted with respect to each other such that they interact with the same lobes of a π -antibonding orbital of NO⁺ (Figure C.2). Similarly, as for all other Ar...NO⁺...Ar complexes considered (see Figure 5.5), the N—O bond lengthens upon complexing with two aromatic species. However, as for the half-sandwiches, only partial charge transfer occurs (see Table C.1) as illustrated by the fact that its length now lies

between that of NO⁺ and NO[•] as calculated at the same level of theory (Table 5.2). The degree of charge transfer is dependent on the IE of the aromatic species involved.

The complexation energies (ΔE_{corr}) for the sandwich complexes of NO⁺ with C₆H₆ (**5A**) and the aromatic groups of Phe (**5B**), Tyr (**5C**), and Trp (**5E**) are 219.2, 243.5, 265.6, and 313.6 kJ mol⁻¹ respectively (Table 5.3). Comparison with ΔE_{corr} of the half-sandwiches indicates that addition of a second appropriate aromatic group is increasingly favored by 32.9, 38.0, 42.4 and 50.2 kJ mol⁻¹. Thus, NO⁺ prefers to form sandwiches with the side group of tryptophan compared to those of tyrosine and phenylalanine, with tyrosine being slightly preferred of these latter two. For the side group of histidine, the preferred complex **5D₁** has the highest ΔE_{corr} at 335.9 kJ mol⁻¹, but is not a sandwich-type complex. The corresponding sandwich **5D₂** has a much lower complexation energy of 262.5 kJ mol⁻¹ (Table C.1), which in fact is also slightly lower than that of **5C**. It is noted that while in proteins the histidine side group is often protonated due to its pK_a being near 6, many metalloproteins use multiple unprotonated histidines to bind metal ions. Thus, the above results suggest that NO⁺ may in fact also be able to bind in such areas.

5.3.5 [Ar...NO...Ar]⁻ Complexes

Optimized structures for the anionic complexes with selected bond distances obtained at the B3LYP/6-311G(2d,p) level are shown in Figure 5.7. Unlike the cationic complexes, the lowest energy structure in all cases corresponds to a "doubling" of the parent half-complex, in that the NO⁻ nitrogen and oxygen interact with the *same* hydrogens of *both* aromatic species as in the appropriate parent. For example, when NO⁻ interacts with two phenylalanine aromatic groups (**7B**), its nitrogen again interacts with a -CH₃ hydrogen in each Phe group, while its oxygen interacts with a C—H adjacent to the alkylated carbon (C1) of each ring. All of the intermolecular interactions, however,

are now longer than in their corresponding half-complexes by 0.018–0.308 Å. The largest increase observed in any anionic complex, except that involving the aromatic group of tryptophan (**7E**), occurs in the $\text{ON}\cdots\text{HX}$ hydrogen bonds (Figure 5.7). It is noted that all of the resulting complexes except **7D**, involving the aromatic group of histidine, are symmetric at the present level of theory; i.e., the NO^- moiety sits equidistant from both aromatic species. In **7D** the NO^- is skewed slightly such that it forms a marginally shorter $\text{N-H}\cdots\text{NO}$ bond with one of the histidine groups and simultaneously has a slightly shorter $\text{NO}\cdots\text{H-C}$ bond with the other group. It is noted that no complexes involving $\text{NO}^- \cdots \pi$ interactions were obtained.

The calculated complexation energies (Table 5.3) for NO^- interacting with two benzenes (**7A**) or aromatic groups of the amino acids phenylalanine (**7B**), tyrosine (**7C**), histidine (**7D**), and tryptophan (**7E**) are 49.5, 59.0, 164.7, 173.7, and 152.3 kJ mol^{-1} , respectively. The overall order is the same as for the corresponding half-complexes. Clearly, there is a distinct preference by NO^- to form complexes with those groups that contain conventional hydrogen bond donors such as $-\text{OH}$ or N-H groups. Interestingly, **7A** and **7B**, which contain only $\text{C-H}\cdots(\text{NO})^-$ interactions, give complexation energies that are slightly more than double those of their half-complexes **2B** and **4A**, respectively (see Table 5.3). In contrast, all others contain more conventional $-\text{OH}\cdots\text{NO}$ or $\text{N-H}\cdots\text{NO}$ hydrogen bonds and have complexation energies that are less than double those of their respective parent half-complexes.

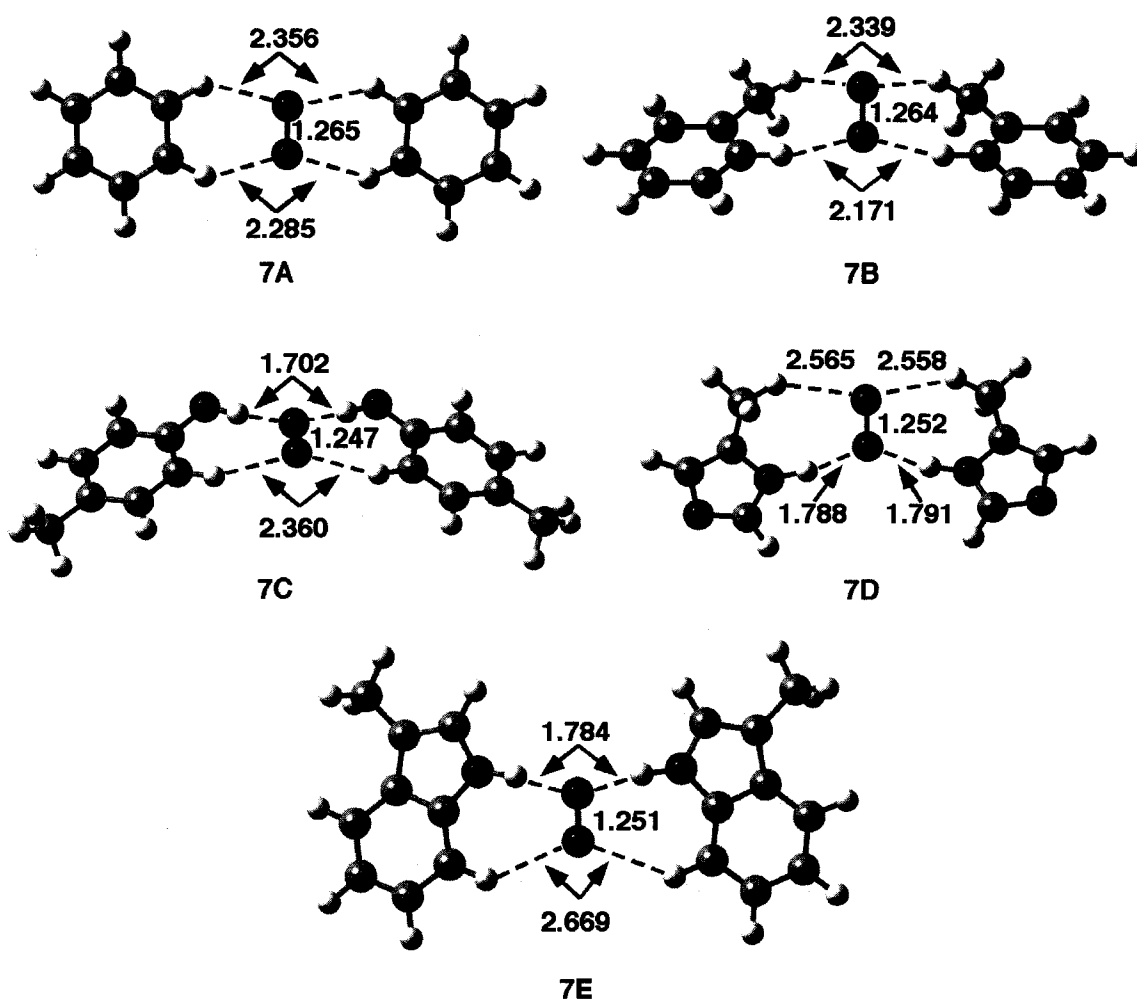


Figure 5.7. Optimized structures (B3LYP/6-311G(2d,p)) with selected distances (Å) of the $[\text{Ar}\cdots\text{NO}\cdots\text{Ar}]^-$ complexes where Ar is (7A) C_6H_6 , (7B) Phe, (7C) Tyr, (7D) His, and (7E) Trp. [C (gray); N (blue); O (red); H (white)].

5.4 Conclusions

Complexes formed by the interaction of NO^+ and NO^- with C_6H_6 (benzene) and the aromatic R-groups of the amino acids phenylalanine (Phe), tyrosine (Tyr), histidine (His), and tryptophan (Trp) have been investigated. In particular, both the half- ($\text{Ar}\cdots\text{NO}^{+/-}$) and full-sandwiches $\text{Ar}\cdots\text{NO}^{+/-}\cdots\text{Ar}$ (where the Ar groups are the same) were studied. In addition, the reliability and accuracy of the B3LYP method for

obtaining optimized structures and complexation energies for such complexes were also assessed by comparison with results obtained using the high-level *ab initio* method MP2/aug-cc-pVTZ.

In all Ar...NO⁺ complexes considered, NO⁺ binds via its nitrogen center. Furthermore, except for the aromatic group of histidine, it preferentially binds via their π -system centered toward one end of the ring with its oxygen directed up and outward from the ring face parallel, or almost, with a C—X bond (X = H, Ar = C₆H₆; X = CH₃, Ar = Phe, Tyr, Trp). In contrast to previous studies, NO⁺ is found to prefer to bind via the pyrrole ring of tryptophan's aromatic group. For Ar = His, the ON⁺... π complex lies 49.5 kJ mol⁻¹ higher in energy than when NO⁺ binds via the in-plane lone-pair of the histidine's ring nitrogen (N1). For the Ar...NO⁻ complexes considered, NO⁻ binds side-on to the aromatic species via two hydrogen bonds. The lowest energy complexes correspond to the NO⁻ nitrogen binding with the aromatic's best hydrogen bond donor while the oxygen binds to the next best "spatially available" donor.

The cationic π -sandwich complexes [Ar...NO...Ar]⁺ do not correspond to a "doubling" of their parent half-sandwiches. Except for Ar = C₆H₆, while the NO⁺ moiety again interacts via its nitrogen with the same ring atom as in the appropriate half-sandwich, it is now directed back over the face of the aromatic rings. Furthermore, for Ar = C₆H₆ and the aromatic group of phenylalanine, at the level of theory used in this present study NO⁺ binds more closely to one of the aromatic rings than the other, the difference decreasing from Ar = C₆H₆ to Phe. For Ar = His, the lowest energy cationic complex again corresponds to both rings binding via their lone-pairs of the N1 ring centres to the NO⁺ nitrogen, although the rings are now almost perpendicular to each other. In contrast, the anionic [Ar...NO...Ar]⁻ complexes are found to correspond to a

"doubling" of the parent Ar...NO⁻ complexes with the same hydrogen bond interactions being maintained.

The calculated complexation energies (ΔE_{corr} values) for those complexes involving NO⁺ binding via the π -systems of the aromatic species indicate that it has a clear preference for the aromatic group of tryptophan. Indeed, for both half- and full-sandwich type complexes this preference is in the order Trp >> Tyr > His > Phe > C₆H₆. For both types of complexes, those involving the Trp aromatic group are favored by around 40 kJ mol⁻¹. For the sandwich-type complexes, the difference between ΔE_{corr} for Tyr and His is quite small. The N1-bound His...NO⁺ and His...NO⁺...His complexes are both found to lie lower in energy than any of the π -bound complexes. Notably, however, the former is only quite marginally lower in energy than the Trp...NO⁺ complex. For the anionic complexes, the calculated ΔE_{corr} values indicate that NO⁻ strongly prefers those aromatic groups that contain conventional hydrogen bond donor groups such as -OH or -NH-. For both types of complexes the order of preference is His > Tyr > Trp >> Phe > C₆H₆.

References

- (1) Gibaldi, M. J. *Clin. Pharmacol.* **1993**, 33, 488.
- (2) Rosen, G. M.; Tsai, P.; Pou, S. *Chem. Rev.* **2002**, 102, 1191.
- (3) Koshland, D. E. *Science* **1992**, 258, 1861.
- (4) Janssen, L. J.; Premji, M.; Lu-Chao, H.; Cox, G.; Keshavjee, S. *Am. J. Physiol.: Lung Cell. Mol. Physiol.* **2000**, 278, 899.
- (5) Fukuto, J. M.; Switzer, C. H.; Miranda, K. M.; Wink, D. A. *Annu. Rev. Pharmacol. Toxicol.* **2005**, 45, 335.
- (6) Butler, A. R.; Flitney, F. W.; Williams, D. L. H. *Trends Pharmacol. Sci.* **1995**, 16, 18.

- (7) Shiva, S.; Crawford, J. H.; Ramachandran, A.; Ceaser, E. K.; Hillson, T.; Brookes, P. S.; Patel, R. P.; Darley-USmar, V. M. *Biochem. J.* **2004**, *379*, 359.
- (8) Broillet, M.-C. *Cell. Mol. Life Sci.* **1999**, *55*, 1036.
- (9) Al-Sa'doni, H.; Ferro, A. *Clin. Sci.* **2000**, *98*, 507.
- (10) Gaston, B. *Biochim. Biophys. Acta* **1999**, *1411*, 323.
- (11) Wang, K.; Zhang, W.; Xian, M.; Hou, Y.-C.; Chen, X.-C.; Cheng, J.-P.; Wang, P. G. *Curr. Med. Chem.* **2000**, *7*, 821.
- (12) Akhter, S.; Vignini, A.; Wen, Z.; English, A.; Wang, P. G.; Mutus, B. *Proc. Natl. Acad. Sci. USA* **2002**, *99*, 9172.
- (13) Meyer, E. A.; Castellano, R. K.; Diederich, F. *Angew. Chem. Int. Ed.* **2003**, *42*, 1210.
- (14) Ma, J. C.; Dougherty, D. A. *Chem. Rev.* **1997**, *97*, 1303.
- (15) Reddy, S. A.; Sastry, G. N. *J. Phys. Chem. A* **2005**, *109*, 8893.
- (16) Gallivan, J. P.; Dougherty, D. A. *Proc. Natl. Acad. Sci. USA* **1999**, *96*, 9459.
- (17) Liu, T.; Zhu, W.; Gu, J.; Shen, J.; Luo, X.; Chen, G.; Pua, C. M.; Silman, I.; Chen, K.; Sussman, J. L.; Jiang, H. *J. Phys. Chem. A* **2004**, *108*, 9400.
- (18) Waters, M. L. *Biopolymers* **2004**, *76*, 435.
- (19) Garau, C.; Frontera, A.; Quiñero, D.; Ballester, P.; Costa, A.; Deya, P. M. *Chem. Phys. Lett.* **2004**, *392*, 85.
- (20) Mascal, M.; Armstrong, A.; Bartberger, M. D. *J. Am. Chem. Soc.* **2002**, *124*, 6274.
- (21) Hartmann, M.; Wetmore, S. D.; Radom, L. *J. Phys. Chem. A* **2001**, *105*, 4470.
- (22) Chaney, J. D.; Goss, C. R.; Folting, K.; Santarsiero, B. D.; Hollingsworth, M. D. *J. Am. Chem. Soc.* **1996**, *118*, 9432.
- (23) Desiraju, G. R. *Acc. Chem. Res.* **1991**, *24*, 290.
- (24) Steiner, T.; Saenger, W. *J. Am. Chem. Soc.* **1992**, *114*, 10146.
- (25) Rosokha, S. V.; Kochi, J. K. *J. Am. Chem. Soc.* **2001**, *123*, 8985.
- (26) Rosokha, S. V.; Kochi, J. K. *J. Am. Chem. Soc.* **2002**, *124*, 5620.

- (27) Rosokha, S. V.; Lindeman, S. V.; Rathore, R.; Kochi, J. K. *J. Org. Chem.* **2003**, *68*, 3947.
- (28) Grabow, J. A. D.; Meyer, P. M. *Eur. J. Mass Spectrom.* **2004**, *10*, 899.
- (29) Zhao, Y.-L.; Bartberger, M. D.; Goto, K.; Shimada, K.; Kawashima, T.; Houk, K. N. *J. Am. Chem. Soc.* **2005**, *127*, 7964.
- (30) Gwaltney, S. R.; Rosokha, S. V.; Head-Gordon, M.; Kochi, J. K. *J. Am. Chem. Soc.* **2003**, *125*, 3273.
- (31) Skokov, S.; Wheeler, R. A. *J. Phys. Chem. A* **1999**, *103*, 4261.
- (32) Dechamps, N.; Gerbaux, P.; Flammang, R.; Bouchoux, G.; Nam, P. C.; Nguyen, M. T. *Int. J. Mass Spectrom.* **2004**, *232*, 31.
- (33) Chiavarino, B.; Crestoni, M. E.; Fornarini, S.; Lemaire, J.; Maitre, P.; MacAleese, L. *J. Am. Chem. Soc.* **2006**, *128*, 12553.
- (34) Frisch, M. J.; Trucks, G. W.; Schlegel, H. B.; Scuseria, G. E.; Robb, M. A.; Cheeseman, J. R.; Montgomery, J. A. J.; Vreven, T.; Kudin, K. N.; Burant, J. C.; Millam, J. M.; Iyengar, S. S.; Tomasi, J.; Barone, V.; Mennucci, B.; Cossi, M.; Scalmani, G.; Rega, N.; Petersson, G. A.; Nakatsuji, H.; Hada, M.; Ehara, M.; Toyota, K.; Fukuda, R.; Hasegawa, J.; Ishida, M.; Nakajima, T.; Honda, Y.; Kitao, O.; Nakai, H.; Klene, M.; Li, X.; Knox, J. E.; Hratchian, H. P.; Cross, J. B.; Adamo, C.; Jaramillo, J.; Gomperts, R.; Stratmann, R. E.; Yazyev, O.; Austin, A. J.; Cammi, R.; Pomelli, C.; Ochterski, J.; Ayala, P. Y.; Morokuma, K.; Voth, G. A.; Salvador, P.; Dannenberg, J. J.; Zakrzewski, V. G.; Dapprich, S.; Daniels, A. D.; Strain, M. C.; Farkas, O.; Malick, D. K.; Rabuck, A. D.; Raghavachari, K.; Foresman, J. B.; Ortiz, J. V.; Cui, Q.; Baboul, A. G.; Clifford, S.; Cioslowski, J.; Stefanov, B. B.; Liu, G.; Liashenko, A.; Piskorz, P.; Komaromi, I.; Martin, R. L.; Fox, D. J.; Keith, T. A.; Al-Laham, M. A.; Peng, C. Y.; Nanayakkara, A.; Challacombe, M.; Gill, P. M. W.; Johnson, B. G.; Chen, W.; Wong, M. W.; Gonzalez, C.; Pople, J. A. Gaussian 03; Gaussian Inc.: Wallingford CT, 2004.
- (35) Becke, A. D. *J. Chem. Phys.* **1993**, *98*, 1372.

- (36) Stephens, P. J.; Devlin, F. J.; Chabalowski, C. F.; Frisch, M. J. *J. Phys. Chem.* **1994**, *98*, 11623.
- (37) Lee, C.; Yang, W.; Parr, R. G. *Phys. Rev. B* **1988**, *37*, 785.
- (38) Seeger, R.; Pople, J. A. *J. Chem. Phys.* **1977**, *66*, 3045.
- (39) Bauernshmitt, R.; Ahlrichs, R. *J. Chem. Phys.* **1996**, *104*, 9047.
- (40) Boys, S. F.; Bernardi, F. *Mol. Phys.* **1970**, *19*, 553.
- (41) Simon, S.; Duran, M.; Dannenberg, J. J. *J. Chem. Phys.* **1996**, *105*, 11024.
- (42) Afeefy, H. Y.; Liebman, J. F.; Stein, S. E. Neutral Thermochemical Data. NIST Chemistry WebBook; NIST Standard Reference Database Number 69; National Institute of Standards and Technology: Gaithersburg MD, June 2005.
- (43) Felder, C.; Jiang, H. L.; Zhu, W. L.; Chen, K. X.; Silman, I.; Botti, S. A.; Sussman, J. L. *J. Phys. Chem. A* **2001**, *105*, 1326.
- (44) Liu, T.; Gu, J.; Tan, X. J.; Zhu, W. L.; Luo, X. M.; Jiang, H. L.; Ji, R. Y.; Chen, K. X.; Silman, I.; Sussman, J. L. *J. Phys. Chem. A* **2001**, *105*, 5431.
- (45) Kawanami, N.; Ozeki, T.; Yagasaki, A. *J. Am. Chem. Soc.* **2000**, *122*, 1239.
- (46) Basch, H.; Stevens, W. J. *J. Mol. Struct.: THEOCHEM* **1995**, *338*, 303.
- (47) Mecozzi, S.; West, A. P. J.; Dougherty, D. A. *Proc. Natl. Acad. Sci. USA* **1996**, *93*, 10566.

Chapter 6

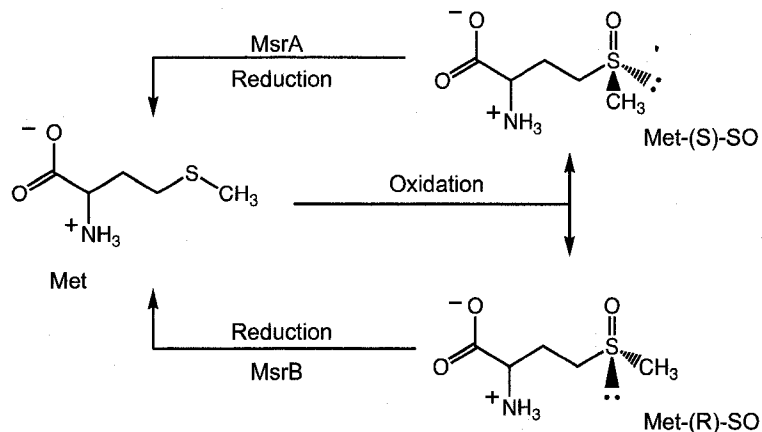
An Ongoing Investigation into the Mechanism of Methionine Sulfoxide Reductase B

6.1 Introduction

Reactive oxygen species (ROS) are produced in organisms during normal cellular activities, e.g., by-products of the electron transport chain or as a result non-enzymatic processes, such as exposure to UV radiation.^{1,2} ROS often target biomolecules, with oxidation of proteins being associated with a variety of age-related diseases, including cancer and Alzheimer's disease.¹⁻³ In order to protect against oxidative damage, cells have developed numerous defense mechanisms. In particular, some cellular proteins prevent oxidative damage to their functional components by utilizing residues in non-critical locations, such as on the protein's surface, as 'oxidation sinks'.^{4,5}

Methionine (Met) is often employed as this 'sacrificial lamb' since it is one of the most readily oxidized amino acids.¹⁻¹² The oxidation of Met results in the formation of methionine sulfoxide (MetSO), in both its S- and R- isoforms. Importantly, however, the oxidation of Met is reversible, with its reduction being catalyzed by two methionine sulfoxide reductase (Msr) enzymes, MsrA and MsrB, which exhibit specificity for the S- and R- isoforms, respectively (Scheme 6.1).¹²⁻¹⁴ Interestingly, these enzymes are not only imperative for antioxidant defense,³⁻¹² but they are also found to be involved in protein regulation^{3,7,9} and bacterial virulence.¹⁵

Scheme 6.1. Illustration of the methionine sulfoxide isomers produced via oxidation and the selectivity of the methionine sulfoxide reductase enzymes, MsrA and MsrB.¹⁶

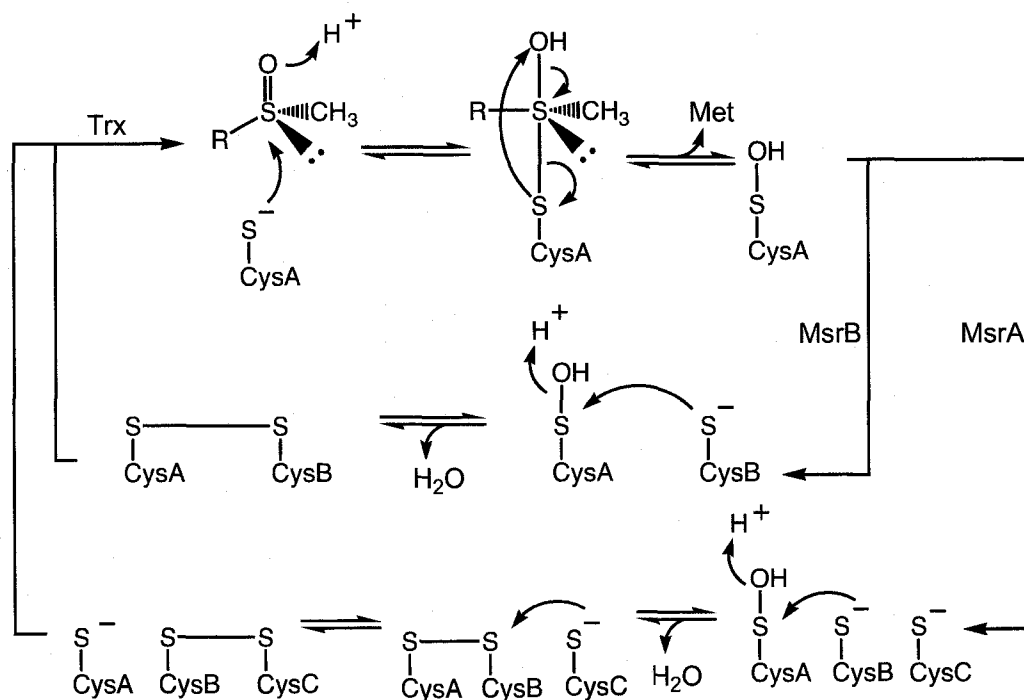


Although the Msr enzymes catalyze the same reaction, albeit on the different isomeric forms of the substrate, they do not share sequence homology and are structurally unrelated.^{17,18} However, both active sites contain a cysteine residue¹⁷⁻²² (selenocysteine in some mammalian MsrBs),²³ whose role is believed to be catalytic, as well as a tryptophan residue that is thought to aid in the orientation of the substrate within the active site.^{19,24,25} In addition, both active sites contain a region of hydrogen bond donors with which the oxygen of MetSO is believed to interact.^{19,25} However, the nature of the amino acids in the aforementioned area is quite different. The active site of MsrA contains two aromatic tyrosine residues and a single glutamate, while that of MsrB is rich in acid-base residues (two histidines and an arginine) and polar residues (threonine and asparagine).^{18,19} However, Lowther *et al.*¹⁹ noted that the active sites of MsrA and MsrB maintain a mirrored relationship, which may account for their specificity for substrates with opposing chirality.

Despite these differences within the active site, the reduction of MetSO, catalyzed by the two Msr's, is believed to occur via similar reaction mechanisms (Scheme 6.2).^{17,21,26} In the first step of the proposed mechanism, a catalytic cysteine (CysA) is

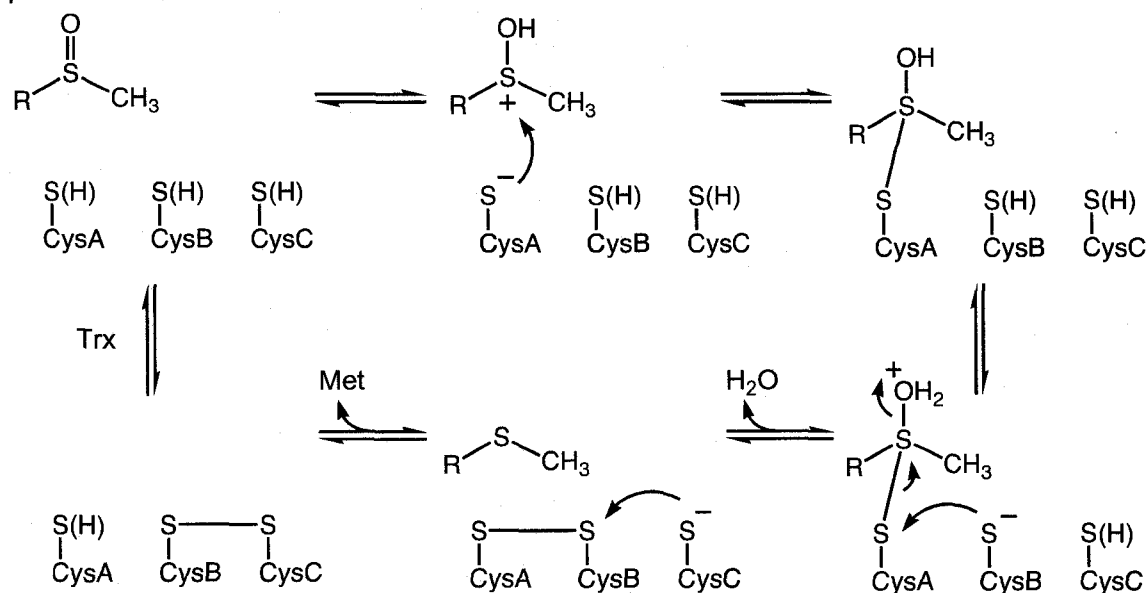
believed to nucleophilically attack the sulfur centre of MetSO, forming a sulfurane intermediate. This role for CysA is supported by studies that indicate that the mutation of this residue renders the enzyme completely inactive.^{20,22} In the proceeding step, the hydroxyl group is transferred to the sulfur centre of CysA, resulting in the formation of Met and sulfenic acid. Experimental evidence suggests the presence of such a sulfenic acid species in both reactions.^{17,21,27} In the ensuing steps, the active site of the enzyme is reduced; however, the details of these steps are dependent upon the enzyme used. In general, most MsrB's undergo a single thiol-disulfide exchange catalyzed by a 'recycling' cysteine (CysB), which results in the removal of the sulfenic acid as water, as well as the formation of a disulfide bond. While the MsrA's catalyze two such exchanges as indicated in Scheme 6.2. Thioredoxin (Trx) is then used to reduce the formed disulfide bonds in both enzymes to regenerate the fully reduced active site.

Scheme 6.2. Key steps of the proposed mechanism for the Msr enzymes in the reduction of MetSO via a sulfenic acid intermediate.^{17,21}



Interestingly, an earlier mechanism proposed by Lowther *et al.*²² for MsrA also suggested that the reaction may proceed via the formation of a sulfurane intermediate in a similar manner (Scheme 6.3). However, this intermediate undergoes protonation of its OH⁻ group of the sulfurane followed by a direct nucleophilic attack of the 'recycling' cysteine to yield a disulfide and water, ultimately leading to the regeneration of Met. This type of mechanism, however, would appear to favour an active site that is rich in acidic residues, such as that of MsrB.

Scheme 6.3. Proposed reaction mechanism for MetSO reduction via a second protonation and a direct thiol attack.²²



A recent theoretical study by Balta *et al.*,²⁸ relating to the mechanism of the Msr's, investigated the methane-thiol catalyzed reduction of dimethyl sulfoxide (DMSO) in the presence of a second DMSO molecule. Importantly, from their investigation, the collapse of a sulfurane intermediate was identified to proceed through the sulfonium intermediate. Cleavage of the disulfide bond in the latter intermediate was found to occur either through a sulfenic acid intermediate or through the direct attack of a

thiolate, with both pathways having comparable energies. Therefore, the chemical model used in this study did not decidedly favour one mechanism over the other. However, investigation of these reactions within the active site of the enzyme may help provide critical insights into the catalytic mechanism of MsrB.

In the present chapter, we have employed density functional theory methods to investigate the mechanism for the reduction of MetSO by MsrB.

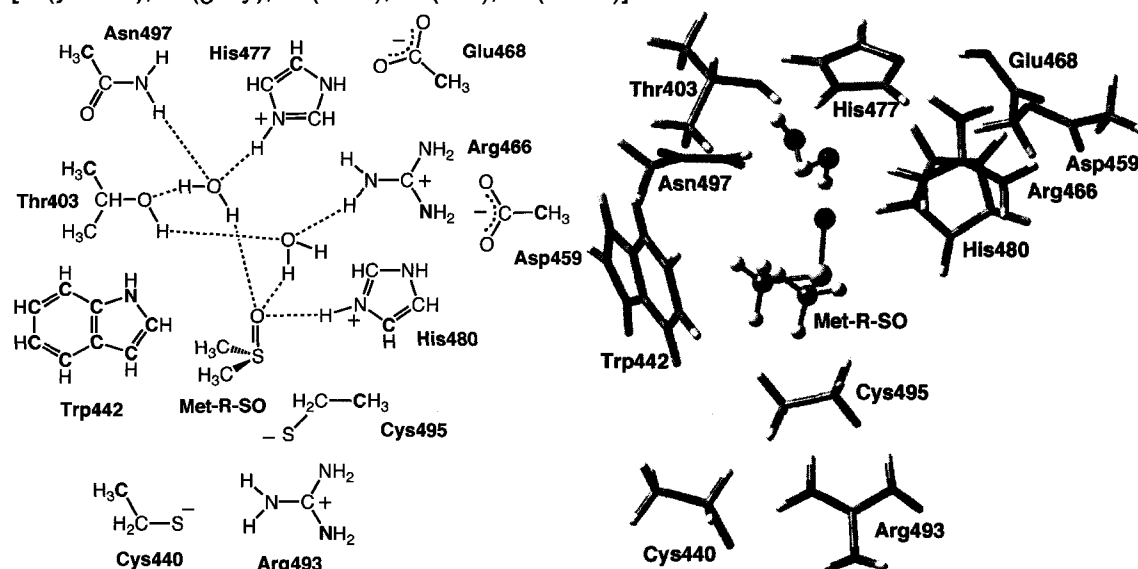
6.2 Computational Methods

All optimizations were performed using the Gaussian 03²⁹ program with the density function theory method B3LYP; a combination of Becke's three parameter exchange functional,³⁰ as implemented in the above program,³¹ and Lee, Yang and Parr's correlation functional.³² The basis set chosen for the optimizations were dependent on the model used (see below); M_{Sm} , M_{Med} , and M_{Lrg} models employed the 6-311G(d,p), 6-31G(d), and 3-21G* basis sets, respectively. Frequency calculations were used to characterize the structures as minima or transition structures in the M_{Sm} and M_{Med} models, whereas linear transit scans were used to approximate the transition states in the M_{Lrg} model. Effects due to the environment around the active site were modelled using the Integral Equation Formalism Polarizable Continuum model (IEF-PCM) as implemented in Gaussian 03, with a dielectric constant of 4.0, as previously suggested for proteins.^{33,34} Single point energy calculations were performed at the B3LYP/6-311+G(2df,p)//B3LYP/6-311G(d,p), B3LYP/6-311+G(2df,p)//B3LYP/6-31G(d) and B3LYP/6-311G(d,p)//B3LYP/3-21G* level of theories for M_{Sm} , M_{Med} and M_{Lrg} models, respectively, to obtain more reliable energies.

In this study we have considered three chemical models for the MsrB system: an isolated model (M_{Sm}), a moderate size active site model (M_{Med}), and a large active site

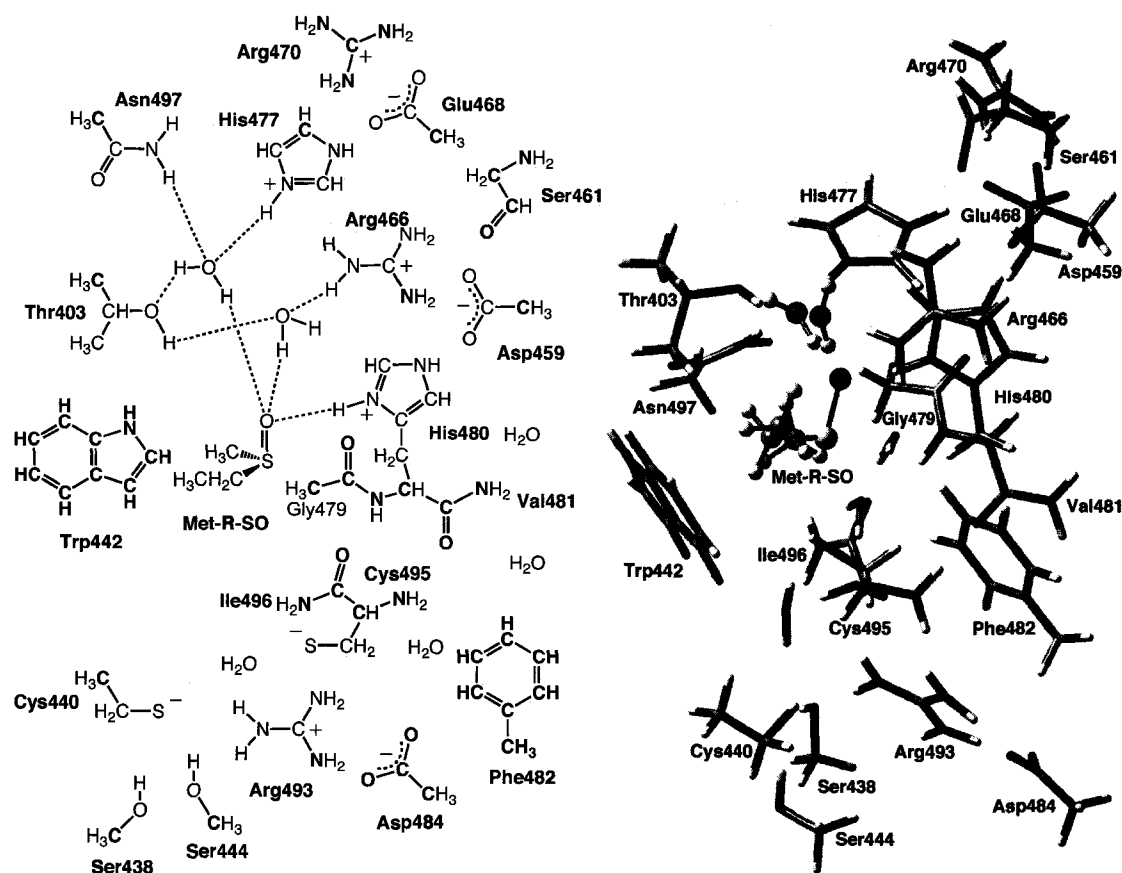
model (M_{Lrg}). The substrate, methionine-R-sulfoxide, has been modelled as dimethyl sulfoxide (DMSO) in M_{Sm} and M_{Med} and ethyl methyl sulfoxide in M_{Lrg} . The active site for the latter two models was obtained from the MsrB crystal structure of *Neisseria gonorrhoeae* pilB (PDB: 1L1D).¹⁹ The M_{Med} model (Scheme 6.4) includes the proposed catalytic (Cys495) and 'recycling' (Cys440) cysteines, a nearby arginine (Arg493) and a tryptophan (Trp442) that is proposed to help orient the substrate. In addition, the amino acid residues that may directly interact with the oxygen of the substrate (His480) or those that interact through water molecules (His477, Asn497, Thr403, and Arg466) have also been included. The amino acids have been modelled as follows: ethylthiolates for cysteines, guanidinium cations for arginine, indole for tryptophan, protonated imidazoles for histidines and acetate for both aspartate and glutamate.

Scheme 6.4. Schematic illustration and optimized substrate structure (1_{Med}) of the active site of MsrB for the M_{Med} model calculations. Fixed points are coloured red and bolded. [S (yellow); C (gray); N (blue); O (red); H (white)].



The M_{Lrg} model includes all of the M_{Med} amino acids as well as additional second shell residues and selected portions of the peptide backbone that may influence the active site amino acids (Scheme 6.5). In both active site models, selected segments of the active site were held fixed in their crystal structure position, including the terminal atoms of the residues, to maintain the integrity of the active site. The atoms that were fixed are highlighted and bolded in red in Schemes 6.4 and 6.5.

Scheme 6.5. Schematic illustration and optimized substrate structure (1_{Lrg}) of the active site of MsrB for the M_{Lrg} model calculations. Fixed points are coloured in red and bolded. [S (yellow); C (gray); N (blue); O (red); H (white)].



6.3 Results

6.3.1. Non-Covalent Binding of the Substrate within the Active Site

Our investigation of the reduction mechanism of MsrB commences with a look into the binding of the substrate within the active site. The crystal structure of MsrB used in this study contains a cacodylate molecule bound within its active site. Its orientation has been suggested to mimic the interactions of Met-(R)-SO with the active site residues.²² Thus, the position of the cacodylate molecule was taken as a starting point for our substrate, which we have modelled as a DMSO in M_{Med} and ethyl methyl sulfoxide in M_{Lrg} . In addition, we have investigated alternative orientations of the substrate, in which a transfer of the oxygen moiety of the sulfoxide to the Cys495 to form a sulfenic acid may be favourable (not shown). These results reveal, however, that the lowest energy structures of the substrate bound to the active site correspond to the cacodylate orientation as previously proposed.²² This orientation is shown in $\mathbf{1}_{\text{Med}}$ and $\mathbf{1}_{\text{Lrg}}$ of Figure 6.1.

In $\mathbf{1}_{\text{Med}}$, the oxygen of the sulfoxide (O_{M}) interacts via a strong hydrogen bond to the nearby His480 at 1.652 Å, as well as by slightly weaker hydrogen bonds to two water molecules, $\text{H}_2\text{O}_{\text{Arg}}$ and $\text{H}_2\text{O}_{\text{His}}$, at 1.771 and 1.867 Å, respectively. These water molecules are found to hydrogen bond with Arg466 and His477, at distances of 2.029 and 1.861 Å, respectively. In the larger active site ($\mathbf{1}_{\text{Lrg}}$), these interactions are found to be slightly shorter compared to those of $\mathbf{1}_{\text{Med}}$, with O_{M} forming stronger hydrogen bonds to His480, $\text{H}_2\text{O}_{\text{Arg}}$ and $\text{H}_2\text{O}_{\text{His}}$ at 1.593, 1.559 and 1.517 Å, respectively (Figure 6.1). Importantly, the substrate binds such that its sulfur centre (S_{M}) is directly over the catalytic cysteine (Cys495). These $S_{\text{M}} \cdots S_{\text{Cys495}}$ distances in $\mathbf{1}_{\text{Med}}$ and $\mathbf{1}_{\text{Lrg}}$ are found to be 3.249 and 2.849 Å, respectively. Thus, this orientation of the substrate within the active site suggests that the nucleophilic attack via Cys495 may be a feasible first step as proposed in the mechanisms (Schemes 6.2 and 6.3).

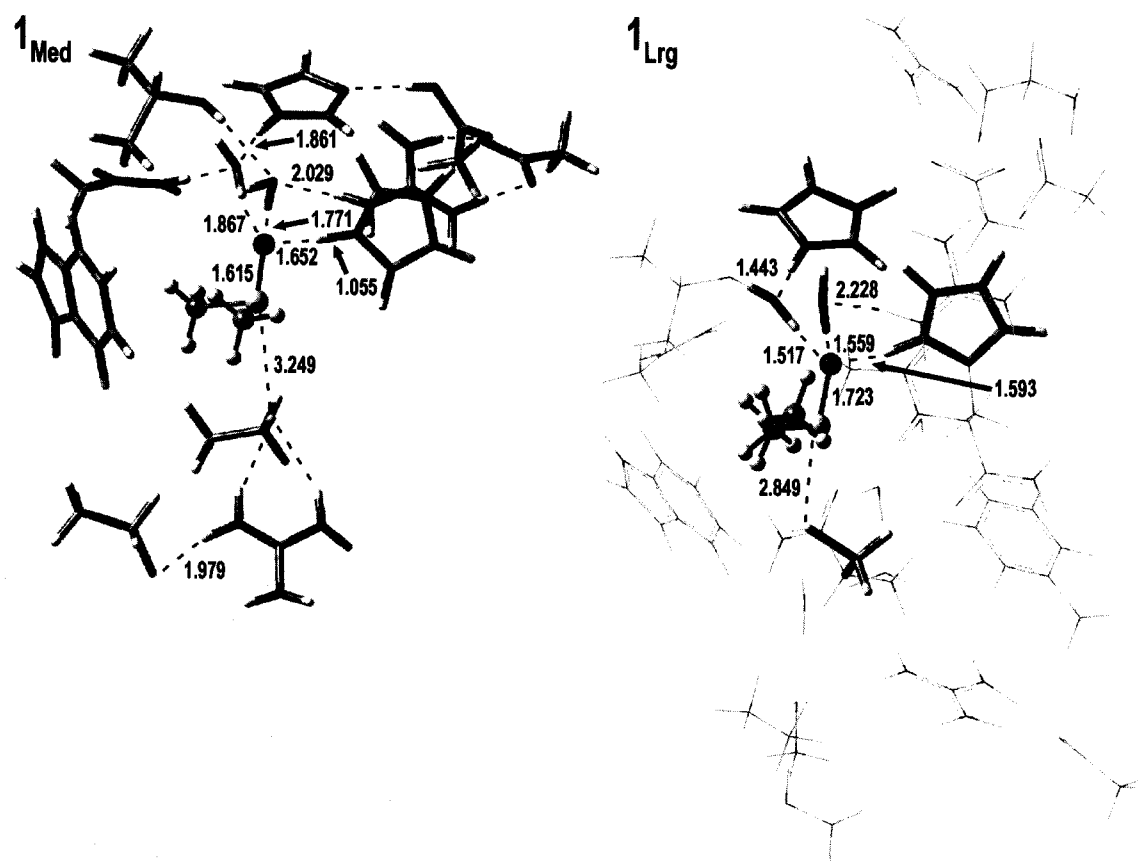


Figure 6.1. Optimized geometry of the lowest energy structures of the non-covalently bound substrates within the active site models M_{Med} and M_{Lrg} . [S (yellow); C (gray); N (blue); O (red); H (white)].

6.3.2 Covalent Binding of the Substrate within the Active Site

Based on the proposed models of the substrate bound active site, we were able to initiate our investigation into the reduction mechanisms of MsrB. The potential energy surfaces obtained from the M_{Med} (blue solid) and M_{Lrg} (red dashed) reactions are shown in Figure 6.2.

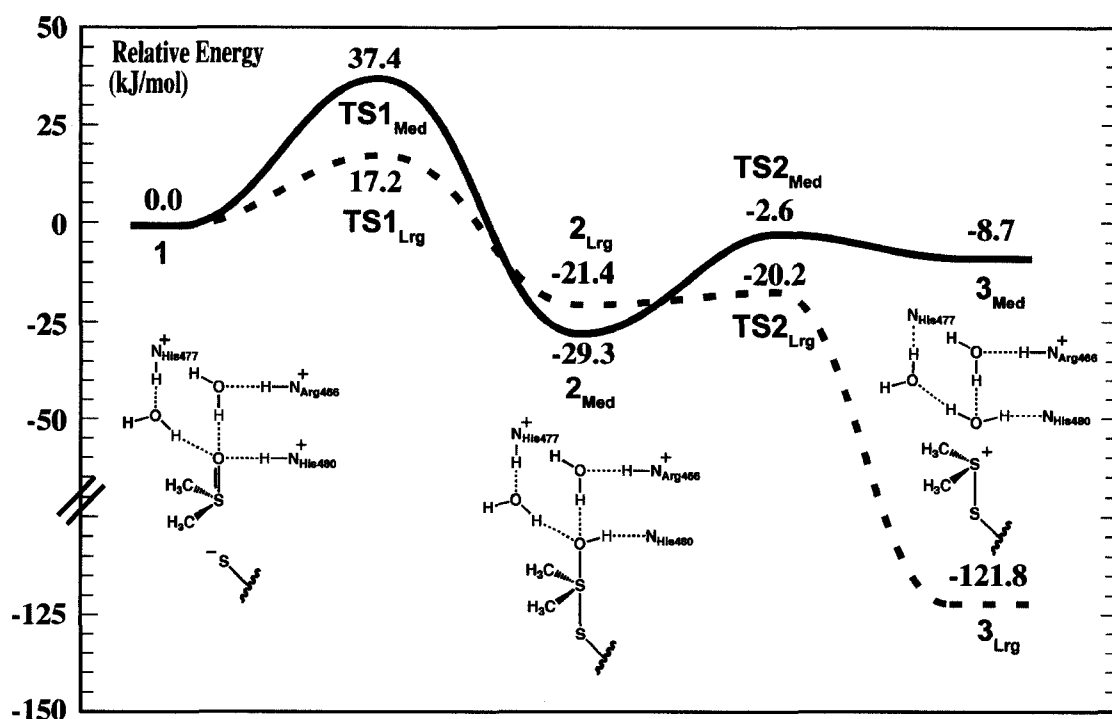


Figure 6.2. Potential energy surface and schematic illustration of key intermediates in the reduction of methionine-R-sulfoxide by MsrB to a sulfonium cation intermediate. Only residues directly involved in the catalysis are shown in the intermediates for clarity. The blue and red PES's correspond to M_{Med} and M_{Lrg} , respectively.

In the first step of the proposed mechanisms, the sulfur of Met-(R)-SO is believed to be attacked by the catalytic cysteine to form a sulfurane intermediate (Schemes 6.2 and 6.3). This sulfurane intermediate, however, is depicted in both the protonated (S—OH) and unprotonated (S—O⁻) forms in various mechanisms.^{17,19} Interestingly, it is found that the unprotonated sulfurane anion is unstable, for upon optimization, it spontaneously dissociates to a thiolate···DMSO complex. However, upon protonation of the sulfoxide's oxygen, the sulfurane intermediate is rendered stable. The molecular orbitals of DMSO and protonated DMSO—H⁺ (Figure 6.3) reveal that upon protonation of the sulfoxide oxygen, the lowest unoccupied molecular orbital (LUMO) reorients, such that it is then located in the axial position. This is then ideally

positioned for nucleophilic attack by the underlying cysteine (Cys495). The proton affinity of DMSO is found to be $1034.2 \text{ kJ mol}^{-1}$, which is higher than that of H_2O , but lower than that of NH_3 . Thus, in the presence of an acidic group, DMSO is quite capable of accepting a proton. Together these results indicate that the protonation of the sulfoxide oxygen may facilitate the formation of a sulfurane intermediate within the reaction mechanism.

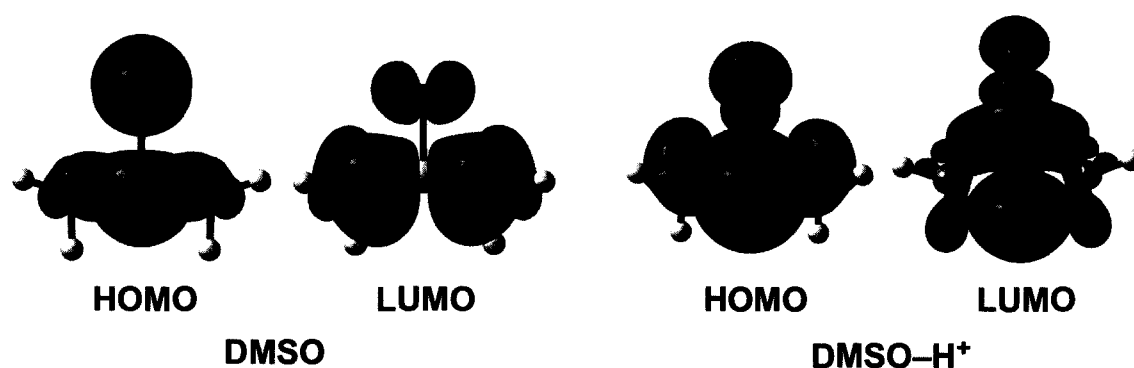


Figure 6.3. The highest occupied (HOMO) and lowest unoccupied (LUMO) molecular orbitals of DMSO and DMSO-H^+ .

Investigation of the active site reveals three possible sources of a proton for the sulfoxide oxygen: His480, His477 via $\text{H}_2\text{O}_{\text{His}}$ and Arg466 via $\text{H}_2\text{O}_{\text{Arg}}$. In this step, we find that the proton of His480 is transferred to the oxygen moiety of the sulfoxide, while concomitantly, Cys495 nucleophilically attacks the S centre of the substrate. This step is found to proceed through TS1_{Med} with a barrier of 37.4 kJ mol^{-1} (17.2 kJ mol^{-1} for TS1_{Lrg}). Importantly, this results in an enzyme-bound substrate, in the form of a sulfurane (2_{Med}), which lies $-29.3 \text{ kJ mol}^{-1}$ relative to 1_{Med} (21.4 kJ mol^{-1} for 2_{Lrg}). In 2_{Med} (Figure 6.4), the newly formed enzyme-Met-(R)-SO disulfide bond is 2.289 \AA in length, which is 0.181 \AA longer than that found in the isolated sulfurane (2.430 \AA). In addition, upon protonation, the $\text{O}_M\text{-S}_M$ bond of the sulfurane has elongated

significantly by 0.504 Å to 2.119 Å. Within the active site, the proton of the S—OH group is now hydrogen bonded to the nitrogen of His480 at a distance of 1.816 Å. Interestingly, the sulfurane's oxygen has now strengthened both of its interactions with the water molecules (1.613 Å and 1.666 Å to H₂O_{Arg} and H₂O_{His}, respectively). These water molecules, in turn, have strengthened their hydrogen bonds with Arg466 and His477 (1.993 and 1.758 Å, respectively). However, we note that in **2**_{Med}, an active site arginine (Arg493) immediately gives up a proton to the thiolate Cys440. This is a result of the loss of the interaction between Cys495 and Arg493 found in **1**_{Med} when the sulfurane intermediate is formed. However, this appears to be an artefact of the model, as within **2**_{Lrg} this protonation of the cysteine is not found to occur, possibly due to the additional interactions provided by the enlarged model.

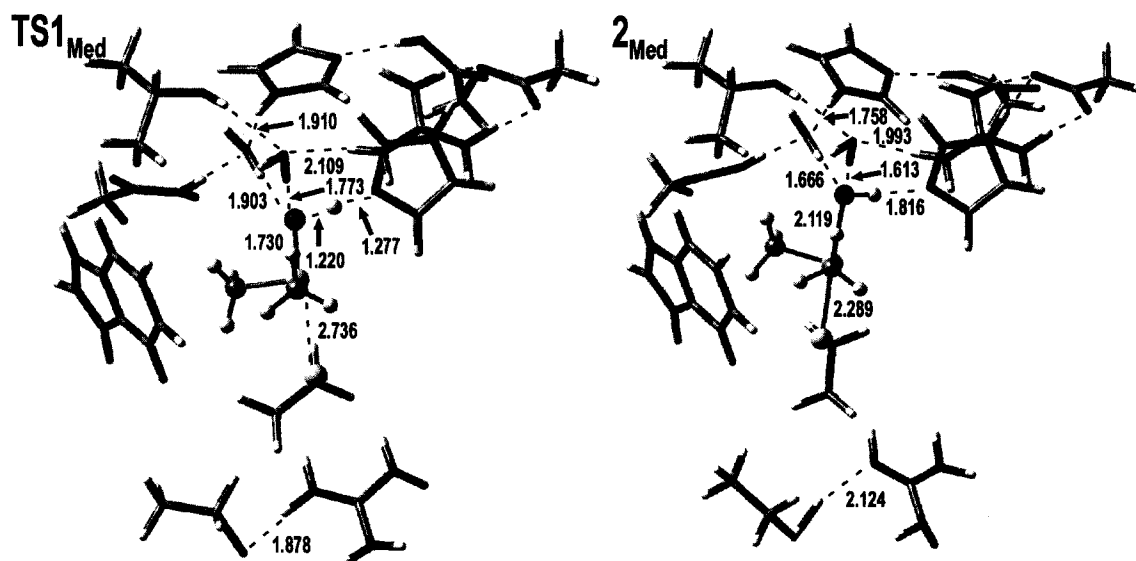


Figure 6.4. Optimized geometries of the transition structure (**TS1**_{Med}) and intermediate (**2**_{Med}) resulting from the concomitant proton transfer and nucleophilic attack of the thiolate on DMSO to form an enzyme bound sulfurane. [S (yellow); C (gray); N (blue); O (red); H (white)].

In 2_{Lrg} , both the $S_{\text{Cys495}}-S_{\text{M}}$ and $S_{\text{M}}-O_{\text{M}}$ bonds of the sulfurane are found to be slightly longer than those in 2_{Med} at 2.254 and 2.318 Å, respectively. In addition, the $\text{H}_2\text{O}_{\text{Arg}} \cdots \text{Arg466}$ hydrogen bond has increased by 0.249 Å to 2.477 Å in 2_{Lrg} , relative to 1_{Lrg} , while that of the $\text{H}_2\text{O}_{\text{His}} \cdots O_{\text{M}}$ has marginally shortened to 1.467 Å. However, the interactions of O_{M} with $\text{H}_2\text{O}_{\text{Arg}}$ and $\text{H}_2\text{O}_{\text{His}}$ have shortened even further in 2_{Lrg} , to 1.399 and 1.467 Å, respectively.

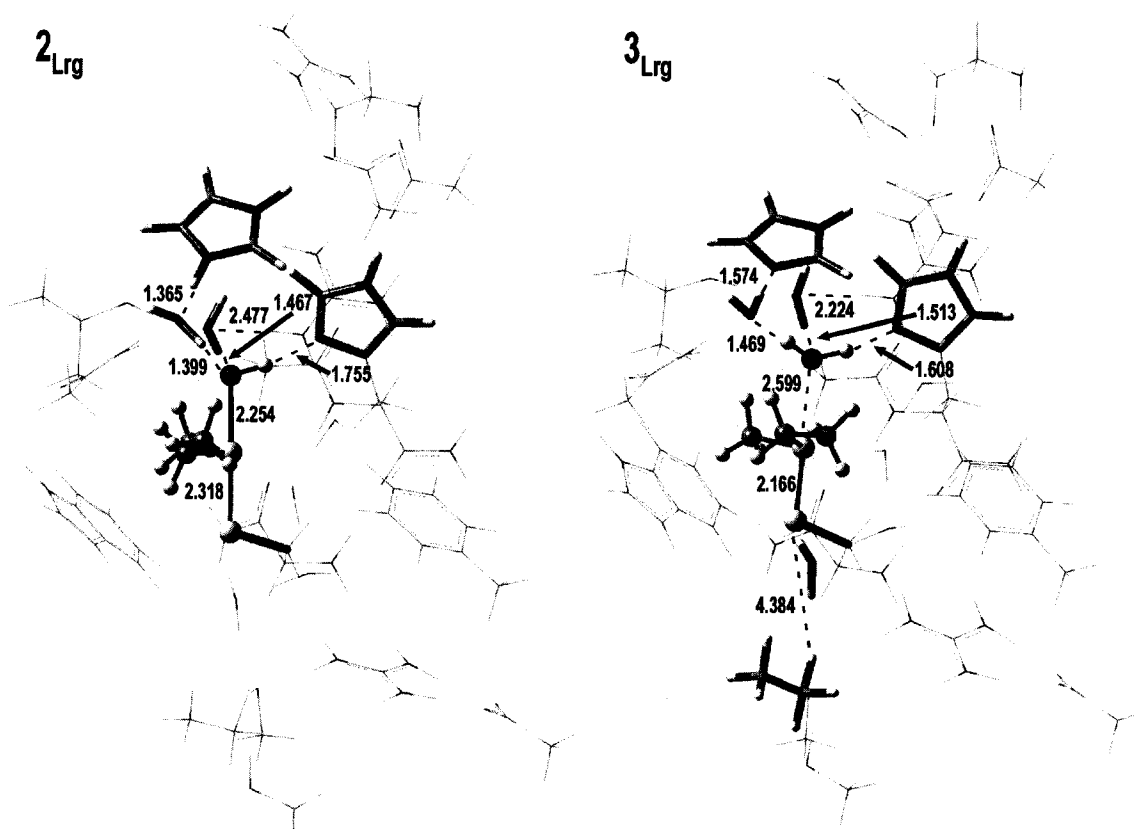


Figure 6.5. Optimized geometries of the intermediates 2_{Lrg} and 3_{Lrg} . [S (yellow); C (gray); N (blue); O (red); H (white)].

6.3.3 Regeneration of the 'Active Site Bound' Methionine

Based on the proposed mechanisms, there are two possible steps that may follow the formation of a sulfurane intermediate to regenerate the methionine residue: (1) the

transfer of the OH^- group from the methionine sulfur to that of the cysteine, or (2) the addition of a second proton. We initially considered the intramolecular transfer of an OH^- group in an isolated model with the resulting potential energy surface shown in Figure 6.6.

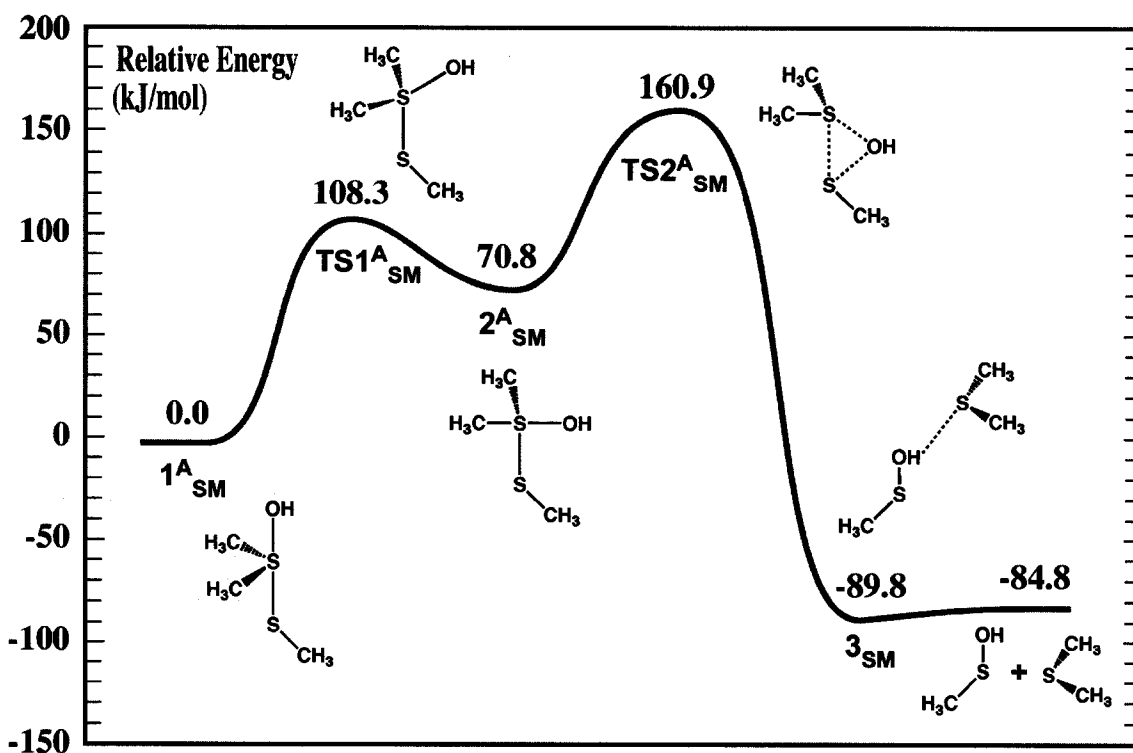


Figure 6.6. Potential energy surface of the intramolecular rearrangement and OH^- transfer of a sulfurane to generate a sulfenic acid and dimethyl sulfide.

The most stable conformation of the sulfurane intermediate was found to correspond to 1^A_{SM} . Due to the preferred orientation of sulfuranes, in which the most electronegative ligands occupy the axial positions, the $\text{O}-\text{S}_{\text{cys}}$ distance and the $\text{O}_M-\text{S}_M-\text{S}_{\text{cys}}$ angle in 1^A_{SM} is 4.297 Å and 178.4°, respectively. Thus, the direct transfer of the hydroxyl to the cysteine in this conformation seems unlikely. However, the sulfurane may undergo a conformational change that orients the OH^- and S_{cys} perpendicular (90°) to one another, which may facilitate the transfer. Such a

rearrangement occurs via $\text{TS1}^{\text{A}}_{\text{Sm}}$, with a barrier of $108.3 \text{ kJ mol}^{-1}$, with the resulting structure, 2^{A}_{Sm} , lying 70.8 kJ mol^{-1} higher in energy than 1^{A}_{Sm} . From 2^{A}_{Sm} , the OH^- may directly transfer to the S centre of the thiolate through an epoxide-like transition structure ($\text{TS2}^{\text{A}}_{\text{Sm}}$). The barrier for this step is 90.1 kJ mol^{-1} , relative to 2^{A}_{Sm} ($160.9 \text{ kJ mol}^{-1}$ overall) and results in the cleavage of the disulfide bond to generate Met and sulfenic acid. The resulting product complex (3^{A}_{Sm}) lies $160.7 \text{ kJ mol}^{-1}$ lower in energy than 2^{A}_{Sm} ($-89.8 \text{ kJ mol}^{-1}$ overall). This reaction for the transfer of the OH^- group is high in energy; however, the active site may serve to stabilize the intermediates and facilitate the reaction.

Within the active site, the sulfurane was optimised in the conformation corresponding to 2^{A}_{Sm} . As shown in Figure 6.7, two conformations were optimised, which vary in the orientation of the hydroxyl group. In $2^{\text{B}}_{\text{Med}}$, the OH^- was transferred down the back of the active site, at a $\text{S}_{\text{Cys495}}-\text{S}_{\text{M}}-\text{O}_{\text{M}}$ angle of approximately 90° . This structure, however, is $113.5 \text{ kJ mol}^{-1}$ higher in energy than 2_{Med} (84.2 kJ mol^{-1} overall). The second conformation ($2^{\text{C}}_{\text{Med}}$) corresponds to the OH^- moiety being transferred down the front of the active site near Arg493. However, this results in a significant movement of the sulfurane, as the OH^- moiety hydrogen bonds with the protons of the Arg below (Arg493). $2^{\text{C}}_{\text{Med}}$ is found to be $126.6 \text{ kJ mol}^{-1}$ higher in energy than 2_{Med} . Thus, this suggests that the intramolecular transfer of the hydroxyl moiety is not favoured within the active site of MsrB.

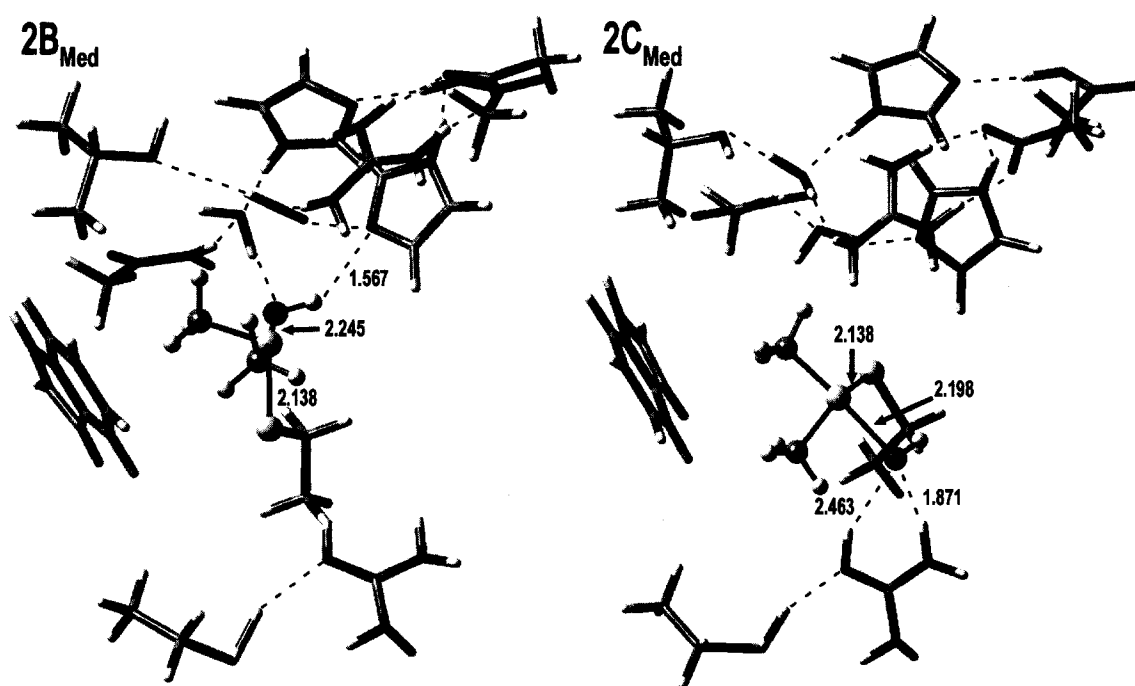


Figure 6.7. Optimized structures for transfer of the OH⁻ group closer proximity to the sulfur of Cys495. [S (yellow); C (gray); N (blue); O (red); H (white)].

Alternatively, a second proton may be added to the OH⁻ group, as proposed in the mechanism of Lowther *et al.*²² In fact, the proton affinity of the sulfurane intermediate **1^A_{SM}** is found to be 1222.1 kJ mol⁻¹, higher than those of ammonia and DMSO. Thus, the formation of the protonated sulfurane intermediate enhances the basicity of the oxygen moiety of the substrate, encouraging the addition of a second proton.

Within the active site of the enzyme, there remains two residues, His477 and Arg466, which are capable of donating an additional proton to the sulfurane's hydroxyl group through a water molecule. We find that in **M_{Med}**, Arg466 can provide the second proton via a barrier of 26.7 kJ mol⁻¹ in **TS2_{Med}** to form the intermediate **3_{Med}** shown in Figure 6.7. **3_{Med}** lies 20.6 kJ mol⁻¹ higher than **2_{Med}**, but 8.7 kJ mol⁻¹ lower than **1_{Med}** (see Figure 6.2). Attempts to transfer the proton of His477 to this moiety in **M_{Med}**

6.3.4 Ongoing and Future Work

Following the formation of the sulfonium cation, the covalent disulfide bond linking the methionine to the enzyme must be cleaved to release methionine. This may occur as proposed in the MsrA mechanism by Lowther *et al.* (Scheme 6.3) via the direct attack of the 'recycling' cysteine (Cys440). Alternatively, a water molecule bridging the two cysteines in the active site, may donate one of its protons to Cys440 and then nucleophilically attack the sulfonium cation. Interestingly, this latter process would result in the formation of a sulfenic acid. Both of these mechanisms were considered by Balta *et al.*³⁵ in their small model study, in which they found that the water attack has a barrier of only 3.8 kJ mol⁻¹, while that of the thiolate attack was found to be only slightly higher in energy at 10.0 kJ mol⁻¹. Therefore, both of these pathways are of interest and warrant further investigation within the active site. These two reaction pathways are currently being explored within the MsrB active site.

6.4 Preliminary Conclusions

Although this investigation into the reduction mechanism catalyzed by MsrB is incomplete, several conclusions may still be formulated:

1. The noncovalent binding of the substrate to the active site positions the substrate such that it is directly above the proposed catalytic cysteine (Cys495).
2. Protonation is required for the formation of an enzyme-substrate sulfurane, as the sulfurane anion itself is found not to be stable. The proposed step corresponding to the formation of such an intermediate is found to occur via the concomitant protonation of the sulfoxide oxygen by His480 and a nucleophilic attack by Cys495 on the substrate.
3. In order to regenerate the active site-bound methionine a second protonation event is found occur at the sulfurane's hydroxyl group. In addition, we have shown that the intramolecular rearrangement of the sulfurane to position the OH⁻

group closer in proximity of the S centre of Cys495 to enable its transfer is unlikely, as these intermediates are high in energy.

References

- (1) Stadtman, E. R. *Curr. Med. Chem.* **2004**, *11*, 1105.
- (2) Schöneich, C. *Exp. Gerontol.* **1999**, *34*, 19.
- (3) Levine, R. L.; Moskovitz, J.; Stadtman, E. R. *IUBMB Life* **2000**, *50*, 301.
- (4) Levine, R. L.; Mosoni, L.; Berlett, B. S.; Stadtman, E. R. *Proc. Natl. Acad. Sci. USA* **1996**, *93*, 15036.
- (5) Levine, R. L.; Berlett, B. S.; Moskovitz, J.; Mosoni, L.; Stadtman, E. R. *Mech. Age. Dev.* **1999**, *107*, 323.
- (6) Petropoulos, I.; Friguet, B. *Biochim. Biophys. Acta* **2005**, *1703*, 261.
- (7) Vogt, W. *Free Radic. Biol. Med* **1995**, *18*, 93.
- (8) Weissbach, H.; Resnick, L.; Brot, N. *Biochim. Biophys. Acta* **2005**, *1703*, 203.
- (9) Moskovitz, J. *Biochim. Biophys. Acta* **2005**, *1703*, 213.
- (10) Schöneich, C. *Biochim. Biophys. Acta* **2005**, *1703*, 111.
- (11) Haenold, R.; Wassef, D. M.; Heinemann, S. H.; Hoshi, T. *Age* **2005**, *27*, 183.
- (12) Weissbach, H.; Etienne, F.; Hoshi, T.; Heinemann, S. H.; Lowther, W. T.; Matthews, B. W.; St. John, G.; Nathan, C.; Brot, N. *Arch. Biochem. Biophys.* **2002**, *397*, 172.
- (13) Sharov, V. S.; Ferrington, D. A.; Squier, T. C.; Schöneich, C. *FEBS Lett.* **1999**, *455*, 247.
- (14) Grimaud, R.; Ezraty, B.; Mitchell, J. K.; Lafitte, D.; Briand, C.; Derrick, P. J.; Barras, F. *J. Biol. Chem.* **2001**, *276*, 48915.
- (15) Ezraty, B.; Aussel, L.; Barras, F. *Biochim. Biophys. Acta* **2005**, *1703*, 221.

- (16) Weissbach, H.; Etienne, F.; Hoshi, T.; Heinemann, S. H.; Lowther, W. T.; Matthews, B. W.; St. John, G.; Nathan, C.; Brot, N. *Arch. Biochem. Biophys.* **2002**, *397*, 172.
- (17) Olry, A.; Boschi-Muller, S.; Marraud, M.; Sanglier-Cianferani, S.; Van Dorsselear, A.; Branlant, G. *J. Biol. Chem.* **2002**, *277*, 12016.
- (18) Kauffmann, B.; Aubry, A.; Favier, F. *Biochim. Biophys. Acta* **2005**, *1703*, 249.
- (19) Lowther, W. T.; Weissbach, H.; Etienne, F.; Brot, N.; Matthews, B. W. *Nature Struc. Biol.* **2002**, *9*, 348.
- (20) Moskovitz, J.; Poston, J. M.; Berlett, B. S.; Nosworthy, N. J.; Szczepanowski, R.; Stadtman, E. R. *J. Biol. Chem.* **2000**, *275*, 14167.
- (21) Boschi-Muller, S.; Azza, S.; Sanglier-Cianferani, S.; Talfournier, F.; Van Dorsselear, A.; Branlant, G. *J. Biol. Chem.* **2000**, *275*, 35908.
- (22) Lowther, W. T.; Brot, N.; Weissbach, H.; Honek, J. F.; Matthews, B. W. *Proc. Natl. Acad. Sci. USA* **2000**, *97*, 6463.
- (23) Kim, H.-Y.; Gladyshev, V. N. *Mol. Biol. Cell* **2004**, *15*, 1055.
- (24) Lowther, W. T.; Brot, N.; Weissbach, H.; Matthews, B. W. *Biochemistry* **2000**, *39*, 13307.
- (25) Taylor, A. B.; Benglis, D. M.; Dhandayuthapani, S.; Hart, P. J. *J. Bacteriol.* **2003**, *185*, 4119.
- (26) Boschi-Muller, S.; Olry, A.; Antoine, M.; Branlant, G. *Biochim. Biophys. Acta* **2005**, *1703*, 231.
- (27) Kumar, R. A.; Koe, A.; Cerney, R. L.; Gladyshev, V. N. *J. Biol. Chem.* **2002**, *277*, 37527.
- (28) Balta, B.; Monard, G.; Ruiz-Lopez, M. F. *J. Phys. Chem. A* **2006**, *110*, 7628.
- (29) Frisch, M. J.; Trucks, G. W.; Schlegel, H. B.; Scuseria, G. E.; Robb, M. A.; Cheeseman, J. R.; Montgomery, J. A. J.; Vreven, T.; Kudin, K. N.; Burant, J. C.; Millam, J. M.; Iyengar, S. S.; Tomasi, J.; Barone, V.; Mennucci, B.; Cossi, M.;

Scalmani, G.; Rega, N.; Petersson, G. A.; Nakatsuji, H.; Hada, M.; Ehara, M.; Toyota, K.; Fukuda, R.; Hasegawa, J.; Ishida, M.; Nakajima, T.; Honda, Y.; Kitao, O.; Nakai, H.; Klene, M.; Li, X.; Knox, J. E.; Hratchian, H. P.; Cross, J. B.; Adamo, C.; Jaramillo, J.; Gomperts, R.; Stratmann, R. E.; Yazyev, O.; Austin, A. J.; Cammi, R.; Pomelli, C.; Ochterski, J.; Ayala, P. Y.; Morokuma, K.; Voth, G. A.; Salvador, P.; Dannenberg, J. J.; Zakrzewski, V. G.; Dapprich, S.; Daniels, A. D.; Strain, M. C.; Farkas, O.; Malick, D. K.; Rabuck, A. D.; Raghavachari, K.; Foresman, J. B.; Ortiz, J. V.; Cui, Q.; Baboul, A. G.; Clifford, S.; Cioslowski, J.; Stefanov, B. B.; Liu, G.; Liashenko, A.; Piskorz, P.; Komaromi, I.; Martin, R. L.; Fox, D. J.; Keith, T. A.; Al-Laham, M. A.; Peng, C. Y.; Nanayakkara, A.; Challacombe, M.; Gill, P. M. W.; Johnson, B. G.; Chen, W.; Wong, M. W.; Gonzalez, C.; Pople, J. A. Gaussian 03; Gaussian Inc.: Wallingford CT, 2004.

(30) Becke, A. D. *J. Chem. Phys.* **1993**, *98*, 1372.

(31) Stephens, P. J.; Devlin, F. J.; Chabalowski, C. F.; Frisch, M. J. *J. Phys. Chem.* **1994**, *98*, 11623.

(32) Lee, C.; Yang, W.; Parr, R. G. *Phys. Rev. B* **1988**, *37*, 785.

(33) Siegbahn, P. E. M.; Blomberg, M. R. A. *Chem. Rev.* **2000**, *100*, 421.

(34) Noodleman, L.; Lovell, T.; Han, W.-G.; Li, J.; Himo, F. *Chem. Rev.* **2004**, *104*, 459.

(35) Brot, N.; Collet, J.-F.; Johnson, L. C.; Jönsson, T. J.; Weissbach, H.; Lowther, W. T. *J. Biol. Chem.* **2006**, *281*, 32668.

Chapter 7

Conclusions

In this thesis, computational techniques have been used to investigate the properties of metallenzymes and metallo-like biomolecules. In particular, the catalytic mechanisms of the metalloenzymes LpxC and NOS, as well as the non-metal, redox active, enzyme MsrB were systematically investigated. In addition, the metallo-like complexation of NO^+ and the interactions of NO^- with the aromatic amino acids were also studied.

From the investigation of the mechanism of LpxC in Chapter 3, our results indicate that the binding of the substrate to the LpxC active site preferentially occurs via coordination of the substrate's carbonyl oxygen to the Zn^{2+} ion between the Zn-bound water and the threonine residue. It was also found that the deacetylation reaction occurs via an acid/base pair mechanism as previously proposed.¹ Specifically, an active site glutamate is found to deprotonate the Zn^{2+} -bound water upon binding of the substrate to the active site. This leads to the rate-determining step corresponding to nucleophilic attack of the OH^- on the substrate. The barrier for this step is found to be approximately half that of the water-assisted system, due in part to the increased nucleophilicity of the OH^- moiety compared to that of H_2O , as well as due to the stabilization of the transition structure and initial *gem*-diolate intermediate provided by the active site. A histidine residue is then employed to protonate the amino nitrogen of the resulting intermediate. However, unlike the isolated system, where protonation leads to cleavage of the amide bond, the protonated intermediate is stabilized within the active site of LpxC via

interactions with the Zn^{2+} ion. Thus, the collapse of this intermediate requires additional reaction steps including a change in the hydrogen-bonding network of the histidine, which is not observed in related metallopeptidases.

In Chapter 4, DFT methods were used to investigate the second half-reaction of nitric oxide synthase (NOS). Specifically, we first investigated the possible reactions of the previously suggested initial intermediate $\text{Fe}_{\text{heme}}-(\text{H})\text{OOH}$.² We found that the lowest energy pathway is analogous to the ping-pong mechanism by which heme peroxidases form a Compound I species from an initial $\text{Fe}_{\text{heme}}-(\text{H})\text{OOH}$ species. In particular, it is found that the substrate itself appears to play a role in its own oxidation, by participating in a series of proton rearrangement steps, resulting in the release of O_{out} as H_2O , with the concomitant formation of a Compound I intermediate. The formation of the final products, citrulline and NO, is then found to occur via a one-step reaction. Specifically, the lowest energy pathway is found to involve attack of the $\text{Fe}_{\text{heme}}-\text{O}$ moiety at the C_{guan} centre of the substrate via a 'tetrahedral-like' transition structure (**TS5**³) containing a heme-oxo cross-link $\text{Fe}_{\text{heme}}-\text{O}-\text{C}_{\text{guan}}$, which 'decomposes' to give citrulline and NO directly.

Complexes formed by the interaction of NO^+ and NO^- with C_6H_6 (benzene) and the aromatic *R*-groups of the amino acids phenylalanine (Phe), tyrosine (Tyr), histidine (His) and tryptophan (Trp) have been investigated in Chapter 5. In particular, both the half- ($\text{Ar}\cdots\text{NO}^{+/-}$) and full-sandwiches $\text{Ar}\cdots\text{NO}^{+/-}\cdots\text{Ar}$ (where the Ar groups are the same) were studied. In all $\text{Ar}\cdots\text{NO}^+$ complexes considered, NO^+ binds via its nitrogen centre to the π -system of the aromatic, with the exception of His. The cationic π -sandwich complexes $[\text{Ar}\cdots\text{NO}\cdots\text{Ar}]^+$ are not found to correspond to a 'doubling' of their parent half-sandwiches. For the $\text{Ar}\cdots\text{NO}^-$ complexes considered, NO^- binds side-on to the aromatic species via two hydrogen bonds. However, the anionic $[\text{Ar}\cdots\text{NO}\cdots\text{Ar}]^-$

complexes are found to correspond to a 'doubling' of the $\text{Ar}\cdots\text{NO}^-$. The calculated complexation energies (ΔE_{corr} 's) for those complexes involving NO^+ binding via the π -systems of the aromatic species indicate that NO^+ exhibits a clear preference for the aromatic group of tryptophan. Indeed, for both half- and full-sandwich type complexes this preference is in the order $\text{Trp} \gg \text{Tyr} > \text{His} > \text{Phe} > \text{C}_6\text{H}_6$. For the anionic complexes, the calculated ΔE_{corr} 's indicate that NO^- strongly prefers those aromatic groups that contain conventional hydrogen bond donor groups such as $-\text{OH}$ or $-\text{NH}-$. For both types of complexes the order of preference is $\text{His} > \text{Tyr} > \text{Trp} \gg \text{Phe} > \text{C}_6\text{H}_6$.

In Chapter 6 the reduction mechanism catalysed by MsrB is investigated. Thus far, the results indicate that the non-covalent binding of the substrate to the active site positions the substrate such that it is directly above the proposed catalytic cysteine (Cys495). However, protonation of the oxygen of MetSO is required for the formation of an enzyme-substrate sulfurane, as the sulfurane anion itself is found to be unstable. The proposed step corresponding to the formation of such an intermediate is found to occur via the concomitant protonation of the sulfoxide oxygen by His480 and a nucleophilic attack by Cys495 on the substrate. In order to regenerate the 'active site-bound methionine', a second protonation event is found to occur at the sulfurane's OH^- group. In addition, we have shown that the intramolecular rearrangement of the sulfurane to position the OH^- group closer to the S centre of Cys495, enabling its transfer, is unlikely, as these intermediates are found to be high in energy.

References

- (1) Hernick, M.; Gennadios, H. A.; Whittington, D. A.; Rusche, K. M.; Christianson, D. W.; Fierke, C. A. *J. Biol. Chem.* **2005**, *280*, 16969.
- (2) Cho, K. B.; Gauld, J. W. *J. Phys. Chem. B* **2005**, *109*, 23706.

Vita Auctoris

Name: Jesse J. Robinet
Place of Birth: Windsor, Ontario
Year of Birth: 1982

Education

- M. Sc. Candidate 2005 – Present
University of Windsor
- B. Sc. in Biochemistry 2005
University of Windsor

Publications

- Robinet, J. J.; Baciuc, C.; Cho, K.-B.; Gault, J. W. *J. Phys. Chem. A* **2007**, *111*, 1981.
- Liu, H.; Robinet, J. J.; Ananvoranich, S.; Gault, J. W. *J. Phys. Chem. A* **2007**, *111*, 439.
- Robinet, J. J.; Cho, K.-B.; Gault, J. W. *J. Am. Chem. Soc.* **2007**, submitted.
- Robinet, J. J.; Gault, J. W. *J. Phys. Chem. B* **2007**, submitted.

Presentations

- Robinet J; Gault, J.W. Computational Investigation of the Catalytic Mechanism of LpxC. Poster Presentation at 89th CSC Conference and Exhibition, Halifax, NS, 2006.
- Robinet J; Liu, H; Gault, J.W. The Role of Cytosine pK_a Perturbation in the Catalytic Mechanism of the Hepatitis Delta Virus Ribozyme. Poster Presentation at 2nd National Undergraduate Chemistry Conference, Ottawa, ON, 2004.

Awards and Scholarships

- Ontario Graduate Scholarship 2005–2007